A high-resolution study of near-IR diffuse interstellar bands, search for small-scale structure, time variability, and stellar features

Smoker, J.V.; Müller, A.; Monreal Ibero, A.; Elyajouri, M.; Evans, C.J.; Najarro, F.; ... ; Cami, J.

A&A 672, A181 (2023)
https://doi.org/10.1051/0004-6361/202142267

Astronomy & Astrophysics

A high-resolution study of near-IR diffuse interstellar bands, search for small-scale structure, time variability, and stellar features*

J. V. Smoker[1,2], A. Müller[3], A. Monreal Ibero[4,5,6], M. Elyajouri[7], C. J. Evans[2,8], F. Najarro[9], A. Farhang[10], N. L. J. Cox[11], J. Minniti[12], K. T. Smith[13], J. Pritchard[14], R. Lallement[7], A. Smette[1], H. M. J. Boffin[14], M. Cordiner[15], and J. Cami[16,17,18]

[1] European Southern Observatory, Alonso de Cordova 3107, Vitacura, Santiago, Chile
e-mail: jsmoker@eso.org
[2] UK Astronomy Technology Centre, Royal Observatory, Blackford Hill, Edinburgh EH9 3HJ, UK
[3] Max-Planck-Institut fur Astronomie, Königstuhl 17, 69117 Heidelberg, Germany
[4] Leiden Observatory, Leiden University, PO Box 9513, 2300 RA Leiden, The Netherlands
[5] Instituto de Astrofísica de Canarias, C/ Vía Láctea s/n, 38205 La Laguna, Tenerife, Spain
[6] Departamento de Astrofísica, Universidad de La Laguna, 38200 La Laguna, Tenerife, Spain
[7] GEPI, Observatoire de Paris, PSL Research University, CNRS, Place Jules Janssen, 92190 Meudon, France
[8] European Space Agency, ESA Office, Space Telescope Science Institute, 3700 San Martin Drive, Baltimore, MD 21218, USA
[9] Departamento de Astrofísica, Centro de Astrobiología, CSIC-INTA, Ctra. Torregjon a Ajalvir km. 4, 28850 Madrid, Spain
[10] School of Astronomy, Institute for Research in Fundamental Sciences, 19395-5531 Tehran, Iran
[11] ACRI-ST, Centre d'Etudes et de Recherche de Grasse (CERGA), 10 Av. Nicolas Copernic, 06130 Grasse, France
[12] Nicolaus Copernicus Astronomical Center, Polish Academy of Sciences, Bartycka 18, 00-716 Warsaw, Poland
[13] AAAS Science International, Clarendon House, Clarendon Road, Cambridge CB2 8FH, UK
[14] European Southern Observatory, Karl-Schwarzschild-Str. 2 85748 Garching bei München, Germany
[15] NASA Goddard Space Flight Center, 8800 Greenbelt Road, Greenbelt, MD 20771, USA
[16] Department of Physics and Astronomy, The University of Western Ontario, London, ON N6A 3K7, Canada
[17] Institute for Earth and Space Exploration, The University of Western Ontario, London, ON N6A 3K7, Canada
[18] SETI Institute, 189 Bernardo Ave, Suite 100, Mountain View, CA 94043, USA

Received 21 September 2021 / Accepted 26 November 2022

ABSTRACT

Context. The diffuse interstellar bands (DIBs) are a set of hundreds of unidentified absorption features that appear almost ubiquitously throughout the interstellar medium. Most DIBs appear at optical wavelengths, but some are in the near-infrared.
Aims. We aim to characterise near-infrared DIBs at high spectral resolving power towards multiple targets.
Methods. We observed 76 early-type stars at a resolving power of 50 000 (velocity resolution ~6 km s^{-1}) and signal-to-noise ratios of several hundreds using the CRyogenic high-resolution InfraRed Echelle Spectrograph (CRIRES). These data allow us to investigate the DIBs around 1318.1, 1527.4, 1561.1, 1565.1, 1567.0, 1574.4, and 1624.2 nm. We detected a total of six DIB features and 17 likely stellar features through comparisons with a model spectrum computed with CMFGEN. Additionally, we measured equivalent widths of the DIBs at 1318.1 and 1527.4 nm using observations with X-shooter towards ten very highly reddened ($3.2 < E(B-V) < 6.5$) Cepheid variable stars and towards four stars observed at low values of precipitable water vapour as well as by using other archive data.
Results. We measured correlations (correlation coefficient $r \sim 0.73$–0.96, depending on the subsample used) between DIB equivalent width and reddening for the DIBs at 1318.1, 1561.1, 1565.1, and 1567.0 nm. Comparing the near-infrared DIBs with 50 of the strongest optical DIBs, we find correlations $r > \sim 0.8$ between the 1318, 1527, 1561, 1565, and 1567 nm and the optical DIBs 5705, 5780, 6203, 6283, and 6269 Å. The 5797 Å DIB is less well correlated with the near-infrared DIBs. The DIB at 9632.1 Å, which is likely C_{60}^+, is not well correlated with the 1318.1 nm DIB. Partial correlation coefficients using E(B-V) as the covariate were also determined. For stars earlier than B2, the 1318.1 nm DIB is affected by an emission line on its blue wing that is likely stellar in nature, although we cannot rule out an interstellar or circumstellar origin for this line caused by, for example, a DIB in emission. The 1318.1 nm DIB also has an extended red wing. The line is reasonably well fitted by two Gaussian components, although neither the component equivalent width (EW) ratios nor the separation between components are obviously correlated with such indicators as $\lambda\lambda$5780/5797 and reddening. The EW at 1318 nm correlates with H I with EW(1318 nm)/$E(B-V)$ decreasing with $f(H_2)$. Five pairs of stars within one arcmin of each other show very similar 1318.1 nm DIB profiles. Possible variation in the 1318.1 nm feature is seen between HD 145501 and HD 145502 (separated by 41 arcsec, equivalent to 7200 au) and HD 168607 and HD 168625 (separated by 67 arcsec, equivalent to 0.52 pc on the plane of the sky). Seventeen sightlines have repeat CRIRES observations separated by six to 14 months, and two sightlines have repeat X-shooter observations separated by 9.9 yr. No time variability was detected in the 1318.1 nm DIB in the CRIRES data nor in the 5780.5 Å, 5797.1 Å, 1318.1 nm, and 1527.4 nm DIBs. Tentative time variation is observed in the C_{60}^+ DIBs at 9577 and 9632 Å towards HD 183143, although it is very close to the noise level and requires confirmation.
Conclusions. The Near Infrared (NIR) DIBs observed occur more in more UV-irradiated regions than the 5797 Å DIB allowing the study of heavily reddened sightlines. Future searches for time variability in DIBs will require either higher quality data, larger intervals between epochs, or both.

Key words. ISM: clouds – ISM: lines and bands – ISM: molecules – dust, extinction – stars: early-type – stars: emission-line, Be

* Equivalent width measurements of the measured lines (Table E.1) are only available at the CDS via anonymous ftp to cdsarc.cds.unistra.fr (130.79.128.5) or via https://cdsarc.cds.unistra.fr/viz-bin/cat/J/A+A/672/A181

1. Introduction

The diffuse interstellar bands (DIBs) were discovered around a century ago as unidentified absorption lines in the spectra of reddened stars (e.g. Heger 1922). The lines are generally several angstroms wide and thus cannot be atomic, and they were initially hypothesised to have arisen from dust grains or large molecules (see Cox 2011 for a review). There is a correlation between reddening and DIB strength (although with large scatter at high reddening and with $E(B-V)$ ~0.2–0.3; Wu et al. 1981, Herbig 1993, Vos et al. 2011), which initially favoured the dust hypothesis. However, a dust carrier was expected to produce emission in the wings of the DIB profiles (van de Hulst 1946), which has not been detected; wavelength shifts; and profile variations due to changes in the composition, size, and structure of the dust grains that are not observed, as well as polarisation in the absorption lines, which has also been ruled out to a level of less than 0.01% for 45 DIBs (Cox et al. 2011).

The most supported hypothesis concerning the composition of DIBs is that the carriers are large gas-phase molecules. Evidence for this includes the complex component structure of several DIBs, which are reminiscent of molecular rotational band profiles (Kerr et al. 1996). Potential carriers include the polycyclic aromatic hydrocarbon (PAH) molecules, which are known to be abundant in space from their mid-infrared bands (Allamandola et al. 1989; Salama et al. 1996; Meeus et al. 2001). Several hundred DIBs have been identified in the interstellar medium (ISM), including in the Milky Way (e.g. Hobbs et al. 2009), and in nearby galaxies such as the Andromeda Galaxy (Cordiner et al. 2011), Messier 33 (Cordiner et al. 2008) the Large Magellanic Cloud (LMC; Cox et al. 2006) and the Antennae Galaxies (Monreal-Ibero et al. 2018).

Identifying the carriers via laboratory experiments is difficult, as there are more than 1.2 million different species of PAHs with 100 or less carbon atoms that would need to be tested (Cami et al. 2018). The only DIBs to have been convincingly assigned to a carrier are two (possibly four) DIBs, due to ionised buckminsterfullerene C_{60}^{+} (Campbell et al. 2015, 2016; Kuhn et al. 2016; Cordiner et al. 2017, 2019; although, see discussion by Galazutdinov et al. 2017b; Lallement et al. 2018).

Most studies of DIBs have concentrated on optical wavelengths (e.g. Merrill & Wilson 1938; Raimond et al. 2012; Cox et al. 2017)[1]. However, laboratory measurements show that larger PAHs (more carbon atoms) have their strongest absorption lines in the near-infrared (NIR; Mattioda et al. 2005; Ruiterkamp et al. 2005). Indeed, several DIBs have been observed in this region (Joblin et al. 1990; Geballe et al. 2011; Rawlings et al. 2011; Cox et al. 2014; Elyajouri et al. 2017). These include twenty NIR DIBs that have been identified in observations of nine stars at a spectral resolving power (R) of ~10 000 between 950 and 2500 nm (Cox et al. 2014). No DIBs were found redwards of ~1800 nm. The strongest correlations were found between the equivalent widths (EWs) of some NIR DIBs (e.g. that at 1318.1 nm) and the optical DIB at 5780 Å (correlation coefficient $r = 0.98$). Additionally, many NIR DIBs were also found to correlate with reddening with $r \sim 0.9$.

Studies investigating the 1527 nm DIB on a statistical basis towards ~60 000 mainly late-type stars at $R \sim 22\,000$ used data from the APOGEE survey (Zasowski et al. 2015b). These studies have shown that this DIB persists in the ISM for long timescales and correlates with dust but has a scale height above the Galactic plane of ~100 pc, twice that of dust. Elyajouri & Lallement (2019) also investigated this DIB using a larger sample from the APOGEE survey, providing measurements for 124 064 sightlines and demonstrating that the carrier is concentrated in the outskirts of interstellar clouds. Hamano et al. (2015, 2016) presented DIB observations from 0.91–1.32 μm at $R = 28\,000$. They concluded that the 1078.0, 1079.2, and 1179.7 nm features likely belong to related carriers and correlate with the 5780 Å DIB. Galazutdinov et al. (2017a) studied fourteen DIBs in the 1.45–2.45 μm range and measured basic correlations between the observed bands. Elyajouri et al. (2017) confirmed several weak DIBs and found that the 1527 nm DIB is most abundant in diffuse interstellar clouds with low density and high ultraviolet radiation fields (known as σ-type clouds, with ζ-type clouds having opposite properties). Hamano et al. (2022) looked at DIBs in the Y and J bands, postulating that DIBs at longer wavelengths are caused by larger molecules. Finally, Ebenbichler et al. (2022) observed four stars at $R = 100\,000$ with CRIRES to confirm 17 new DIBs and identify a possible 12 additional DIBs.

We seek to extend previous work by observing multiple NIR DIBs at high spectral resolving power ($R \sim 50\,000$) and to better constrain the known correlations using data of higher signal-to-noise ratios. Some optical DIBs are known to vary on small scales in the ISM (see Sect. 4.5 for references), so we also searched for small-scale structures in the NIR DIBs. No optical DIBs are known to vary (convincingly) with time, but even so we also searched for time variability in the NIR DIBs using twin epoch observations of a number of sightlines.

This paper is organised as follows. Section 2 describes our sample of targets, observations, data reduction, and telluric line removal. Section 3 outlines the analysis of the data, including profile fitting. The discussion is presented in Sect. 4, which includes discrimination between stellar and interstellar or circumstellar features, the shape of the DIB profiles, a comparison of NIR DIB line strengths with optical DIBs, atomic lines and reddening, and finally a search for small scale structure and time variability in the NIR DIBs studied. In Sect. 5, we summarise our results and make suggestions for future work.

2. Sample, observations, and data reduction

2.1. The Sample: CRIRES observations and data reduction

Most of the sample was observed using CRIRES (Kaeufl et al. 2004), mounted on the 8.2-m Unit Telescope One (Antu) at the Very Large Telescope (VLT) under programme IDs 091.C-0655 (epoch 1) and 093.C-0480 (epoch 2). In epoch 1, the central wavelengths on detector three (of the four CRIRES detectors) were a combination of one or more of 1318.1 nm, 1574.4 nm, and 1624.2 nm. In epoch 2 we observed far fewer stars but also included 1527.0 nm and 1568.8 nm settings for a few sightlines. The wavelength coverage in each setting was small, ranging from 31 nm for the 1318.1 nm setting to 37 nm for the 1624.2 nm setting, with gaps of around 2 nm between the four detectors on the mosaic. The vacuum wavelengths observed for each star are listed in Table A.1. Observations were scheduled during poor weather conditions, so we used the widest slit possible with CRIRES, 0.4 arcsec, and no adaptive optics for the majority of the stars, yielding a resolving power of $R \equiv \lambda/\Delta\lambda \sim 50\,000$, as measured from the telluric lines.

The CRIRES sample includes observations of 67 O-type and B-type stars (median magnitude in the H-band of 5.9) between April and September 2013, and follow-up observations of 17 stars between March and June 2014. The latter group were

[1] In this paper, we use angstroms for DIBs bluewards of 1000 nm and nm for redder wavelengths.

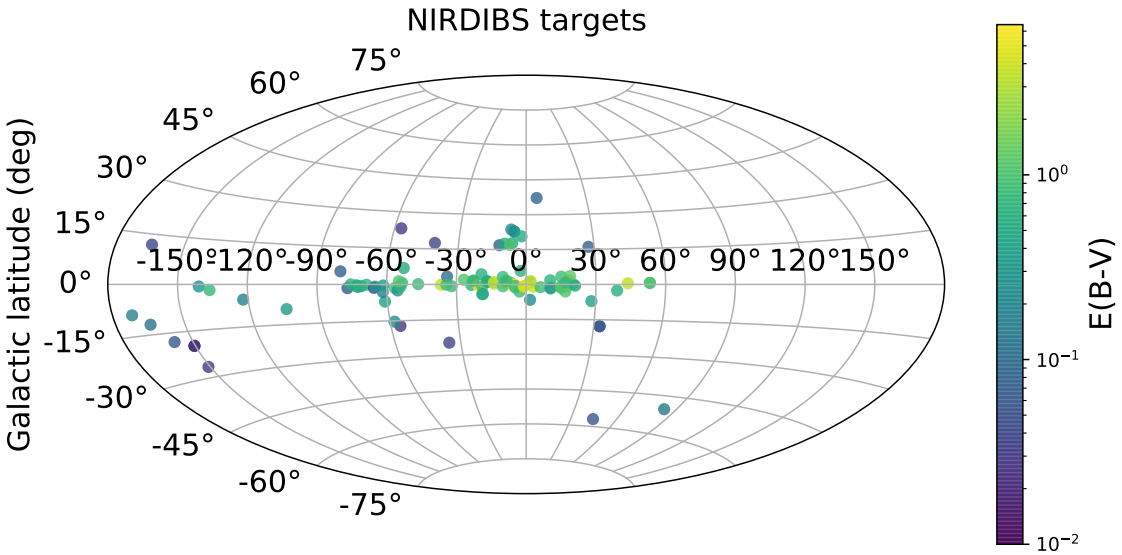

Fig. 1. Distribution of the sample in Galactic coordinates, colour-coded by reddening. Most targets are close to the Galactic plane, with the highest reddenings near the Galactic Centre.

either repeat observations of stars observed in the first epoch (to search for time-varying DIB strength), or observations of companion stars in double or triple systems, in which case the intention was to search for small-scale structures in the ISM. The total sample comprised 76 stars. We favoured early-type stars as they typically have few stellar lines at the wavelengths of the NIR DIBs and are often fast rotators (e.g. Stütz et al. 2006), making it easier to distinguish between stellar and interstellar features. The CRIRES-observed sightlines have interstellar reddening ranging from $E(B-V) \simeq 0$ to $\simeq 1.5$ mag, estimated from their observed $(B-V)$ colours and the intrinsic colour of the relevant spectral type taken from Fitzgerald (1970) and Wegner (1994).

Total integration times ranged from 60 s to 1200 s, depending on target brightness, with a median of 600 s. An ABBA nodding pattern was used to facilitate sky subtraction. For a handful of targets that had close companions, adaptive optics was used to separate the components. Data were reduced using the original CRIRES data reduction pipeline[2] utilising instrument calibration data taken the morning after the observations and including a correction for detector non-linear response. The initial wavelength calibration was performed using exposures of a ThAr lamp, then refined during telluric correction (see below). The median S/Ns of the reduced spectra in the 1318.1 nm setup were ~300 per pixel (~550 per resolution element) with similar values for the other wavelength settings.

2.2. X-shooter observations and archival data

To increase the range of E(B-V) sampled in this study, X-shooter (Vernet et al. 2011) spectra of ten stars with $m_J < 16.0$ mag. were taken from Minniti et al. (2020), who studied Cepheid variables towards the Galactic Centre. The S/Ns were between ten and 50 per pixel at 1318 nm and higher at 1527 nm, with $R \sim 8000$. These targets have extinction in the Ks band ranging from 1.13 to 2.25 mag, corresponding to $E(B-V)$ values between 3.13 and 6.51 (A_V from ~9.7 to 20.2), assuming the extinction law of Cardelli et al. (1989). Their distances range from 8.0 to 31.5 kpc.

Additionally, four stars were observed with X-shooter under dry weather conditions (precipitable water vapour (PWV) of less than 0.5 mm) with the aim of searching for time variation in the C_{60}^{+} and NIR DIBs. Finally, we downloaded reduced spectra for a further 19 X-shooter targets from the ESO archive to investigate the dependence on NIR DIB strength with fractional H_2 content. Figure 1 shows the distribution of the sample across the sky for the CRIRES and X-shooter spectra, and Table A.1 lists basic information for all the observed stars.

2.3. Telluric correction

Correction for telluric lines was performed using the MOLECFIT package[3] (Smette et al. 2015). The PWV was fitted by the code. Example spectra before and after telluric line correction are shown in Fig. 2 in two wavelength settings, each at low (0.2 mm) and high (6.0 mm) PWV.

3. Data analysis

The data analysis was straightforward and consisted of normalising the spectra with polynomials of order three to four for either side of the DIB features and measuring the EWs and the full-width half-maximum (FWHM) velocity widths by fitting Gaussians to the detected components. Errors were calculated according to Eq. (10) of Ebbets (1995). Data were transformed to the heliocentric restframe using RV[4]. Where the expected DIBs were not detected, five sigma upper limits to the EWs were estimated according to:

$$\mathrm{EW}_{\mathrm{upperlim}} = 5.0 \times \frac{\sqrt{N_s} \times \Delta\lambda}{S/N},$$

where S/N is the signal-to-noise ratio (S/N) per pixel, $\Delta\lambda$ is the width of each intensity sample in angstroms, and N_s is the number of samples. The derived errors were compared with those estimated in twelve cases where the same star was observed on different nights. The standard deviation on the measurements is

[2] https://www.eso.org/sci/software/pipelines/crires/crires-pipe-recipes.html

[3] http://www.eso.org/sci/software/pipelines/skytools/molecfit

[4] http://www.starlink.ac.uk/docs/sun78.htx/sun78.html

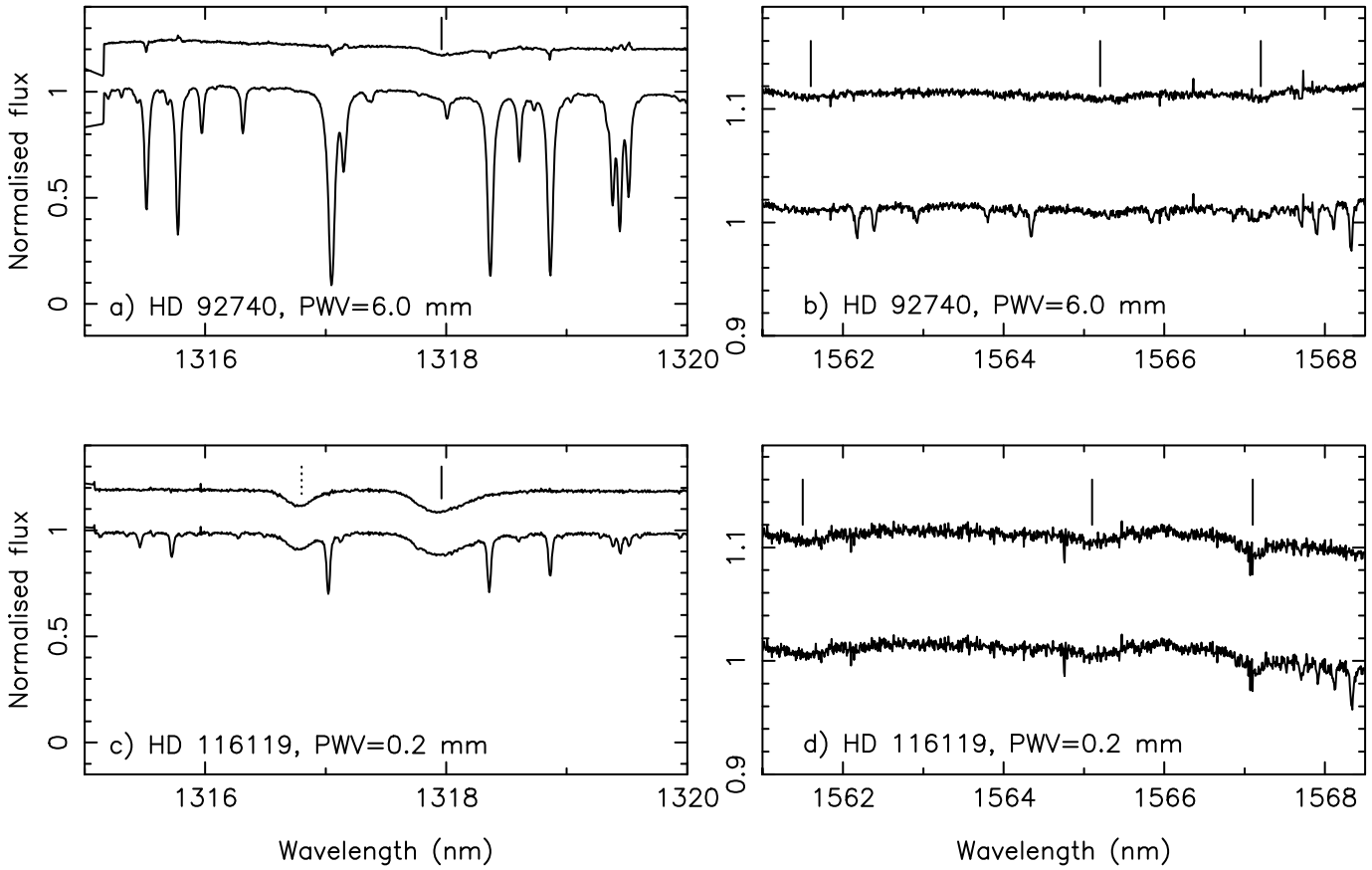

Fig. 2. Examples for two wavelength regions of the use of MOLECFIT to remove telluric lines from spectra when the PWV was ~6.0 mm (plots *a* and *b*) and ~0.2 mm (plots *c* and *d*) for HD 92740 and HD 116119. Spectra have been normalised. The median nighttime PWV for Paranal is 2.4 mm (Kerber et al. 2014). The lower spectra in each panel are the reduced data. The upper spectra are the same objects after telluric correction (offset in the ordinate for clarity). Vertical lines above the corrected spectra indicate the DIBs at 1318.1, 1561.1, 1565.1, and 1567.0 nm. Vacuum wavelengths are shown. The dashed vertical line displayed for HD 116119 at a wavelength of 1316.8 nm indicates a likely stellar feature caused by an O I triplet.

8% ($N = 12$) for EWs $\gtrsim$150 mÅ. The largest difference in measurements at different epochs is 23%, towards HD 145482 with a (small) EW of ~40 mÅ for the 1318.1 nm line.

Excluding the handful of sightlines contaminated by stellar lines, the detection rates for the DIBs approached 90% for the 1318, 1561.1, 1565.1, and 1567.0 nm features. Finally, no clear DIBs were detected in the CRIRES setting around 1624.2 nm. Table C.1 shows the EW results for the current sample as well as the 5780 and 5797 Å DIBs from optical spectra discussed in Sect. 4.3.

4. Discussion

We detected a total of 23 non-telluric features, of which 17 are likely to be stellar and six are likely to be interstellar (or possibly circumstellar) in nature. Figure 3 shows examples of each, with all spectra being shown in Fig. B1. These are discussed in turn. Table 1 shows all of the detected lines.

4.1. Likely stellar features

A number of likely stellar features are listed in the spectra in Table 1, with examples shown in Fig. 3. We classified lines as being stellar based on their width compared with other metallic stellar lines. For these lines, we also searched the National Institute of Standards and Technology (NIST) database[5] for close matches in wavelength.

4.1.1. 1315.4 nm (absorption)

This line is seen in only two stars in our sample, HD 145501 B and HD 147932 (B5V). The estimated vsin(i) for HD 147932 is 153 km s^{-1} (Brown & Verschueren 1997), although this was perhaps affected by a secondary component that makes the spectrum difficult to analyse. HD 145501 B is a magnetic chemically peculiar star of type CP2 (Kochukhov & Bagnulo 2006; Wraight et al. 2012, and references therein), and HD 147932 is also a magnetic (and rotationally variable) star (Alecian et al. 2014).

4.1.2. 1316.5 nm (emission)

A weak emission line is seen in a handful of the early-type stellar spectra. These include the blue supergiants HD 115363 (B1Ia), HD 148688 (B1Ia), HD 152235 (B0.5 Ia), and HD 159455 (B0.5Ia). The FWHMs from single-component Gaussian fits to the observed lines are 59 km s^{-1} for HD 115363, 61 km s^{-1} for HD 148688, 92 km s^{-1} for HD 152235, and 66 km s^{-1} for HD 159455 although the feature does not appear Gaussian in this case. The lines observed (if stellar) are likely to be formed at the

[5] See https://physics.nist.gov/PhysRefData/ASD/lines_form.html

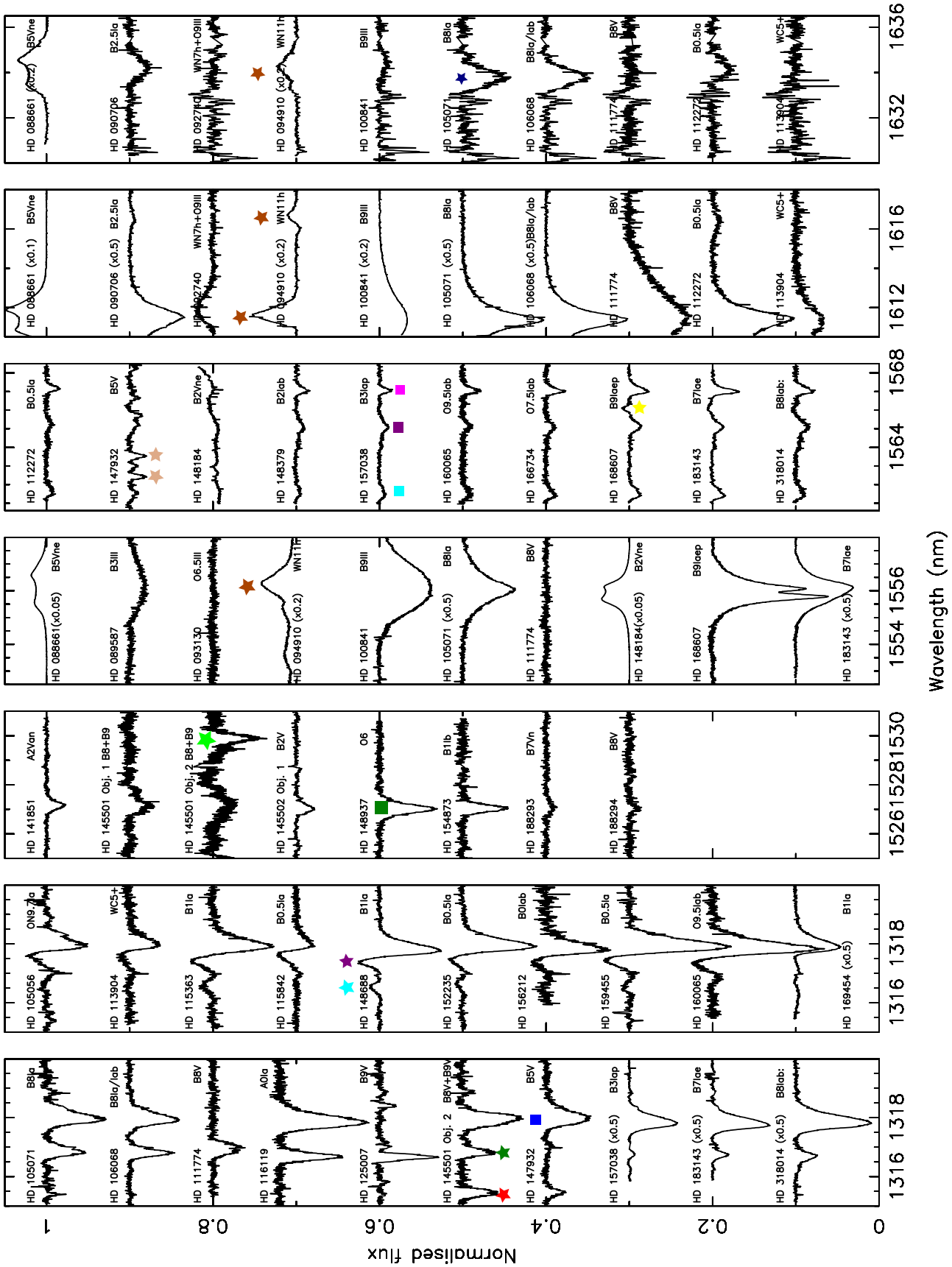

Fig. 3. Normalised CRIRES spectra showing examples of observed stellar and interstellar features. The ordinate is the normalised flux plus an offset with the abscissa as the wavelength in nm. Stellar lines: Red stars: 1315.4 nm; Green: 1316.8 nm; Cyan: 1316.5 nm (EmL); Purple: 1317.3 nm (EmL, uncertain); Light Green: 1529.9 nm; Yellow: 1566.1 nm (EmL); Gold: 1563.0 and 1563.5 nm; Navy: 1633.8; Brown: 1555.7, 1610.9, 1616.7, and 1634.2 nm (EmL). Not shown: 1562.4 nm, 1625.3 nm and 1626.1 nm features. DIBs: Blue squares: 1318.1 nm; Green: 1527.1 nm; Cyan: 1561.1 nm; Purple: 1565.1 nm; Pink: 1567.0 nm. Not shown: broad and weak feature around 1564.4 nm.

Table 1. Rest wavelengths in vacuum of lines detected in the CRIRES spectra.

λ (nm)	Stellar or IS	Abs. or EmL	Notes	Lines from the NIST database within ±0.2 nm
1315.4	S	Abs.	(1)	Zn I (1315.42 nm), Al I (1315.43 nm), Th I (1315.45 nm), Fe I (1315.52 nm) Fe I (1315.52 nm), Cs II (1315.53 nm)
1316.5	S	EmL	(2)	C I (1316.42 nm), Fe II (1316.60 nm), Fe II (1316.65 nm), Cs II (1316.68 nm)
1316.8	S?	Abs.		O I (1316.75, 1316.85, 1316.87 nm), Fe II (1316.82 nm)
1317.3	S	EmL	(3)	Th I (1317.14, 1317.19 nm), Fe I (1317.39, 1317.42 nm), V I (1317.43 nm), Th II (1317.52 nm)
1318.1	IS	Abs.	DIB	Th I (1317.97, 1318.20 nm), Si I (1318.05 nm), Fe I (1318.06 nm) Kr I (1318.10 nm), Ti I 1318.20 nm), Th II (1318.29 nm), V I 1318.29 nm)
1527.0	IS	Abs.	DIB	Cr II (1526.97 nm), Fe I (1526.84, 1527.12 nm), Kr I 1527.01 nm), Fe II (1527.10 nm)
1529.9	S	Abs.	(4)	Th II (1529.72 nm), Fe II (1529.73, 1529.87, 1529.90, 1529.98 nm), Cs II (1529.80 nm), V I (1529.82 nm), Th I (1529.93, 1529.98, 1530.04 nm), Fe II (1529.98 nm), Hg I (1530.00 nm), Fe I (1530.00, 1530.03, 1530.06, 1530.10 nm)
1555.7	S	Abs. & EmL	Br line	Fe I (1555.64, 1555.78, 1555.88 nm), Th I (1555.59, 1555.74 nm), Ti II (1555.63 nm), Fe II (1555.81 nm)
1561.1	IS	Abs.	DIB	Ti I (1560.91, 1560.94 nm), Fe II (1560.96 nm), Cr II (1561.14 nm), Al II (1561.14 nm) Th I (1561.24 nm)
1562.4	S	Abs.	(4)	Se I (1562.27 nm), Ti II (1562.38 nm), Th I (1562.44 nm), Fe II (1562.54, 1562.59 nm)
1563.0	S	Abs.	(4)	Fe II (1562.84 nm), Th II (1562.89 nm), B I (1562.90 nm)
1563.5	S	Abs.	(4)	B I (1563.33 nm), Fe I (1563.36, 1563.39, 1563.53 nm, Th II (1563.58 nm)
1564.4	???	Abs.	Weak	Fe I (1564.32, 1564.38 nm), Th II (1564.47, 1564.56, 1564.61 nm), V I (1564.47 nm), Fe II (1564.52 nm)
1565.1	IS	Abs.	DIB	Fe I (1564.92, 1565.28 nm) Fe II (1564.96, 1565.21 nm) Ar II (1565.21 nm)
1566.1	S	EmL	(5)	V I (1566.1 nm), Fe I (1566.2 nm)
1567.0	IS	Abs.	DIB	Ti I (1566.05 nm), V I (1566.07 nm)
1610.9	S	Abs. & EmL	Br. line	Ti I (1619.73, 1610.99, 1611.03 nm), Th I (1610.84, 1610.98 nm), Ar II (1610.94 nm)
1616.4	S	Abs.		Ti I (1616.21, 1616.47, 1616.56), Be I (1616.21) Fe I (1616.21, 1616.34 nm), Fe II (1616.31, 1616.39 nm)
1616.7	S	Abs. & EmL	(6)	Ti I (1616.56, 1616.84 nm), Fe I (1616.72 nm), Th II (1616.78 nm), Si I (1616.81 nm)
1625.3	S	EmL		Al II (1625.11, 1625.23 nm), Fe I (1625.14, 1625.33 nm)
1626.1	S	EmL	–	Fe I (1625.91 nm), P I (1625.92 nm), Fe I (1625.34 nm), Ti I (1626.37 nm)
1633.8	S?	Abs.		Fe II (1633.74 nm), Fe I (1633.76 nm), C I (1633.84 nm)
1634.2	S	EmL	–	Fe I (1634.16 nm)

Notes. We also show lines taken from the NIST database within ±0.2 nm in vacuum wavelength. (1) Only observed in magnetic stars. (2) Only observed in blue supergiants. (3) Observed in B2 and earlier spectral types. Contaminates 1318.1 nm DIB. (4) Only observed in one magnetically peculiar star. (5) Only observed in blue supergiant and emission-line stars. (6) Only observed in blue supergiant and Wolf–Rayet stars.

base of the wind, close to the photosphere, and the broadening they display is basically caused by rotation and macroturbulence. Hence the line broadening does not measure the wind terminal speed. The FWHM of the lines are broadly consistent with this picture and indicate that the lines do not form in the stellar wind as if they did they would be much broader (Vink & Sander 2021). We also note that in the case of HD 152235, the Hα line at 6556 Å is approximately twice as wide (in km s^{-1}) as the infrared emission line. Finally, the difference in the wavelengths of the peak emission of the 1316.5 nm line and 1317.3 nm lines is not the same for the HD 152235 and HD 159455 sightlines, although the measurement is difficult.

4.1.3. 1316.8 nm (absorption)

This line is seen in several stars that are typically late B-types: HD 105071 (B8Ia), HD 106068 (B8Ia), HD 115088 (B9.5), HD 116119 (A0Ia), HD 111774 (B8V), HD 125007 (B9V), HD 145501 (B8), HD 157038 (B3 Iap), HD 164865 (B9Ia), HD 183143 (B6Ia), and HD 318014 (B8Ia). The measured

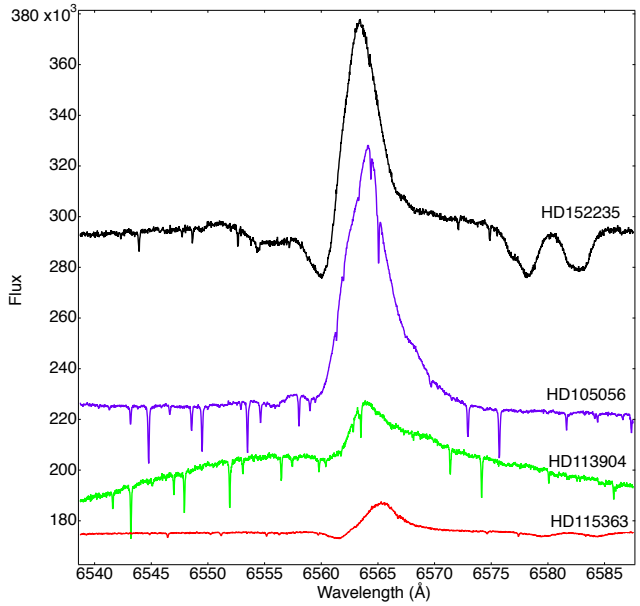

Fig. 4. Archival UVES spectra showing Hα emission for four stars towards which an emission feature is also seen near to the 1318 nm DIB.

FWHMs range from 44 km s^{-1} for HD 157038, with a FWHM of 50 km s^{-1} from Si III (4567 Å), to 71 km s^{-1} for HD 105071, which has somewhat lower FWHMs in the optical of 55 km s^{-1} (Si II 4128 and 4130 Å) and 48 km s^{-1} (N II 3995 Å) from archival spectra from the Ultraviolet and Visual Echelle Spectrograph (UVES; Dekker et al. 2000; Smoker et al. 2009). Malkan et al. (2002) noted the presence of a blend of Al I at 1312.6 nm and Si I at 1318.0 nm in cooler stars, although this was only detectable in their data for stars of type A4 or later.

Finally, HD 111774 has a FWHM of 100 km s^{-1} for visible lines at 4549 and 4555 Å, while the NIR line has a FWHM of 88 km s^{-1}. Overall, although there are a few discrepant values, the FWHM values indicate that this line is stellar and not interstellar. There is no correlation between the line strength and reddening for these sightlines.

4.1.4. 1317.3 nm (possible stellar emission merged with DIB causing inverted P-Cygni profile)

A number of sightlines show inverted P-Cygni-like profiles around 1317.3 nm, bluewards of the main DIB at 1318.1 nm. Such emission lines were predicted in solid state carriers associated with a red wing by Van de Hulst (1948). The features are weakly visible in the X-shooter spectra of Cox et al. (2014), although they are not commented on and much more obvious with the current higher spectral resolution data. The Wolf–Rayet stars in the Galactic Centre observed by Najarro et al. (2017) do not show this emission line at 1317.3 nm, although the resolving power of those data is again only R = 1200–5000, so it would be difficult to detect (though they do clearly detect the 1318 nm DIBs).

As the features are present mainly in stars of spectra of type B2 and earlier, there is a strong likelihood that we are in fact seeing a mix of a stellar emission line in hot stars combined with the interstellar DIB at 1318.1 nm. A search for emission lines in UVES spectra towards a handful of these objects showing the 1317.3 nm emission line feature revealed strong Hα (Fig. 4). We note that one-third of our sample has spectral types later than B2, in which no inverted P-Cygni profiles are seen.

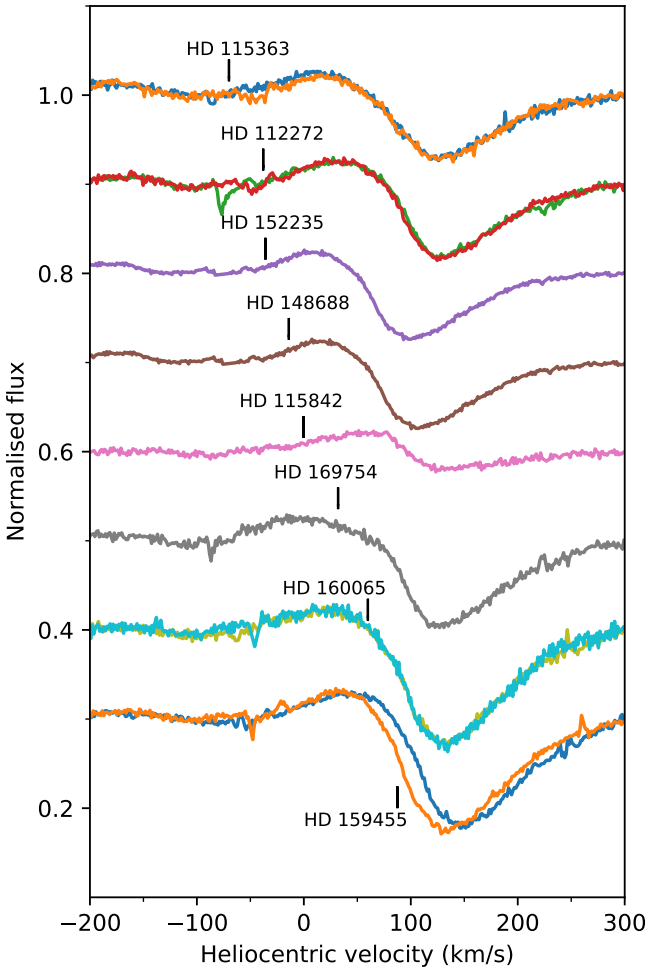

Fig. 5. Example spectra showing the bluewards emission feature towards the 1318 nm DIB with heliocentric stellar velocities marked by vertical black lines. For HD 115363, HD 112272, HD 159455, and HD 160065, two spectra taken at different epochs are shown. HD 159455 has a shift in radial velocity between the two epochs. Kervella et al. (2019) use *Gaia* data to determine that this object has a tangential velocity anomaly of 2.4 km s^{-1} and is hence likely a binary, although this should not affect the DIB absorption profile. The rest wavelength of the emission line is assumed to be 1317.30 nm.

To investigate the nature of the emission, we (a) compared the emission line velocities with stellar and DIB velocities and (b) computed a model spectrum of the region for an early B-type star. For the comparison, we determined the stellar velocities of the sightlines where the emission feature was seen, either using values from the literature or our own measurements from archive data. Figure 5 shows spectra of eight stars with emission lines bluewards of 1318 nm with their stellar velocities indicated.

Of particular interest are three stars, HD 115363, HD 159455, and HD 160065, which have heliocentric radial velocities of −70, +88 and +60 km s^{-1}, respectively. If the emission lines were at the stellar velocities, then one would expect an offset of approximately 0.7 nm (158 km s^{-1}) between the position of the emission line peaks when comparing HD 115363 and HD 159455. Similarly, the offset between the emission line peak from the star and the absorption line trough from the DIBs would also be expected to change. The fact that the emission-absorption offset, 0.51 nm for HD 115363 and 0.46 nm for HD 159455, is similar for both stars could indicate that the emission line does not move at the stellar velocity.

Table 2. Emission line around 1318 nm.

HD Number	Stellar velocity (km s^{-1})	Ref.	MJD	EmL, Abs. Wavelength (nm) at |peak|	$\delta\lambda$ (nm)	EmL, Abs. norm. flux peak (abs. value)	Hel. RV corr (km s^{-1})
105056	+5±6, –9.0±3.1,	(1), (4)	56411.272	1317.56, 1317.95	0.39	1.020, 0.955	+2.4
"	+14.5 ±1.8	(5)		(1317.61, 1318.05)	0.44		
112272	–36±2, –38.0±4.4	(1)	56440.172	1317.46, 1317.89	0.43	1.025, 0.918	–6.0
"	–37.1±1.8	(5)		(1317.47, 1318.02)	0.55		
"			56732.333	1317.38, 1317.79	0.41	1.025, 0.917	+14.7
"				(1317.39, 1317.92)	0.53		
113904	+7±5, +4.4±1.5	(1), (5)	56459.143	1317.56, 1317.97	0.41	1.010, 0.965	–10.5
"				(1317.58, 1318.07)	0.49		
115363	–70±2, –71.0±4.5	(1), (4)	56465.029	1317.41, 1317.92	0.51	1.023, 0.929	–12.4
"	–70.4±1.4	(5)		(1317.39, 1318.02)	0.63		
"			56732.346	1317.30, 1317.80	0.50	1.021, 0.929	+15.8
"				(1317.31, 1317.90)	0.59		
115842	–21±2 –3.0±4.3	(1), (4)	56465.058	1317.61, 1317.95	0.34	1.020, 0.980	–15.7
"	–21.1±1.7	(5)		(1317.57, 1318.07)	0.50		
152235	–25±1, –35.2±2.3	(1), (4)	56467.098	1317.43, 1317.91	0.48	1.015, 0.913	–7.2
"	–35.9±1.8	(5)		(1317.50, 1318.01)	0.51		
159455	87.5±1.9	(2)	56435.263	1317.44, 1317.90	0.46	1.029, 0.880	+11.5
"				(1317.46, 1318.00)	0.54		
"			56764.186	1317.33, 1317.78	0.45	1.032, 0.875	+25.4
"				(1317.34, 1317.93)	0.59		
160065	59.9±6.4, 10.4±2.7	(2), (6)	56434.396	1317.33, 1317.83	0.50	1.022, 0.873	+12.0
"				(1317.32, 1317.94)	0.62		
"			56746.394	1317.27, 1317.75	0.48	1.022, 0.870	+29.7
"				(1317.22, 1317.68)	0.46		
169754	32.0±7.4	(3)	56497.240	1317.34, 1317.91	0.57	1.025, 0.904	–12.4
"				(1317.37, 1318.04)	0.67		

Notes. Stellar velocities, velocity of the peak of the emission line and velocity at peak of absorption line towards stars where the 1318 nm showed strong emission. The standard of rest is heliocentric. Values in brackets are flux weighted wavelengths determined using fitting as shown in Fig. 7.
References. (1) POP, UVES pop survey (Bagnulo et al. 2003); (2) *Gaia* DR2; (3) Kharchenko et al. (2007); (4) Gontcharov (2006); (5) This paper with the stellar velocity measured using He I at λ = 4387 Å; (6) *Gaia* DR3 (Gaia Collaboration 2023). There is a large (50 km s^{-1}) difference in the *Gaia* DR2 and DR3 velocities for the one star (HD 160065) for which data are available for both releases.

To investigate this further, Fig. 6 shows (a) the difference in emission and absorption line velocities, (b) the difference in stellar and emission line velocities, and (c) the emission line velocity, all plotted against the stellar velocity. The simple trough or peak of the absorption or emission lines were used for the velocity measurements and are shown in Table 2. Additionally, we performed a fit to the data comprised of an emission line component and a 1318 nm DIB profile taken from Fig. 12 shifted in wavelength, scaled in flux, and stretched in wavelength by up to 5%. The weighted wavelength was derived for the two components by averaging the wavelength bins weighted by the absolute value of the absorption line depth, $f(\lambda)$ vis:

$$\lambda_{\rm weighted} = \frac{\int ((1.0 - f(\lambda) \times \lambda))\, {\rm d}\lambda}{\int \lambda\, {\rm d}\lambda}. \quad (1)$$

The values of the Gaussian fit wavelengths are also included in Table 2. Figure 7 shows the model for two stars (HD 115363 and HD 159455) as well as the data and model residual.

The emission line minus absorption line velocity difference plotted against stellar velocity is shown in Fig. 6a. There is no strong correlation between the velocities, which indicates that the emission and absorption line components could be formed in the same medium. A priori, if the emission line were stellar in nature, it should be correlated with the stellar velocity. However, Fig. 6c implies that this is not the case. Indeed, Fig. 6b shows that the difference in the stellar and emission line velocity is correlated with the stellar velocity when a constant offset may have been expected. We caution that measuring the centre of the emission peak is not straightforward, and these errors could dominate.

A final attempt to determine the origin of the line was performed by computing a stellar model of a B0.5Ia blue supergiant star HD 152235 using CMFGEN (Hillier & Lanz 2001) and comparing it with observations. A solar metalicity was assumed as well as an effective temperature of 21 800 K, log(g) = 2.55, and a slightly enhanced He/H=0.135 by number compared with the standard value of ∼0.1. In Fig. 8 we show the emission and absorption lines from the X-shooter data and our model in the 1075 to 1105 nm region. In particular, the model predicts emission from the He I P-Cygni profile line at 1083 nm with an EW of 820 mÅ (integrated from 1072 to 1090 nm), which is somewhat lower than the observed value of 1660±100 mÅ. The corresponding integrated line strengths for the model and data for the absorption line doublet at 1091.6 and 1092.0 nm are 1000 and 1180±70 mÅ. Finally, for the Hydrogen Paschen

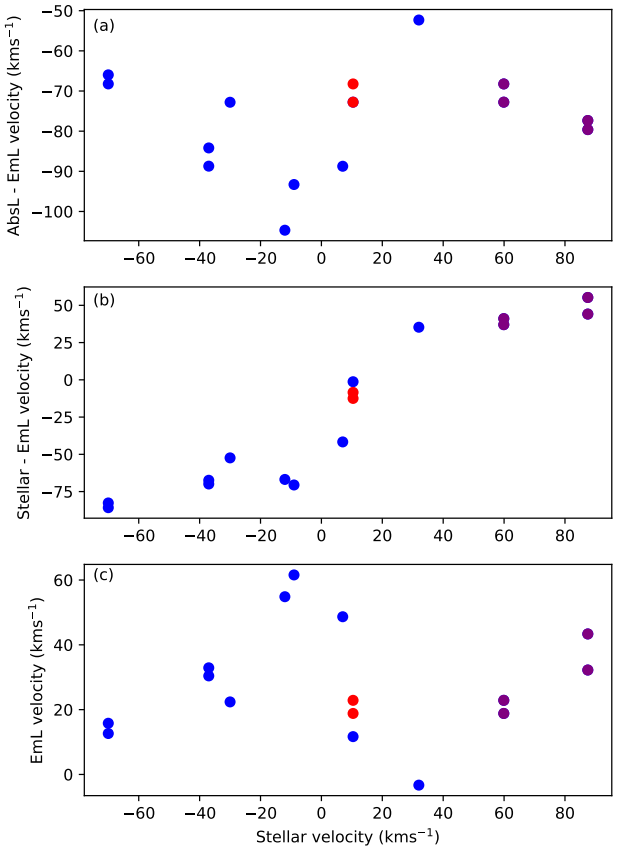

Fig. 6. (*a*) Difference in absorption and emission line peak velocity around 1318 nm plotted against the stellar velocity. (*b*) The same for stellar velocity minus emission line velocity. (*c*) Emission line velocity versus stellar velocity, assuming the emission line has a rest wavelength of 1317.37 nm. Results with the same stellar velocities are from repeat observations of a given star. Purple points are from *Gaia* DR2 with Red points from *Gaia* DR3 for HD 160065.

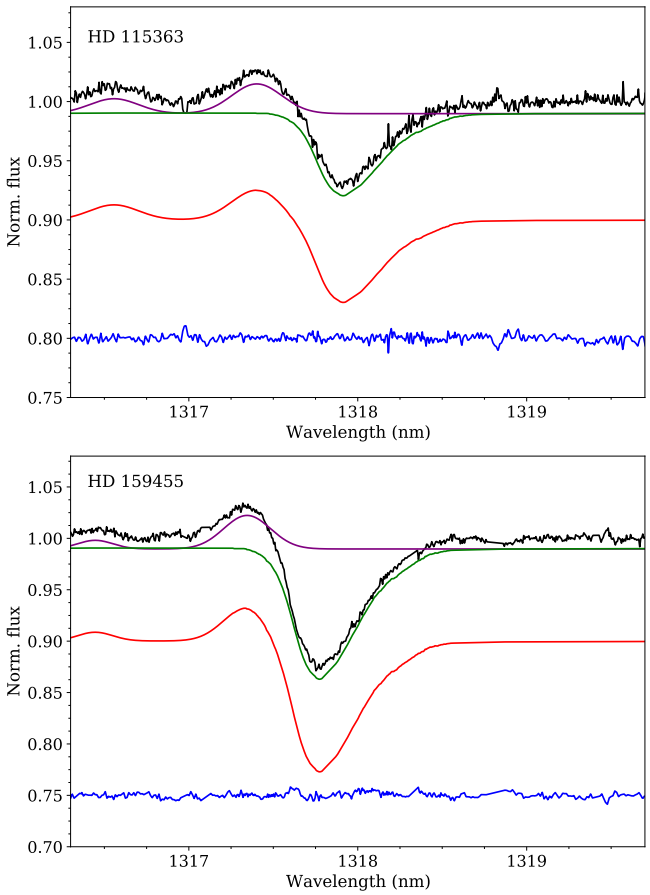

Fig. 7. Normalised absorption and emission around 1318 nm towards HD 115363 (B1 Ia) and HD 159455 (B0.5 Ia). Black lines: Data. Purple lines: Twin-component Gaussian fits to the unidentified emission lines. Green line: Scaled, shifted, and wavelength stretched absorption line DIB profile. Red line: Combined Gaussian fit plus DIB model. Blue line: Data divided by model. Lines are offset in the ordinate for clarity.

line at 1094.0 nm, the model and data have EWs of 2700 and 2750±100 mÅ respectively.

Figure 9 shows the stellar model and CRIRES or X-shooter data for HD 152235 for the DIB regions studied in this paper plus the 1078 and 1080 nm DIBs studied by Cox et al. (2014). Panel (c) of this figure shows that the model only predicts a very weak emission (5 mÅ) in the bluewards emission P-Cygni feature of the 1318 nm DIB compared with the actual value of 40±5 mÅ, indicating a non-stellar nature. Although the model also predicts lower values for emission in the 1075–1090-nm regions the difference is less pronounced than for the 1317.3 nm feature. Given the weakness of the predicted emission compared to what was observed, a perhaps more intriguing possibility is that we are seeing a PAH emission near the hot star, turning to absorption further out. Such behaviour has been claimed towards the Red Rectangle in the DIBs around 5797Å (Fossey 1991, Sarre 1991 although see Glinski et al. 2009). The lack of an emission line feature in later stars in this scenario would be explained by a higher UV flux from the earlier-type stars. However, such emissions would require a large amount of cooler and dustier circumstellar material. Additionally, Sect. 4.3 and previous work such as that by Hamano et al. (2015, 2016) show that the 1318 nm DIB acts more like a 5780 Å DIB than the 5797 Å DIB variety, and in the Red Rectangle no emission is seen around 5780 Å. Furthermore, in the Red Rectangle the emission is redwards, not bluewards of the DIB at 5797 Å. Hence it seems unlikely that we are seeing a PAH emission from the DIB although confirmation would require follow-up observations of the Red Rectangle using for example the upgraded CRIRES or X-shooter. We note that circumstellar absorption has been claimed for the 1527 nm DIB towards the Red Square Nebula by Zasowski et al. (2015a). Figure 7 shows two emission line features towards HD 115363 at around –200 and +25 km s^{-1}, that could be explained by circumstellar material rotating the central star and that could produce a double peak in velocity. However, the strengths of the two peaks are different and emission line velocities are not symmetric about the stellar velocity of 70 km s^{-1}.

In conclusion, our finding that the emission is only seen in stars of B2 or earlier and that these stars also show Hα in emission suggests a stellar or circumstellar origin for the line. However, the fact that the emission line is stronger than predicted by a stellar model and there is a lack of obvious correlation between the emission line wavelength and the stellar velocity points to the line being interstellar. To conclusively eliminate an ISM or circumstellar nature would need an investigation into the wind speed of the targets.

4.1.5. 1529.9 nm (absorption line)

A single sightline, the magnetically chemical peculiar star HD 145501 (B8V+B9VpSi), displays an absorption line at

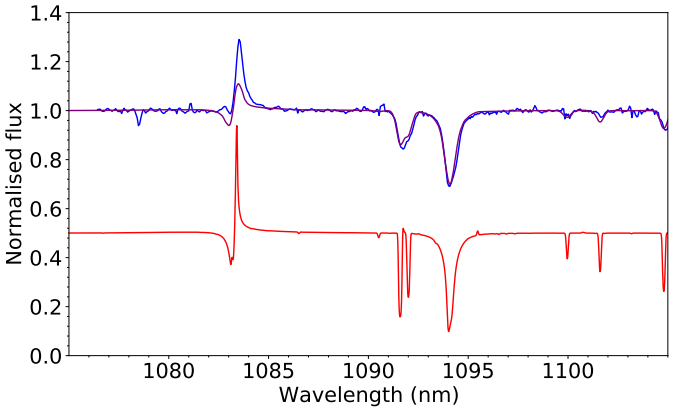

Fig. 8. Blue line: X-shooter data of HD 152235 from 1075 to 1105 nm showing an emission line from the star at 1083 nm (He I) and absorption at 1094 nm (H I). Red line: Stellar model in vacuum wavelength obtained using CMFGEN of a B0Ia star of solar metalicity, $T_{\rm eff}$ = 21 800 K, log(g) = 2.55, and slightly enhanced He/H = 0.135 by number, offset in the ordinate for clarity. The purple line shows the model spectrum Gaussian smoothed to a FWHM of 0.91 nm (~250 km s^{-1}) to fit the absorption line data.

1529.9 nm. The line is very likely stellar as this is the only sightline where it is seen in the sample, with the reddening towards the star being $E(B-V)$ = 0.22 mag. The line is not seen in the spectrum of a close companion.

4.1.6. 1555.7 nm (emission and absorption lines)

The 16–4 Brackett line at 1555.65 nm is observed in many spectra[6], both in absorption and emission. The lines have a range of shapes, including strong, symmetric absorption (HD 105071, B8Ia); asymmetric absorption (HD 183143, B7Ia); twin absorption components (possibly from super-imposed central emission in HD 168607, B9 Iaep); and double-peaked emission in the Be-type objects (HD 88661 and HD 148184). However, several stars do not show the line at all (e.g. HD 111774, B8V; HD 93130, O6.5 III).

4.1.7. 1562.4 nm, 1563.0 nm, and 1563.5 nm (absorption)

The B5V star HD 147932 (ρ Oph C) displays several absorption lines around 1563 nm, the strongest being at 1562.4, 1563.0, and 1563.5 nm with FWHM widths of 49 km s^{-1}. This compares with the FWHM of the Mg II line at 4481 Å for the same star of 180 km s^{-1}, indicating that if the lines are stellar they likely originate from a cool spectroscopic binary companion as indicated from *Gaia* observations (Kervella et al. 2019). The star is magnetic (Alecian et al. 2014) and shows possible variability over timescales of 20.7 h (Koen & Eyer 2002) although with possible contamination of the spectra by the brighter ρ Oph (David et al. 2019).

4.1.8. 1566.1 nm (emission)

Weak emission at 1566.1 nm is seen in several sightlines. These include the supergiant and emission-line stars HD 148184 (B2Vne; broad and hard to fit the continuum), HD 168607 (B9Iaep, $FWHM$ = 0.26 nm), HD 183143 (B7Iae; often used as a 'template' for DIBs), and HD 318014 (B8Iab).

4.1.9. 1610.9 nm (absorption and emission)

A number of spectra show absorption near to 1610.9 nm, which is the 13–4 Hydrogen Brackett line. The line sometimes also appears in emission.

4.1.10. 1616.4 nm (absorption line)

An absorption feature at 1616.4 nm is visible in spectra of the supergiant stars HD 112272 (B0.5Ia), HD 148379 (B2Iab), HD 148688 (B1Iae), HD 168987 (B1Ia), HD 169454 (B1Ia), and HD 318014 (B8Ia). This is close to the emission lines noted in the next section.

4.1.11. 1616.7, 1625.3, 1626.1 and 1634.2 nm (emission lines)

The Wolf–Rayet star HD 94910 shows a rich set of emission lines at 1616.7, 1626.1, and 1634.2 nm. In a nearby wavelength range, the supergiant HD 148688 (B1Ia) displays an emission line at 1625.3 nm.

4.1.12. 1633.8 nm (absorption line)

Absorption line features are seen at 1633.8 nm in HD 90706 (B2.5Ia), HD 94910 (WN11-type star near emission line feature, creating P-Cygni profile), HD 105071 (B8Ia), HD 106068 (B8Ia/Iab), HD 112272 (B0.5Ia), HD 148379 (B9Iaep), HD 148688 (B1Iaeqp), HD 164865 (B9Ia), HD 168607 (B9Iaep, twin absorption line profiles), HD 168625 (B6Iap), HD 169454 (B1Ia), HD 170938 (B1Ia), HD 183143 (B6Ia), and HD 318014 (B8Ia). At a similar wavelength, several of the stars in the sample display prominent emission (Fig. 3 and Sect. 4.1.11). Neither Geballe et al. (2011) nor Cox et al. (2014) identified this feature. It is likely stellar, although we could not identify the line. Both N II (1634 nm) and Ne I were candidates but not visible in the B0.5Ia model (nor in a model for a cooler B8Ia star).

4.2. Likely interstellar or circumstellar features

A number of insterstellar or cirucumstellar features were detected. Their wavelengths and profile shapes are described below.

4.2.1. Wavelengths of detected features

Interstellar or circumstellar features were detected at the following wavelengths: 1318.1 nm, 1527.9 nm (partly contaminated by stellar absorption, as seen in the CMFGEN model of HD 152235 in Fig. 9), 1561.1 nm, 1564.4 nm (broad and weak, possibly stellar), 1565.1 nm (also partly contaminated by stellar absorption), 1567.0 nm, and possibly at 1634.2 nm, although it seems likely stellar (see Sect. 4.1.12). We had hoped to detect the broad DIB at 1622.7 nm previously observed towards the highly reddened Galactic Centre (Geballe et al. 2011). This DIB was also observed at 1622.7 nm in 4U 1907+09, the most heavily reddened object in the sample of nine stars observed by Cox et al. (2014). We did not detect the absorption in any of our higher resolution CRIRES spectra nor in the more highly-reddened X-shooter Cepheid data. Near 1623.3 nm, there is weak telluric absorption but no obvious DIB absorption.

[6] See http://www.gemini.edu/sciops/instruments/nearir-resources/astronomical-lines/h-lines for a list of Hydrogen lines.

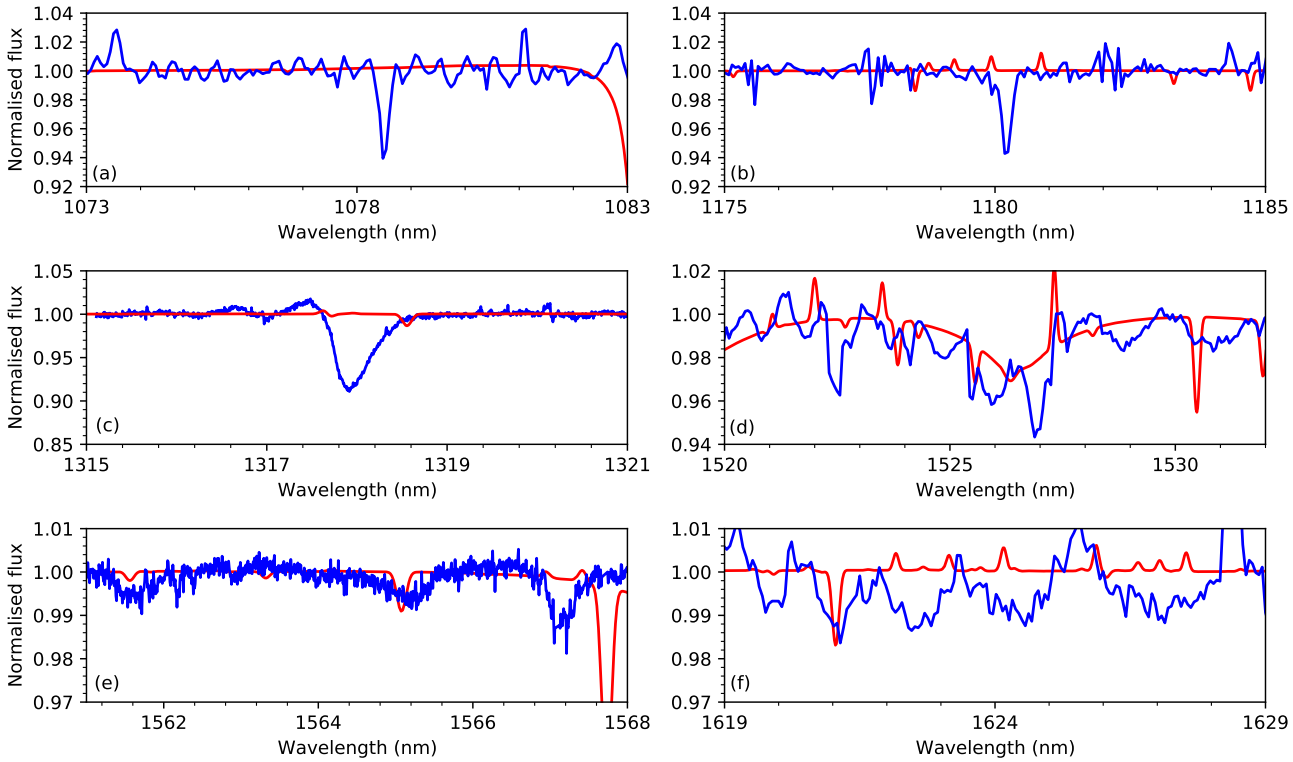

Fig. 9. Red lines: The same stellar model as shown in Fig. 8 plotted at the wavelength regions of the NIR DIBs shown in this paper plus the NIR DIBs around 1078 and 1180 nm. Blue lines: Observations of HD 152235 either from CRIRES (*panels c* and *e*) or X-shooter (*panels a, b, d, f*).

4.2.2. Shape of the DIB profiles and Gaussian fitting

Fits using one and two Gaussian components to the DIB at 1318.1 nm are shown in Fig. 10. For the DIB at 1318 nm, the majority of the lines are best fitted by twin Gaussians due to the extended red wing. A single-fit Gaussian leaves larger residuals.

An attempt was made to search for correlations between the ratio of the integrated flux in the twin Gaussian components and the difference in their peak wavelengths with 5780 and 5797 Å EWs, the $\lambda\lambda$5780/5797 DIB ratio, and reddening $E(B-V)$. No obvious correlations were found.

For the 1318 nm line, there was a range of FWHM fitted with a single component Gaussian. The values range from 0.36±0.01 nm (82±2.5 km s^{-1}) for HD 188293 to 0.53±0.01 nm (120±2.5 km s^{-1}) for HD 170938. These measurements compare with FWHM values of 0.45±0.12 nm from Cox et al. (2014) and 0.40±0.05 nm from Joblin et al. (1990) in lower-resolution spectra. For the current observations, the instrumental resolution of CRIRES was 6 km s^{-1}, so the DIB lines always appear to be resolved. Historically, the blue wing seen in the 4428 Å DIB was thought to provide evidence for a solid state carrier (Wickramasinghe 1968); however, this explanation has fallen out of favour for various reasons but principally for the lack of polarisation seen in DIBs. In contrast, the steep blue side (or red wing) seen in many DIBs is currently explained by the short wavelength spectral limit of the R-branch being reached in molecular carriers (e.g. Sarre 2014). In the current data, even the single-component dominated sightlines show the wing in the 1318 nm DIB. Finally, we note that no substructure is seen in the 1318 nm DIB at a spectral resolution of 50 000. In the optical DIB at 6614 Å, such structure has been used to infer the rotational constant, temperature, and possible excitation of the DIB via rotational contour modelling (Kerr et al. 1996; Cami et al. 2004; Marshall et al. 2015; MacIsaac et al. 2022). Higher spectral resolution CRIRES observations currently being analysed by Cox et al. ($R = 100\,000$) may be useful in finding such substructure.

Figure 11 shows the 1527 nm DIB towards four sightlines. At the S/N and resolution of the current observations, a Gaussian fit is sufficient to fit the profile, although in each case the trough of the profile is slightly deeper than the fit implies, and in the highest S/N spectra towards HD 148937, there are some residuals present.

The three DIBs at 1561, 1565, and 1567 nm have been extensively studied by Elyajouri et al. (2017) at a spectral resolution of 21 500. They measured mean FWHM values for the three DIBs of 0.44, 0.57 and 0.37 nm, in contrast to the current work of 0.53, 0.53 and 0.35 nm. As for the 1318 nm DIB, we find that the 1561 and 1567 nm DIBs are better fitted with twin rather than single Gaussian components.

Figure 12 shows a number of individual profiles for the 1318, 1527, 1561, 1565, and 1567 nm DIBs plus the co-added profile for spectra with the highest S/Ns. For the DIBs from 1561–1567 nm the spectrum appears to show an extra broad component at around 1564.4 Å, but the S/N is low. Continuum placement is hence difficult. We note that such a feature is not mentioned in the case of the higher S/N, lower spectral resolution data of (Elyajouri et al. 2017). However, a close look at their Fig. 4 shows that a similarly broad and shallow absorption is not precluded. The feature is not telluric in nature.

4.3. Comparison of NIR DIB strengths with other DIBs, atomic lines and reddening

Correlation studies between DIBs and other DIBs as well as between DIBs and atomic and molecular features serve two purposes. Firstly, the studies search for lines that correlate almost perfectly to provide evidence that the carrier producing the two

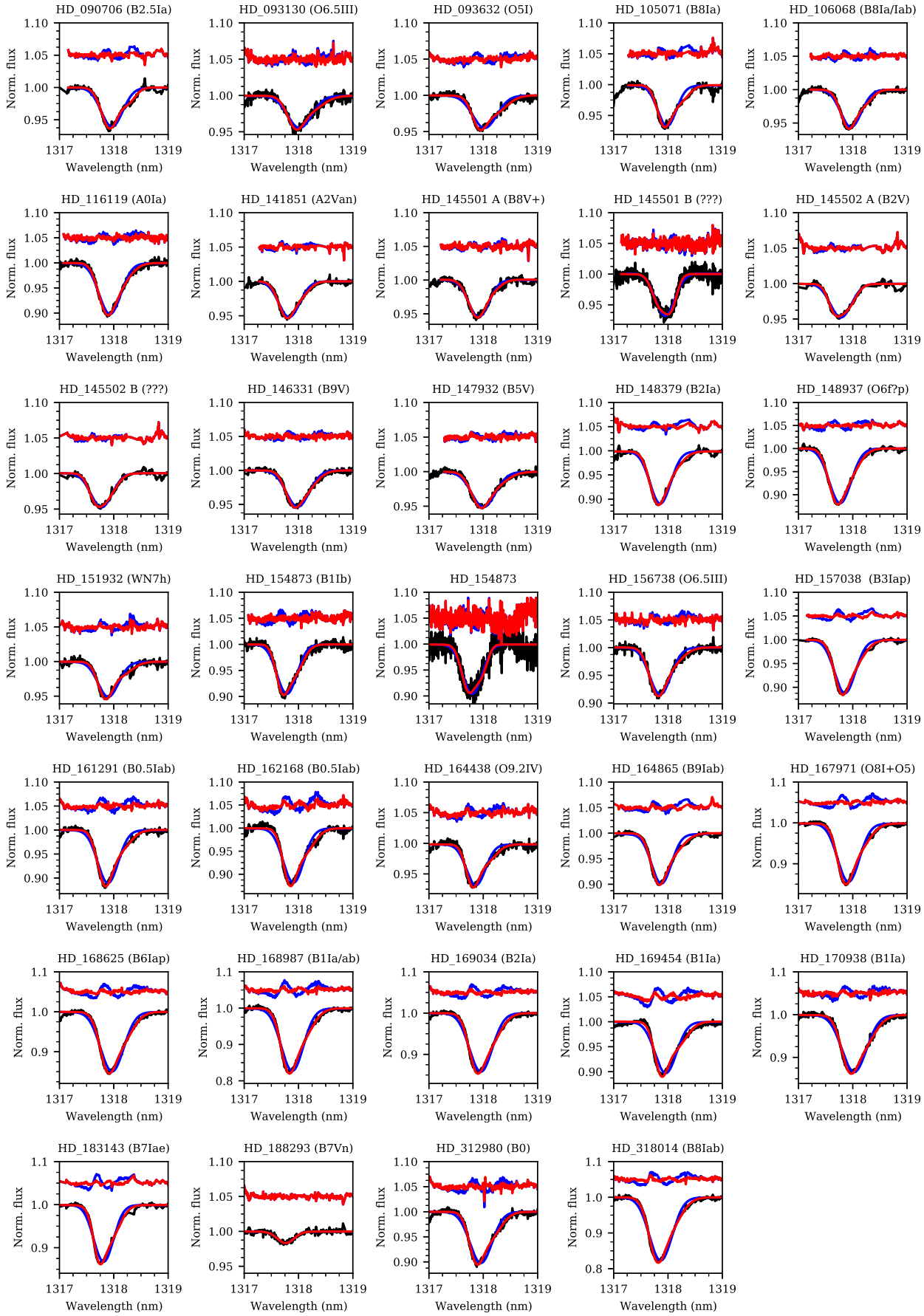

Fig. 10. CRIRES DIB observations around 1318 nm corrected for telluric absorption. Blue lines: One component Gaussian fit plus the residual (1.0+data-model). Red lines: The same for the two component Gaussian fits. The spectral resolution is ~0.026 nm.

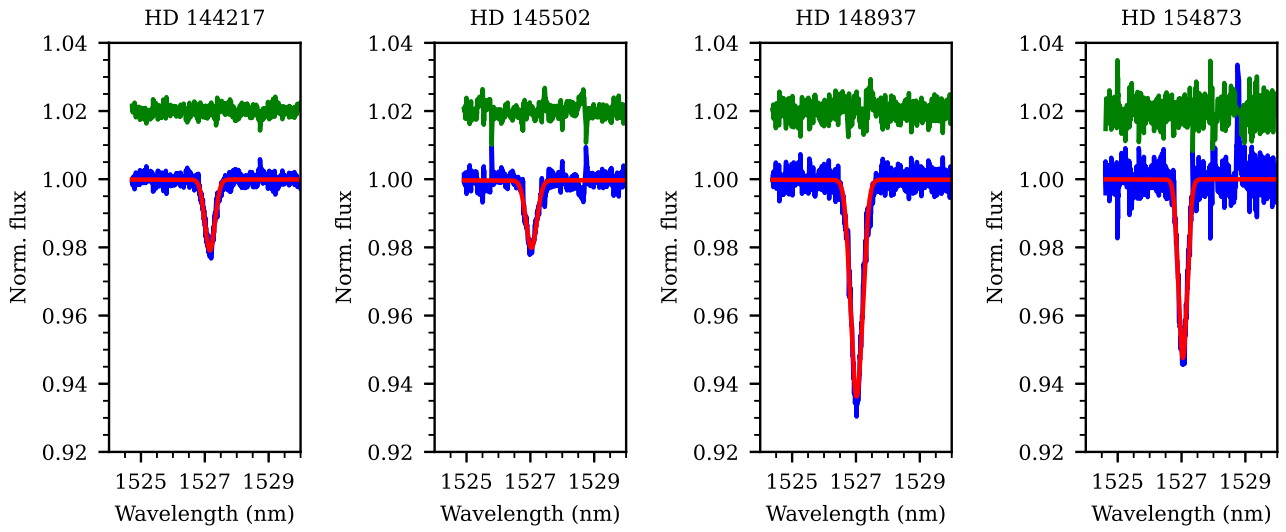

Fig. 11. CRIRES DIB observations around 1527 nm corrected for telluric absorption. Blue lines: Data. Red lines: One component Gaussian fit. Green lines: Residual (1.0+data-model) offset in the ordinate for clarity. The spectral resolution is ~0.030 nm. We note that HD 145502 is a binary.

lines is the same. Secondly they seek to determine the physical and chemical conditions in which certain DIBs exist, data which can be used in other work as probes of the environmental conditions. We note that just as in atomic lines a 1:1 correlation does not mean that the carriers are the same (as in the case of the near perfect correlation between Na I and K I EW), there is some evidence that the lack of a 1:1 correlation between different lines at different wavelength may not rule out a common carrier as in the case of the postulated $C60^+$ DIBs at 9577 and 9632 Å due to issues in telluric line fitting, possible overlapping bands and stellar contamination (Walker et al. 2017).

We searched for optical data related our NIR DIB sightlines in the advanced data products (ADPs) of the ESO archive[7]. In particular, we looked for data recorded with the Fiber-fed Extended Range Optical Spectrograph (FEROS; Kaufer et al. 1999), High Accuracy Radial velocity Planet Searcher (HARPS; Pepe et al. 2000) and UVES instruments. Some ADPs did not exist for FEROS observations so the data were re-reduced. Additionally we performed a search of the NARVAL/ESPADONS online archives but no relevant data were found. One star (HD 157778) was used from historical observations using the SOPHIE spectrometer at the Haut Provence Observatory (Perruchot et al. 2008). A total of 57 out of the 76 objects for which we have CRIRES spectra had optical data.

In each sightline we measured the EW of the strongest 50 DIBs in the catalogue of DIBs in the spectrum of HD 204827 (Hobbs et al. 2008, 2009) as well as the EWs derived from the current spectra. Many of the weaker DIBs were not detected in the archive spectra due to insufficient S/Ns. Telluric correction was performed by using scaled versions of synthetic spectra produced by SKYCALC. A CSV file containing the results of all of the EW measurements is available at the CDS. Apart from the DIBs, we also measured a number of atomic, ionised, and molecular lines. The full list is shown in Table 3, and Fig. D.1 displays the Na I (5895 Å) and K I (7698 Å) data for sightlines, where available, as well as the DIBs at 5780, 5797, 6196, 6203, 6269, 6283, 6379, and 6614 Å. Table E.1 (available at the CDS) shows the corresponding EW measurements.

In work on optical DIBs, Moutou et al. (1999) classified a Pearson correlation coefficient r of less than 0.7 as weak, 0.7 to 0.95 as good, and anything exceeding 0.95 as strong (also see Fan et al. 2017; Friedman et al. 2011, who suggest two quantities may have a physical relation if r exceeds 0.86–0.88). This is due to the fact that within the Galaxy, increasing distance along the line of sight will typically result in more absorbing material, so some correlation is natural. Most DIBs correlate (if only weakly), although to date the only near perfect 1:1 correlation between two DIBs is for those at 6196.0 and 6613.6Å (McCall et al. 2010).

Table G.1 shows the Pearson correlation coefficients for those DIBs that showed at least one instance of a correlation

[7] archive.eso.org

Table 3. Optical lines for which EW measurements were obtained.

Species, λ(Å)	Species, λ(Å)	Species, λ(Å)
NaI 3302.36	DIB 5236.18	DIB 6283.84
NaI 3302.97	DIB 5418.87	DIB 6376.08
TiII 3383.75	DIB 5450.60	DIB 6379.32
FeI 3719.93	DIB 5452.40	DIB 6397.01
FeI 3859.91	DIB 5494.10	DIB 6439.48
CNI 3873.99	DIB 5542.20	DIB 6445.28
CNI 3874.60	DIB 5545.40	DIB 6449.22
CNI 3875.76	DIB 5546.90	DIB 6521.30
CaII 3933.66	DIB 5705.08	DIB 6597.40
KI 4044.14	DIB 5711.60	DIB 6614.00
C3 4051.60	DIB 5763.20	DIB 6993.13
CaI 4226.72	DIB 5766.10	DIB 7224.03
CH+ 4232.54	DIB 5780.48	DIB 7562.25
CH 4300.31	DIB 5797.06	KI 7698.96
DIB 4501.79	DIB 5849.81	C2 7714.20
DIB 4726.83	NaI 5889.95	C2 7724.20
DIB 4762.61	NaI 5895.92	Rb 7800.30
DIB 4780.02	DIB 6089.85	C2 8757.68
DIB 4963.88	DIB 6113.18	C2 8761.19
DIB 4984.79	DIB 6195.98	C2 8763.74
DIB 4987.42	DIB 6203.05	C_{60}^+ 9632.10
DIB 5074.47	DIB 6204.49	
DIB 5176.04	DIB 6269.85	

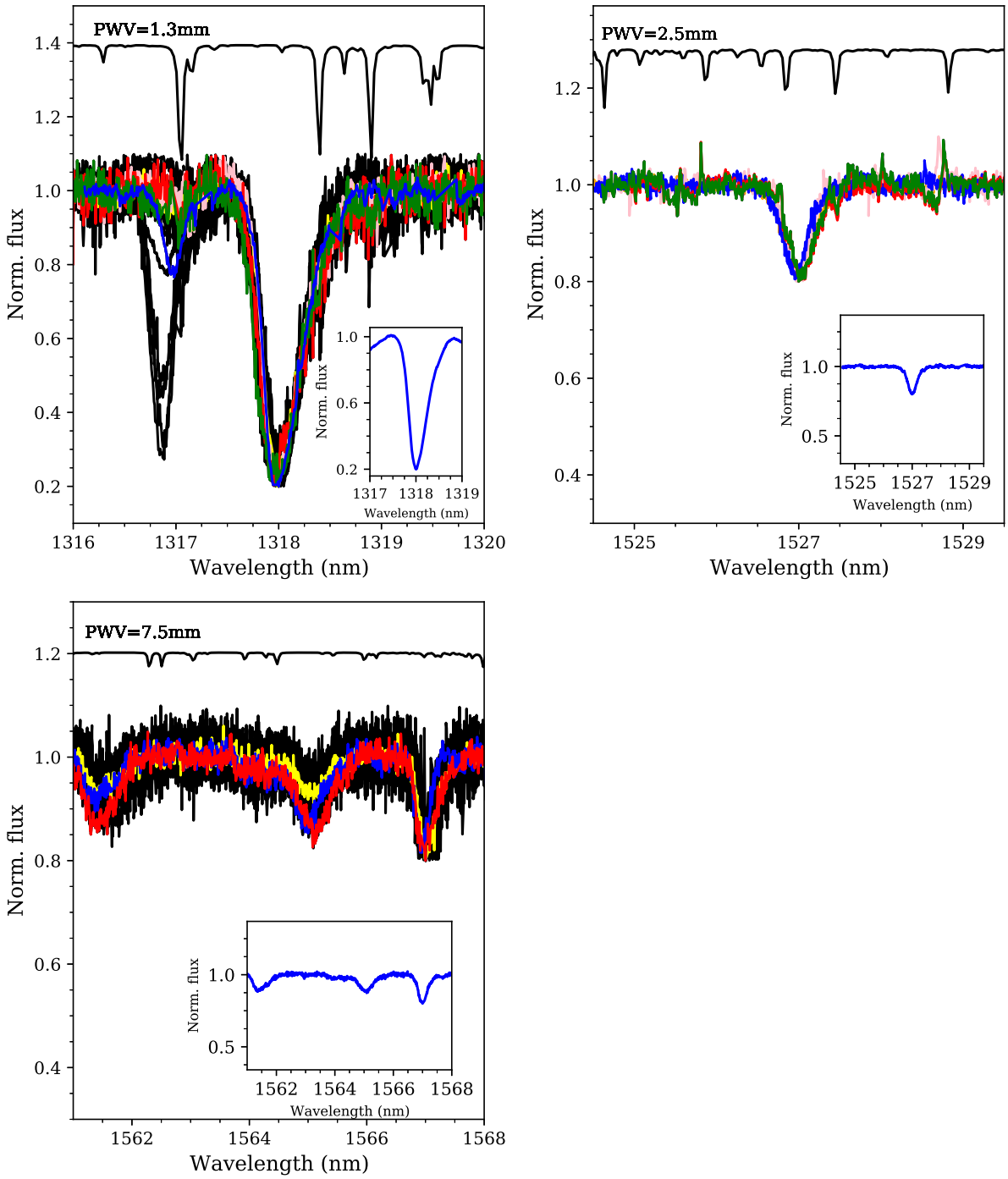

Fig. 12. CRIRES DIB spectra around 1318, 1527, and 1561–1568 nm. *Main panels*: Observations of all stars shifted in wavelength to 1318, 1527, and 1567 nm, respectively, and with absorption line trough normalised to 0.2. Top black line: Model of telluric absorption assuming PWV values of 1.3, 2.5, and 7.5 mm, respectively, with $R = 50\,000$. *Inset panels*: Averaged profiles for the DIBs with the strongest lines and for 1318 nm DIBs excluding sightlines showing inverted P-Cygni type profiles.

r exceeding 0.87 with another feature (the criteria of Friedman et al. 2011 to indicate that "two quantities are correlated at a significant level") for the whole sample, plus some optical transitions. Note that the correlation coefficients should be considered lower limits, as when sightlines with only one dominating component are considered (Single Cloud Dominated; SCDs), typically the correlation coefficient typically improves as shown in Fig. 13 and Table H.1. The disadvantage of such sightlines is that they are few in number in the current sample. Figure F.1 shows the correlations themselves where $r \geq 0.87$.

Following the suggestion of referee Ed Jenkins, the method of partial correlation coefficients was used to investigate the confidence level in the derived correlation coefficients. Partial correlation coefficients take into account the fact that even when there is correlation between two variables, it may be partly caused by a third variable, the so-called covariate or controlling variable (Vio et al. 2020). For the current work the reddening $E(B-V)$ was used as the covariate. The implementation of Vallat (2018) was used to derive the 95% confidence limits around the partial correlation coefficient. These are also shown

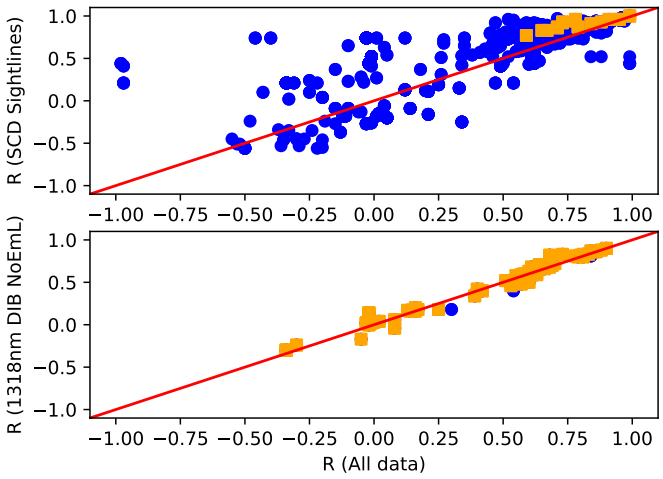

Fig. 13. *Top panel*: Comparison of correlation coefficients derived using the whole sample (abscissa) with those determined for the single component dominated sightlines (ordinate). There is a tendency for the correlation coefficients for the SCDs to be higher. The stars that we consider to be SCD from their K I profiles are HD numbers 36861, 36862, 88661, 89587, 93576, 137753, 144217, 145501, 145502, 147932, 148184, 156738, 164438, 164865, 167264, 169454, 188294 and 318014. Blue and orange symbols: Greater than or equal to ten or 15 data points, respectively. *Bottom panel*: Correlation coefficients comparing the 1318 nm sample excluding emission-line stars with the whole sample.

in Tables G.1 and H.1. If the 95% ranges are large then the chance of the two main variables not being physically correlated is increased. We note that results for correlations are shown only where there are 5 data points or more and with so few samples the significance is low. This is particularly the case for the sightlines that are single component dominated (SCD) which have fewer data available.

4.3.1. Correlations between NIR DIB strength and reddening

Figure 14 shows the correlation between DIB EWs and reddening for the lines studied in this paper. In the optical wavelength range at low values of $E(B-V)$, the correlation between EW and reddening is reasonable (e.g. Lan et al. 2015), but it reaches saturation at higher values, partly due to the skin effect by which DIB carriers seem to disappear in the centre of dense clouds (Snow & Cohen 1974). One DIB relatively well correlated with reddening is the *Gaia* DIB at 8620.4 Å (Munari 2000), although even it shows some intrinsic scatter.

There are reasonable correlations for the CRIRES-observed targets with reddening for all of the NIR DIBs studied. Correlations between the 1318, 1527, 1561, 1565, and 1567 nm DIBs and $E(B-V)$ are in the range 0.76–0.92 for the full sample and 0.74–0.96 for the SCD sample. These ranges are similar to the values observed by Cox et al. (2014) for the 1318 and 1527 nm DIBs. We note that in the current dataset the scatter in the measurements above $E(B-V)$ of around two to three magnitudes becomes larger. Of course, this could partly be due to stellar contamination of the lines in the high-reddening X-shooter Cepheid sample. Stellar contamination in the 1318 nm and 1527 nm lines for the Cepheid variables was estimated from X-shooter spectra of six Cepheid variable stars taken from the X-shooter spectral library of Chen et al. (2014). Five of these are in the Galactic disc with reddening $E(B-V)$ values between 0.04 and 0.89, and one star is towards the low-metallicity cluster ω Cen with $E(B-V) = 0.12$.

Figure 15 shows the Chen et al. (2014) spectra (at a range of reddenings) and two targets from Minniti et al. (2020). The EW values of the stellar lines around 1318 nm and 1527 nm DIBs for the Galactic plane Cepheid with $E(B-V)$ of 0.12 are 368 and 651 mÅ, respectively. Hence, at $E(B-V) \approx 3$ magnitudes, the stellar contribution in the Cepheid data could be up to 20% in both 1318 nm and 1527 nm DIBs. We note that the Cepheid towards the low-metallicity cluster Omega Cen (NGC 5139 LEID 32029) with $E(B-V) = 0.12$ has a 1318 nm EW of 135 mÅ, although the region around 1527 nm is very crowded with lines with the total EW from 1524 to 1530 nm of ∼1.5 Å.

These results are comparable to those of Cox et al. (2014), who found $r = 0.91$ for the 1318.1 nm DIB (with fewer data points). No correlation coefficients are shown for $E(B-V)$ in the paper of Elyajouri et al. (2017) for this DIB.

4.3.2. Correlation between strength of NIR DIBs

Figure 16 shows correlations between the line strength of DIBs studied in this paper. The correlations between the 1318, 1527, 1561, 1565, and 1567 nm DIBs range from 0.84 to 0.92 for the entire sample and from 0.18 (few stars) to 0.98 for the SCD sample. We highlight that these are lower limits due to the S/N limitations and difficulty in the baseline fitting, especially for the 1561 nm DIB. Cox et al. (2014) determined $r = 0.93$ when comparing the 1318 and 1527 nm DIBs, similar to our value of 0.90.

4.3.3. Correlation between 1318 nm DIB strength, H I, H_2, and f(H_2)

Figure 17 shows normalised X-shooter spectra, corrected for telluric contamination using MOLECFIT for early-type stars for which N(H I), $N(H_2)$, and f(H_2) data were available from the literature (Fan et al. 2017 and references therein). To these data we added our CRIRES 1318.1 nm observations, using either literature values for H I, H_2 and f(H_2), or, in the case where these did not exist, estimates of H_2 from the CH(4300 Å) line derived from $\log(N(H_2)) = 0.8875 \times \log(N(CH)) + 8.88$ using data from Welty et al. (2006). The DIB at 5780 Å was used to estimate N(H I) via $\log(N(\text{H I}) = 0.82 \times \log(\text{EW}(5780\ \text{Å DIB})) + 19.34$ (Friedman et al. 2011). The results are shown in Table 4.

Figure 18 shows the EW of the 1318 nm line and the EW divided by the $E(B-V)$ plotted against N(H I), $N(H_2)$, and f(H_2). The aim of these plots was to search for the lambda-shaped trend which shows that atomic and diffuse molecular clouds show dramatically different balances in the creation and destruction of DIBs (Fan et al. 2017). There are hints of such a trend when plotting the EW of the 1318 nm DIB against molecular fraction. However, when this is normalised by the reddening, the shape disappears and what is left is a noisy but slowly decreasing EW(1318 nm)/$E(B-V)$ trend with increasing molecular fraction. In the straight correlation we found better correlation between the 1318 nm DIB and H I than with H_2, though still with a lot of scatter.

4.3.4. Correlation between optical DIB strengths

There is extensive literature concerning correlations between the strengths of optical DIBs (e.g. Cami et al. 1997; Moutou et al. 1999; McCall et al. 2010; Kos et al. 2013 amongst many others).

The accuracy of our analysis was evaluated by comparing our EW measurements with previous results. Figure 19 shows the ratio of the EWs measured for several sightlines of our sample

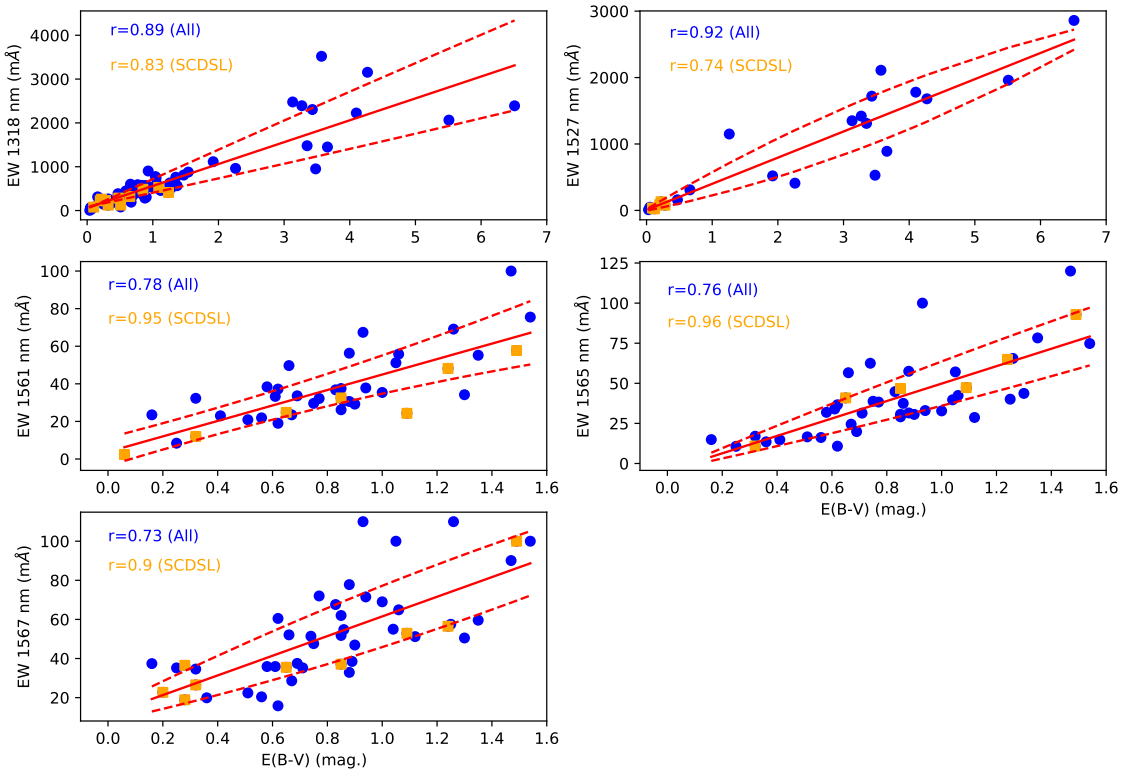

Fig. 14. EW in mÅ vs. Reddening $E(B-V)$ (mag.) for the NIR DIBs in the current sample. Blue points show all of the data, and orange points show only single component dominated sightlines. For the 1318 and 1527 nm DIBs for reddening exceeding 3.13 mag. the data are from the X-shooter Cepheid sample that suffer from stellar contamination of around 500 mÅ for un-reddened sightlines. The solid red line is the best fit y=mx+c and the dashed red curves show the upper and lower one sigma error bounds.

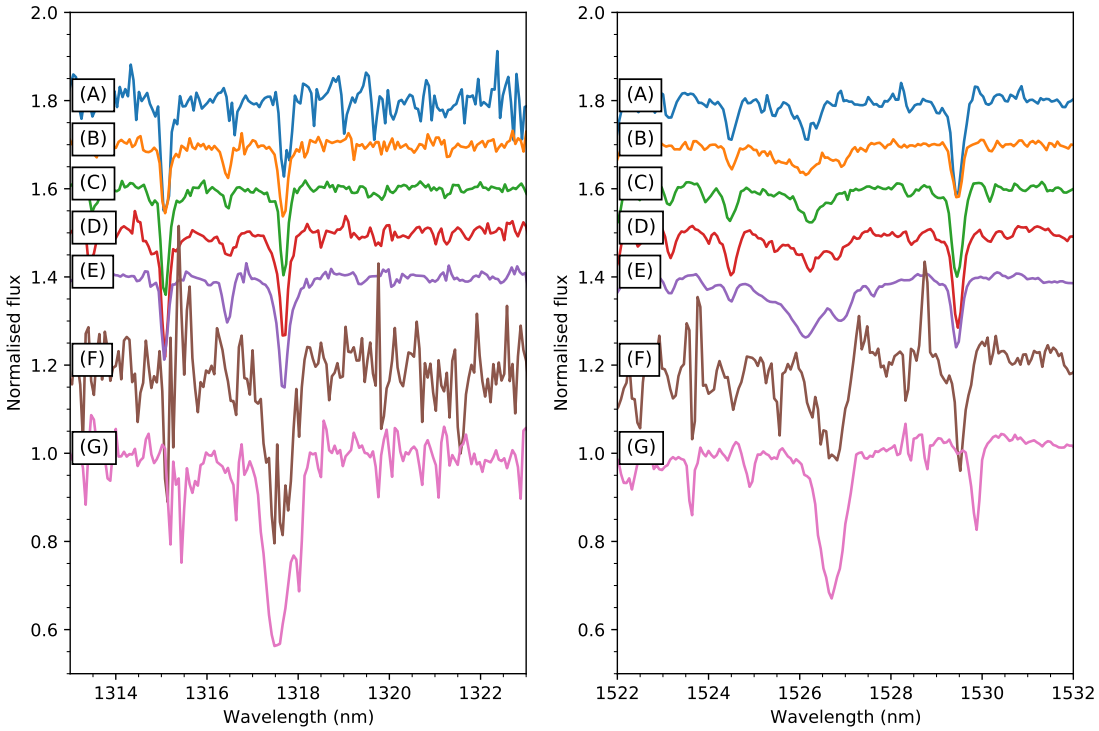

Fig. 15. X-shooter spectra of Cepheid variables around 1318 nm (*left panels*) and 1527 nm (*right panels*) taken from Chen et al. (2014) and Minniti et al. (2020). Reddening increases downwards. (A) HD 052973, $E(B-V)$ = 0.04, EW(1318 nm)=368±30 mÅ, and EW(1527 nm)=450±50 mÅ. (B) HD 101602, $E(B-V)$ = 0.25, EW(1318 nm)=419±30, and EW(1527 nm)=840±50 mÅ. (C) HD 178287, $E(B-V)$ = 0.40, EW(1318 nm)=470±20 mÅ, and EW(1527 nm)=570±60 mÅ. (D) HD 179315, $E(B-V)$ = 0.59, EW(1318 nm)=691±50 mÅ, and EW(1527 nm)=890±70 mÅ. (E) HD 139717, $E(B-V)$ = 0.89, EW(1318 nm)=913±30 mÅ, and EW(1527 nm)=2300±600 mÅ. (F) B19, $E(B-V)$ = 3.27, EW(1318 nm)=2300±250 mÅ, and EW(1527 nm)=1400±300 mÅ. (G) D20, $E(B-V)$ = 3.57, EW(1318 nm)=2120±110 mÅ, and EW(1527 nm)=3300±100 mÅ.

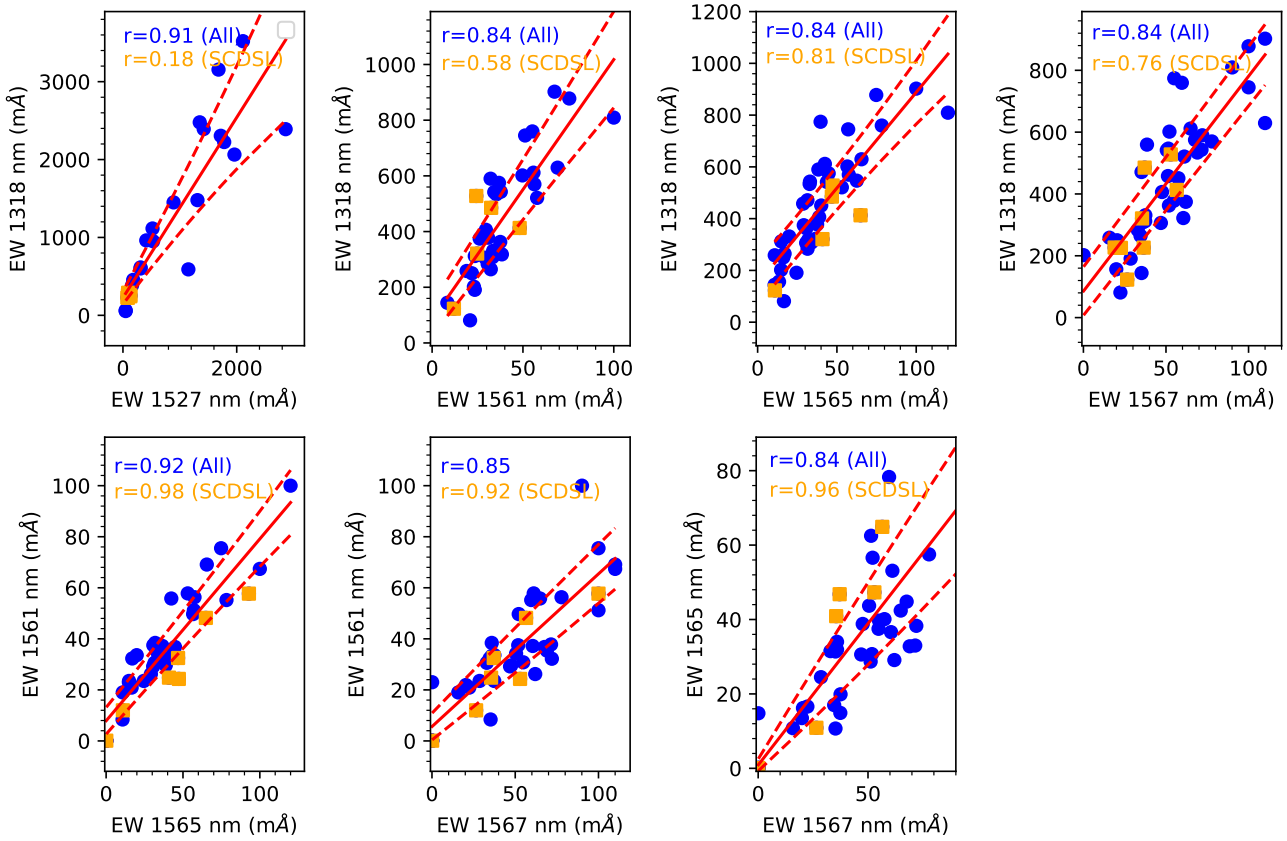

Fig. 16. Correlations in EW in mÅ for the NIR DIBS in the current sample. Both the whole sample (blue points) and the single component dominated subsample (orange points) are shown. The dashed red curves show the upper and lower one sigma error bounds.

with values taken from the literature. The current measurements have a median value some 4.6% larger than the literature values ($N = 86$) with 76/86 of the measurements lying within 20% of each other. However, the correlation coefficient of the two lines of the Na I UV doublet and for Na I vs K I are (as expected) close to 1.00, respectively, indicating no gross error in our analysis.

We next considered optical to optical correlations with values of $r \geq 0.95$ and more than or equal to six data points. These correlations included the 6614 Å DIB correlated with 5780 Å, 5797 Å, 6269 Å, 6376 Å, 6439 Å, and 6693 Å. Of these, 5780, 6196, 6203, 6269, and 6284 Å were historically classified as a DIB family (Krelowski & Walker 1987, although see Cami et al. 1997). Additionally, the 6439 Å DIB correlates extremely well with 6376 Å and the NIR DIB at 1527 nm, but for the latter with only six data points.

Finally, a number of DIBs showed negative correlations when compared with other optical or NIR DIBs. For correlations with greater than or equal to ten data points these include the 4501.8 DIB compared with the NIR DIBs described in this paper, the comparisons of the 4762.6 nm, 5074.5 nm, and 6993.1 nm DIBs with more than ten other DIBs, and finally the comparison of the 4780.0 DIB compared with the 5418.9 DIB.

4.3.5. Correlation between NIR DIB and optical DIB strengths

Of particular interest is the correlation between the NIR DIBs and "C_{60}^+"-DIBs whose wavelengths were measured in the lab by Campbell et al. (2015, 2016) of 9348.4, 9365.2, 9427.8, 9577.0, and 9632.1 Å with an uncertainty of 0.2 Å. These lines are the only DIBs thus far for which a carrier has been identified. The two reddest lines are the strongest lines. In this work we only measured the 9632.2 Å DIB as it is less affected by telluric contamination. That said, there is a nearby Mg II stellar line that causes contamination of the DIB (Galazutdinov et al. 2017b; Lallement et al. 2018). The correlation coefficient between the "C_{60}^+" 9632 Å DIB and 1318 nm DIB is only $r = 0.50$ (N=10), not correcting for possible stellar contamination.

The 1318, 1561, and 1567 nm DIBs show good correlation (r = 0.88, 0.86, 0.85) when compared with the 5780 Å DIB (Cox et al. (2014) determine $r = 0.98$ for the 1318 nm DIB but with fewer data points) and similar values when compared with the 6283 Å DIB ($r = 0.91$, 0.85, 0.89), 6203 Å DIB ($r = 0.86$, 0,85, 0.88), 5705 Å DIB ($r = 0.84$, 0.83, 0.80), 6196 Å DIB ($r = 0.81$, 0.88, 0.80), 6269 Å DIB ($r = 0.79$, 0.85, 0.81) and 6993 Å DIB ($r = 0.78$, 0.85, 0.83). For the 5797 Å DIB the correlation is slightly lower with the NIR DIBs, being $r = 0.71$, 0.77 and 0.73 for the 1318, 1561 and 1567 nm DIBs, respectively with typically around 30 data points in the samples. These results indicate that the NIR DIBs are more sigma type than eta type and supports the conclusion of Cox et al. (2014) from the absence or weakness of NIR DIBs in the HD 147889 sightline probing a translucent cloud. The correlation plots are shown in Fig. 20.

4.3.6. Correlations between DIB ratios and $\lambda\lambda$5797/5780, Ca I/Ca II, CH/CH+, and Na I/Ca II

The most commonly studied optical DIBs are at 5797 Å and 5780 Å. The former, like the blue 4429 Å DIB, is known to trace the neutral ISM, while the latter probes more ionised regions (e.g. Farhang et al. 2015; Bailey et al. 2016). The 5797 Å/5780 Å

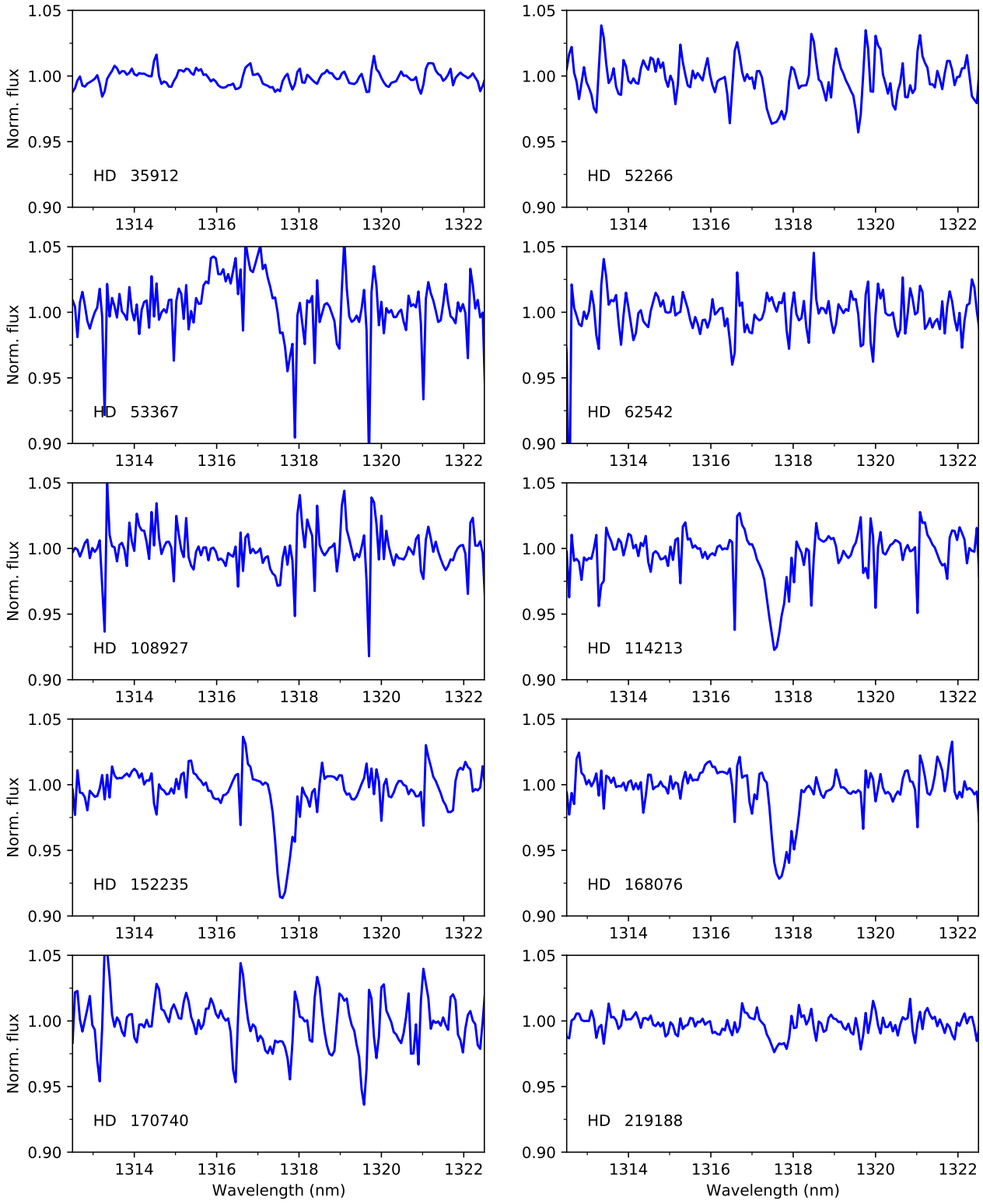

Fig. 17. X-shooter data around 1318 nm corrected for telluric contamination using MOLECFIT for which $f(H_2)$ is available in the literature.

DIB EW ratio is therefore used to probe the UV field. Values of less than 0.35 probe regions with higher UV. Higher values of the ratio indicate UV-shielded regions (e.g. Cami et al. 1997; Vos et al. 2011 and references therein).

Hence, we also searched for correlations between ratios of the 1318 nm DIB to a number of the stronger optical DIBs (Hamano et al. 2015, 2016) and reddening. The aim was to determine the relative dependence of the 1318 nm band on the UV radiation field. This was done by plotting in Fig. 21 the ratio of EW of the 1318 nm DIB divided by the 4984, 5780, 5797, 6196, or 6283 Å EW against the $\lambda\lambda$5797/5780 ratio. As noted above, the latter ratio is an indicator of UV radiation field with the

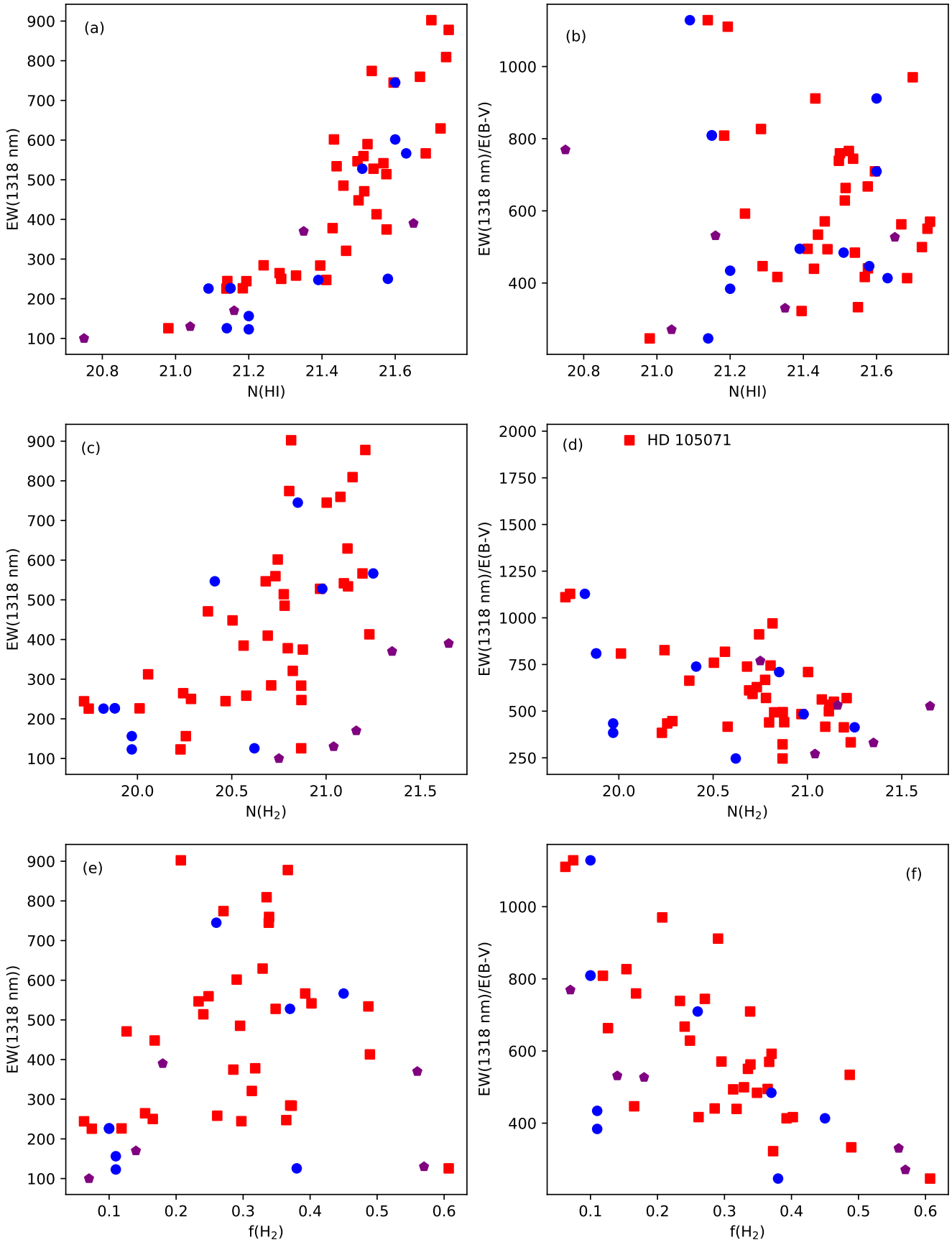

Fig. 18. EW(1318 nm) (*plots a,c,e*) or EW(1318 nm)/$E(B-V)$ (*plots b,d,f*) plotted against N(H I), $N(H_2)$ and f(H_2). Stars with emission lines near 1318 nm were excluded. Blue circles: CRIRES data with N(H I), $N(H_2)$, f(H_2) from the literature. Red squares: CRIRES data with H I calculated from the 5780 DIB and N(H_2) from CH. Purple pentagons: X-shooter with N(H I), $N(H_2)$, f(H_2) from the literature. Outlier HD 105071 is labelled.

Table 4. Values of the EWs of the 1318 nm DIB, CH(4300 Å), and the 5780 Å DIB for CRIRES (C) and X-shooter (X) sightlines for which $f(H_2)$ is available or can be estimated.

HD	Inst.	EW(1318) (mÅ)	EW(CH4300) (mÅ)	EW(5780) (mÅ)	N(H_2) (cm^{-2})	N(H_2)c (cm^{-2})	N(HI) (cm^{-2})	N(HI)c (cm^{-2})	$f(H_2)$ (cm^{-2})	$f(H_2)$c (cm^{-2})
35912	X	...	...	...	20.35	...	20.35	...	...	0.12
36408	C	Det. (HWV)	...	...	...	...	...	...	...	...
36861	C	<	1.76	48.29	19.65	19.11	20.77	20.72	0.14	0.04
36862	C	...	2.44	34.27	19.80	...	...	20.60	0.24	...
36959	C	< (HWV)	...	...	...	...	20.40	...	...	...
52266	X	170.00	...	...	21.16	...	21.16	...	...	0.14
53367	X	...	...	...	21.32	...	21.32	...	...	0.51
57060	X	...	...	...	20.78	...	20.78	...	...	...
62542	X	...	...	...	20.90	...	20.90	...	...	0.62
88661	C	< (EmL)	...	13.21	...	...	...	20.26	...	...
90706	C	308.10	...	...	...	...	...	...	...	...
92740	C	156.30	6.38	...	20.26	19.97	21.20	...	...	0.11
93130	C	250.20	6.76	237.90	20.28	...	21.58	21.29	0.17	...
93632	C	258.40	12.55	266.51	20.58	...	...	21.33	0.26	...
94910	C	448.10	10.76	430.55	20.50	...	...	21.50	0.17	...
97707	C	190.80	...	...	...	...	...	...	...	...
105056	C	202.00	3.36	...	19.95	...	21.15	...	...	...
105071	C	312.20	4.18	...	20.06	...	...	...	...	...
106068	C	264.60	6.19	234.96	20.24	...	...	21.28	0.15	...
108927	X	...	...	...	20.86	...	20.86	...	...	0.46
111774	X	...	1.00	...	19.38	...	...	...	1.00	...
112272	C	362.70	39.21	441.12	21.12	...	...	21.51	0.45	...
113904	X	144.20	1.66	126.35	19.62	19.84	21.08	21.06	0.07	0.10
114213	X	370.00	...	...	21.35	...	21.35	...	...	0.56
115088	C	<	...	13.75	...	...	...	20.27	...	...
115363	C	331.10	27.87	...	20.95	...	...	...	...	...
115842	C	81.20	21.83	234.59	20.84	...	21.15	21.28	0.42	...
116119	C	471.00	8.17	449.75	20.37	...	...	21.52	0.13	...
125007	C	...	...	18.28	...	...	...	20.37	...	...
125241	C	514.10	19.10	532.96	20.78	...	...	21.58	0.24	...
142468	C	589.80	...	461.15	...	...	...	21.52	...	...
144217	C	225.70	2.15	156.24	19.74	19.82	21.09	21.14	0.07	0.10
144218	C	244.60	9.95	157.34	20.47	...	...	21.14	0.30	...
145501	C	244.30	2.04	182.11	19.72	...	...	21.19	0.06	...
145502	C	226.40	3.80	177.17	20.01	19.88	21.15	21.18	0.12	0.10
147889	X	...	...	...	21.80	...	21.80	...	...	0.48
147932	C	284.30	16.59	207.86	20.71	...	...	21.24	0.37	...
148184	X	125.70	23.21	100.11	20.87	20.62	21.14	20.98	0.61	0.38
148379	C	546.70	15.60	427.06	20.68	20.41	...	21.50	0.23	...
148688	C	318.10	13.20	...	20.60	...	...	...	...	...
148937	X	601.60	17.85	356.50	20.74	...	21.60	21.43	0.29	...
151932	C	247.40	23.27	336.08	20.87	...	21.39	21.41	0.36	...
152235	X	406.30	29.13	418.07	20.98	21.00	21.42	21.49	0.38	0.43
152386	C	378.00	19.97	352.84	20.80	...	...	21.43	0.32	...
154368	X	<	...	...	21.00	...	21.00	...	...	0.74
154811	C	409.70	15.96	...	20.69	...	...	...	...	...
154873	C	384.60	12.18	...	20.56	...	...	...	...	...

Notes. A '<' symbol corresponds to no detection. The log of the column densities of H_2 and HI taken from the literature or derived from CH (N(H_2)c) and the 5780 Å DIB (N(HI)c) are also shown, along with the fractional H_2 content or its value derived from CH and the 5780 Å DIB, (fH_2c). HWV refers to sightlines that had high water vapour affecting the 1318 nm DIB measurements and EmL observations affected by emission lines in the DIB.

5780 Å as the DIB prefers regions where the UV radiation field is strong (the so-called σ DIBs) and the 5797 Å DIB prefers regions where the field is weaker (the ζ DIB). Although our results are somewhat scattered, they are in line with previous work in that the 1318 nm DIB appears to favour regions of higher UV field and perhaps are cation molecules (Hamano et al. 2016).

Finally, in Fig. 21 we plot the 1318 nm/optical DIB ratio against a number of line ratios. The first line ratio was Ca I/Ca II which has been used as an indicator of electron

Table 4. continued.

HD	Inst.	EW(1318) (mÅ)	EW(CH4300) (mÅ)	EW(5780) (mÅ)	N(H_2) (cm^{-2})	N(H_2)c (cm^{-2})	N(HI) (cm^{-2})	N(HI)c (cm^{-2})	$f(H_2)$ (cm^{-2})	$f(H_2)$c (cm^{-2})
156134	X	283.70	23.21	320.89	20.87	...	...	21.40	0.37	...
156201	C	306.20	...	318.77	...	...	...	21.39	...	...
156212	X	322.10	30.49	375.79	21.00	...	...	21.45	0.41	...
156738	C	413.00	49.81	494.35	21.23	...	...	21.55	0.49	...
157038	C	559.60	17.40	447.04	20.73	...	...	21.51	0.25	...
157778	C	<	...	34.26	...	...	...	20.60	...	...
164438	C	320.90	21.13	391.36	20.82	...	...	21.47	0.31	...
164865	C	485.20	19.28	383.28	20.78	...	...	21.46	0.30	...
165319	C	374.60	23.65	533.85	20.88	...	...	21.58	0.29	...
166734	X	566.50	46.12	720.74	21.19	21.25	21.63	21.68	0.39	0.45
167264	X	122.90	6.01	...	20.23	19.97	21.20	...	...	0.11
167971	C	745.00	30.89	563.33	21.00	20.85	21.60	21.60	0.34	0.26
168076	X	390.00	...	...	21.65	...	21.65	...	...	0.18
168607	C	877.80	47.60	859.65	21.21	...	...	21.75	0.37	...
168625	C	809.30	41.27	842.82	21.14	...	...	21.74	0.34	...
168987	C	902.30	20.74	752.62	20.81	...	...	21.70	0.21	...
169034	X	759.60	36.03	689.54	21.08	...	...	21.67	0.34	...
169454	X	527.80	28.68	482.95	20.97	20.98	21.51	21.54	0.35	0.37
170740	X	130.00	...	...	21.04	...	21.04	...	...	0.57
170938	C	774.30	20.30	476.37	20.80	...	...	21.54	0.27	...
171722	C	<	0.47	20.88	19.02	...	...	20.42	0.07	...
183143	C	629.40	38.99	807.49	21.11	...	...	21.72	0.33	...
214080	X	...	...	...	20.58	...	20.58	...	...	0.01
219188	X	100.00	...	...	20.75	...	20.75	...	...	0.07
318014	C	813.00	42.88	675.39	21.16	...	...	21.66	0.39	...
319699	C	534.00	39.22	363.85	21.12	...	...	21.44	0.49	...
319702	C	541.70	37.45	521.04	21.09	...	...	21.57	0.40	...

Table 5. Objects with observed companions within one arcminute.

HD number	Alternative names	l, b (deg.)	Companion	Separation (arcs, au)	NIRDIB setting(s) observed	Reference and comments
36408	HR 1847	188.4942 –08.8854	HD 36408B	9.5, 2100	a,c	WM96. No NIRDIB detection.
36959	YSO	209.5670 –19.7206	HD 36960	36.0, 21000	a,b,c	WM96. No NIRDIB detection.
36861 J	lam Ori A	195.0519 –11.9951	HD 36862	3.5, 2500	a,b	WM96. No NIRDIB detection.
139891	HR 5834	058.6978 +53.4129	HD 139892	6.3, –	a,b	LWV03. No NIRDIB detection.
144217	HR 5984, bet Sco	353.1929 +23.5996	HD 144218	13.6, 2900	a,b,c	WM96. NIRDIB detection.
145501	HR 6026	354.6140 +22.7107	HD 145501 B	2.5, –	a,b,c	NIRDIB detection.
145501	HR 6026	354.6140 +22.7107	HD 145502 A	41.0, 7200	a,b,c	LM99. NIRDIB detection.
145502	HR 6027, nu Sco A	354.6087 +22.7002	HD 145502 B	1.4, –	a,b,c	LM99. NIRDIB detection.
154873 A	HIP 84010	341.3454 –04.1096	HD 154873 B	8.0, –	a,b	No optical data. NIRDIB det.
157779	HR 6485, rho Her A	061.4422 +32.7103	HD 157778	4.3, 480	a,b,c	WM96. No NIRDIB detection.
160065	LS 4314	355.3166 –01.3562	–	18.6, –	a	Companion has no SIMBAD Reference. NIRDIB detection.
168607		014.9679 –00.9397	HD 168625	67.4, 108289		NIRDIB detection.
188293	57 Aql A	032.6612 –17.7609	HD 188294	35.6, 5700	a,b,c	WM96. NIRDIB detection.
318014	LS 4255	355.0738 –00.7062	LS 4256	20.5, –	a	NIRDIB detection.

Notes. CRIRES reference wavelengths are as follows: (a) 1318.1 nm, (b) 1527.9 nm, (c) 1568.8 nm.
References. WM96 (Watson & Meyer 1996), LM99 (Lauroesch & Meyer 1999), LWV03 (Lallement et al. 2003).

density (e.g. McEvoy et al. 2015). The use of this line ratio has many issues, in particular the presence of a perhaps dominating Ca III (Sembach et al. 2000) and the assumption that Ca I and Ca II trace the same parts of the ISM (Crawford 2002; see also Welty et al. 2003). Second, we show correlations with the CH/CH+ ratio which is an indicator of turbulent dissipation and warm H_2 (Valdivia et al. 2017). The last line ratio is Na I/Ca II which provides an indication of shocks and dust content via the Routly-Spitzer effect (Routly & Spitzer 1952; Vallerga et al. 1993). We note that saturation can be an issue in

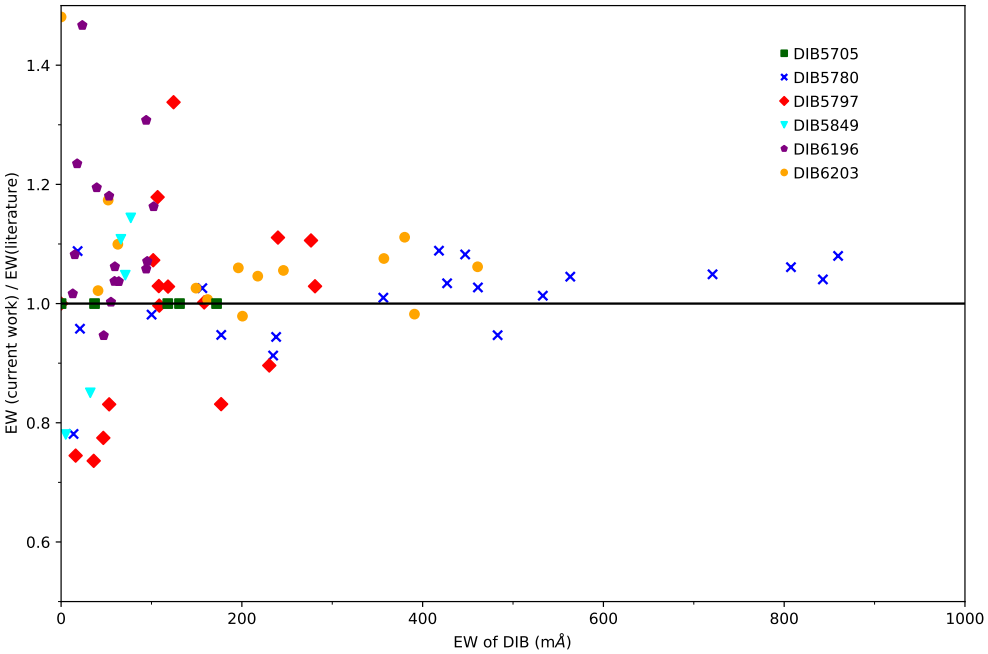

Fig. 19. Ratio of the EW from the current paper divided by values taken from the literature. Values are shown for several DIBs. The unity line is shown.

these lines and that there are no convincing trends in any of the relationships.

4.4. Search for correlations in normalised DIB spectra

Cami et al. (1997) and more recently Fan et al. (2022) searched for correlations in DIB strengths by using the normalised DIB strength (EW/$E(B-V)$). One of the goals of Fan et al. (2022) was to search for anti-correlated DIBs and compare the changes in the correlation coefficients across DIB families. In the current dataset we find that no NIR DIBs show anti-correlations less than ~–0.7 with more than ten data points. The best correlations are found between the 1318 and 1527 nm reddening-normalised DIB EWs where r exceeds 0.9.

4.5. Search for small-scale structure and time variability in NIR DIBs

4.5.1. Search for small-scale structure

In neutral species, such as Na I and K I, small-scale (pc-) structure is ubiquitous in the interstellar medium (Meyer & Lauroesch 1999), with variations also seen (but smaller) in singly ionised elements, such as Ca II and Ti II (Smoker et al. 2011). Variations have also been detected in five optical DIBs between 5780 and 6614 Å by Cordiner et al. (2013) towards the stellar binary ρ Oph A and B, separated by 344 au and with variations in the DIB strengths of 5–9%. Sometimes the variations seen are greater than in the corresponding difference between atomic and diatomic lines, such as in Na I. Similarly, van Loon et al. (2013) observed DIBs in both Galactic and LMC gas, finding that small-scale structure increased from Na I to the 5780 Å DIB to the DIB at 5797 Å. Furthermore, in Milky Way gas, the 5797 Å DIB displayed a variation of an order ten times greater than that seen in Na I on scales of 0.04 pc. Wendt et al. (2017) discuss small-scale variations over the face of NGC 6397 (a globular cluster), which are of the order of a few thousand au.

Eleven of our CRIRES sightlines are in double, triple, or quadruple systems. Table 5 shows the stars that have companions within 1′ that were observed to search for small-scale structure in DIBs. The subsample was derived in part from observations by Watson & Meyer (1996) and Lauroesch & Meyer (1999), who studied many of the sightlines in either Na I or K I, and partly by chance when another object was visible on the slit viewer image. Of our sample of eleven fields, five show no DIB at 1318.1 nm, and four show no difference in profile between the two closely separated objects. The spectra are shown in Figs. 23 to 25.

In particular, three stars have bright companions within 20 arcsec: HD 144217 and HD 144218, which are separated by 13.6 arcsec and have similar values of parallax (8.07±0.78 and 7.75±0.40 mas); the HD 154873 A and B pair with separation of 8.2 arcsec and similar parallaxes of 0.97±0.06 and 1.00±0.08 mas respectively and HD 318014 which is a line-of-sight companion to TYC 7380-1056-1 at 20.8 arcsec. The parallaxes of these stars are somewhat different, (i.e. 0.42±0.05 and 0.18±0.06 mas, respectively). None of the stars above show convincing differences in the 1318 nm EW compared with their line-of-sight companions. In the case of the HD 144217 and HD 144218 pair some optical data exist in the ESO archives (see Fig. 22). Similarly, there are no convincing small-scale variations observed in the optical lines.

This leaves three fields in which possible variations in the 1318 nm line are seen. The first is the HD 145501 and HD 145502 field. This field comprises the two main objects, each of which has a companion. The two main objects were observed in K I by Lauroesch & Meyer (1999) as many of the lines were saturated in Na I. They found a density contrast of between 1.1±0.1 and 1.8±0.8 in three different observed components, with the HD 145501 sightline having stronger K I lines. This contrast in the K I components is not seen in the data we downloaded from the ESO archive, shown in Fig. 23, likely due to the lower spectral resolving power in the archive data.

In the 1318 nm spectra, the main component, HD 145501 A ($\pi = 7.09 \pm 0.07$ mas), separated by 41 arcs or ~7200 au from HD 145502 A, has a marginally deeper line profile than HD 145502 A and B, with an EW of 250±10 mÅ compared with 220±10 mÅ. The secondary component HD 145501 B, separated

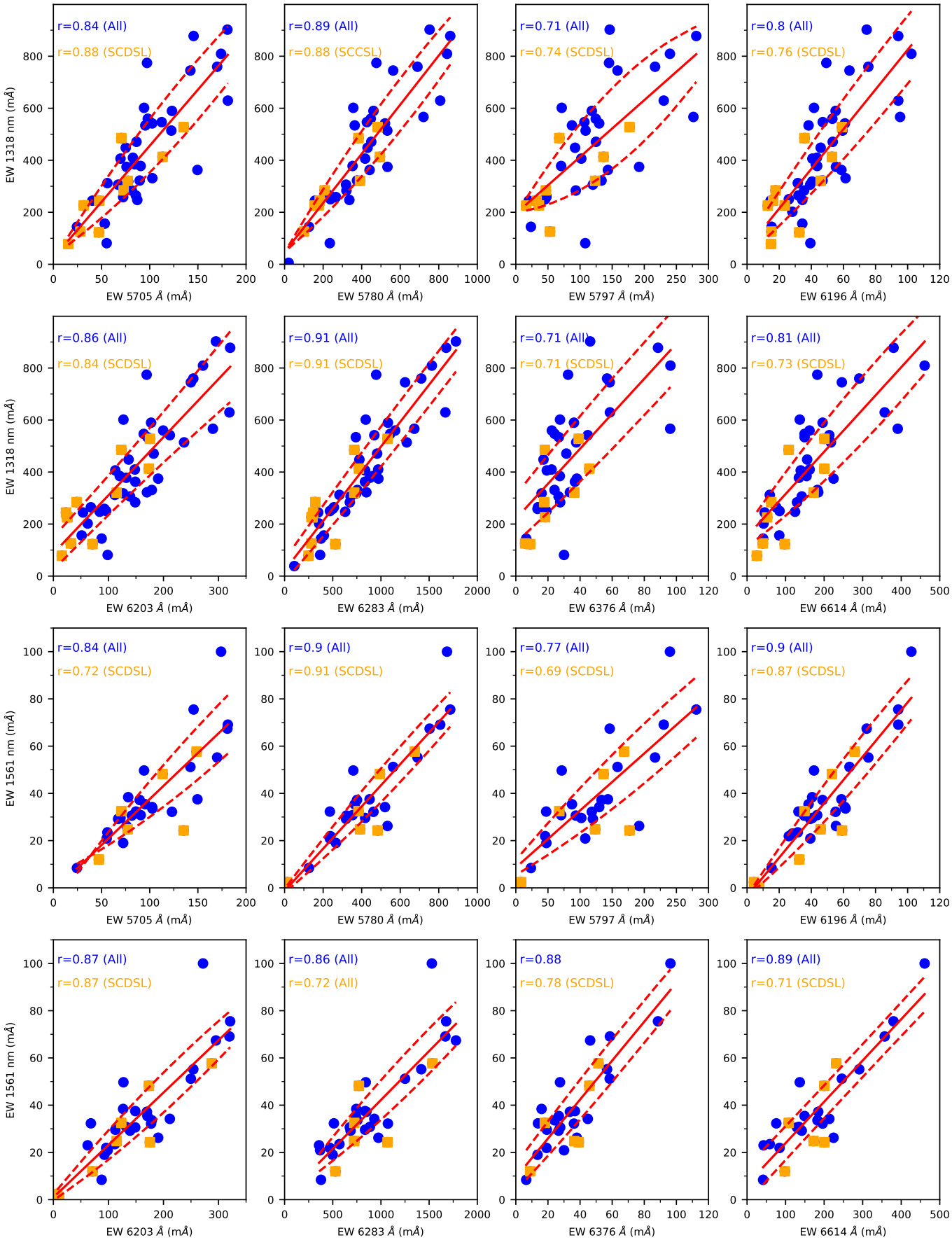

Fig. 20. Correlations in EW in mÅ for the 1318 nm and 1561 nm DIBs in the current sample towards the optical DIBs where the highest correlation coefficients were observed. The dashed lines show upper and lower error bounds obtained by fitting with a second order polynomial.

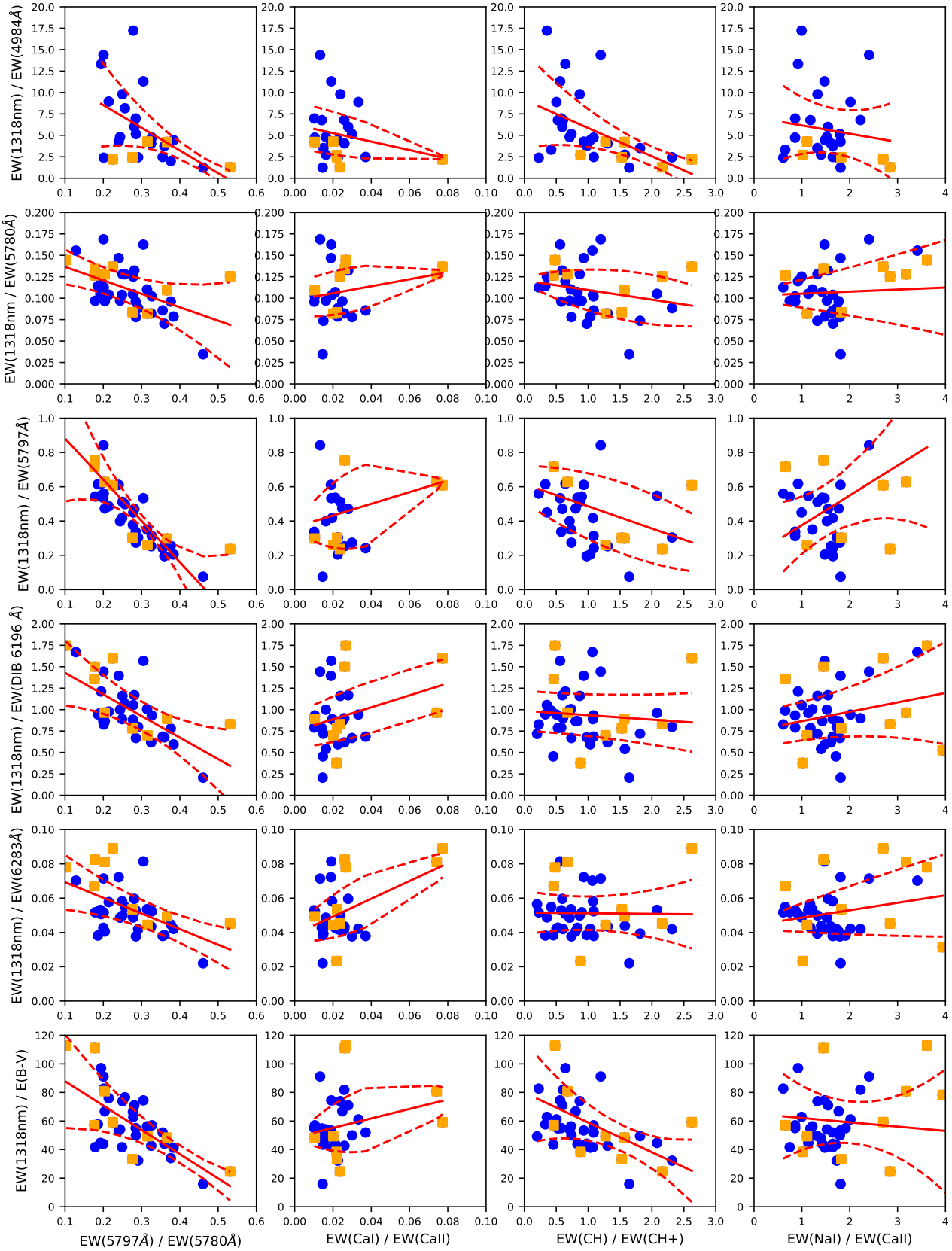

Fig. 21. Ratio of the EW of the 1318 nm NIR DIB divided by the EW of optical DIBs or $E(B-V)$ plotted against (1) $\lambda\lambda$5797/5780 ratio, (2) Ca I (4226 Å)/Ca II (3933 Å), (3) CH (4300 Å)/CH+ (4232 Å) and (4) Na I (5895 Å)/Ca II (3933 Å). Blue circles are for the whole sample, and orange squares show the single component dominated DIBs. The dashed lines show upper and lower error bounds obtained by fitting with a second order polynomial.

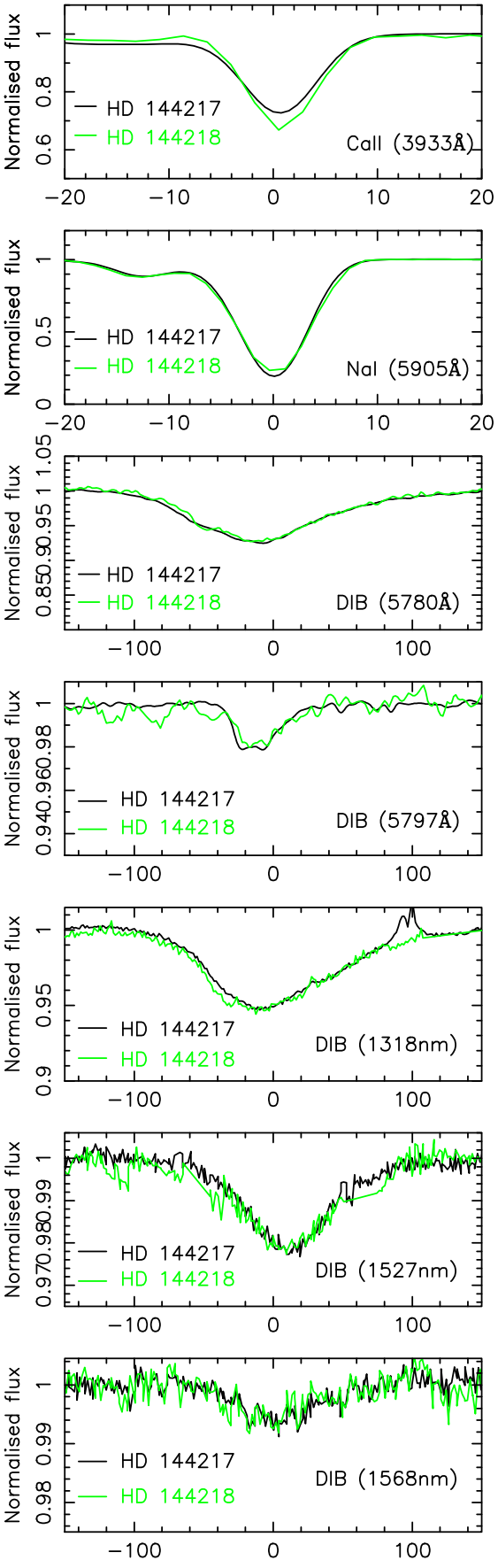

Fig. 22. Spectra of the binary stars HD 144217 and HD 144218 field in the Ca II, Na I line and 5780 Å, 5797 Å, 1318 nm, 1527 nm and 1567 nm DIBs.

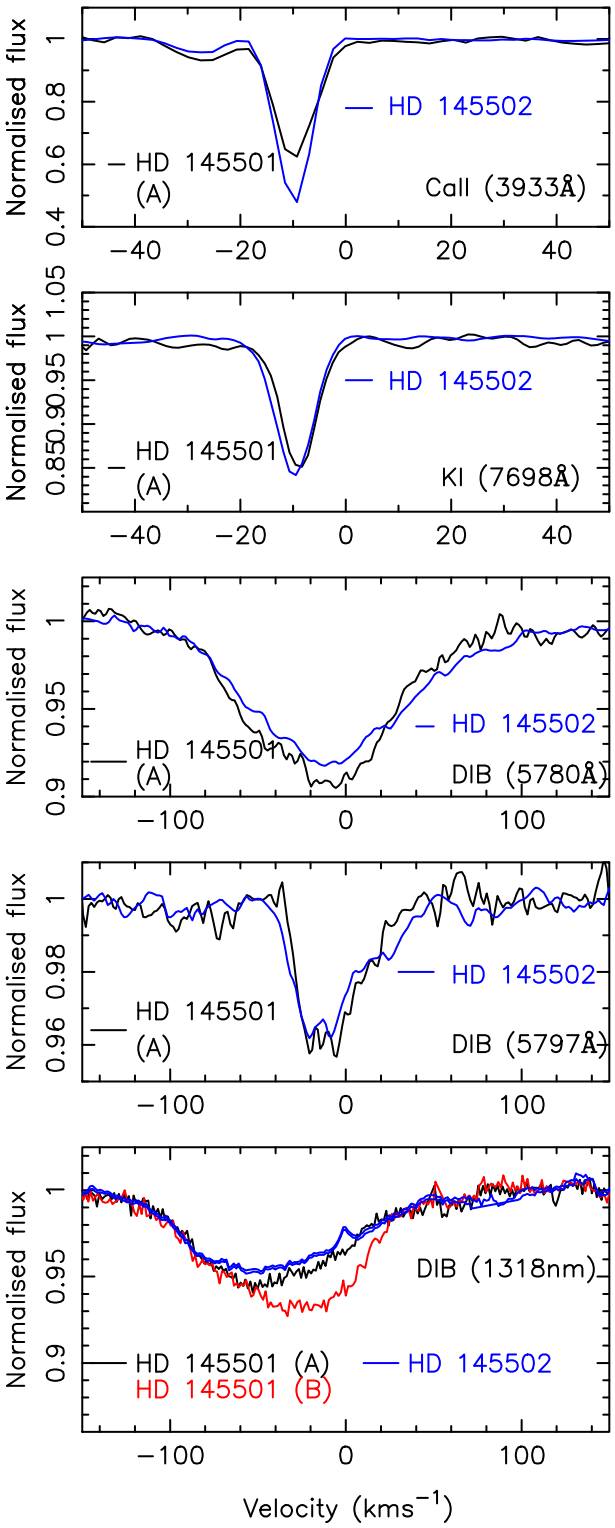

Fig. 23. Spectra of the HD 145501 and HD 144502 field in the Ca II and K I lines and 5780, 5797 Å and 1318.1 nm DIBs. We note that HD 145502 is a close binary.

by 2.5 arcsec, has a different profile shape and stronger EW of 310±10 mÅ. However, its spectral type and parallax are unknown and the proper motion of −8.0±0.4, −24.0±0.3 mas yr^{-1} is different to that of HD 145501 A, which has a proper motion of −11.9±0.1 −24.4±0.1 mas yr^{-1}. Hence HD 145501 B may well be a line-of-sight companion. The blue absorption line components at 1315.5 and 1316.8 nm are only seen in the HD 145501

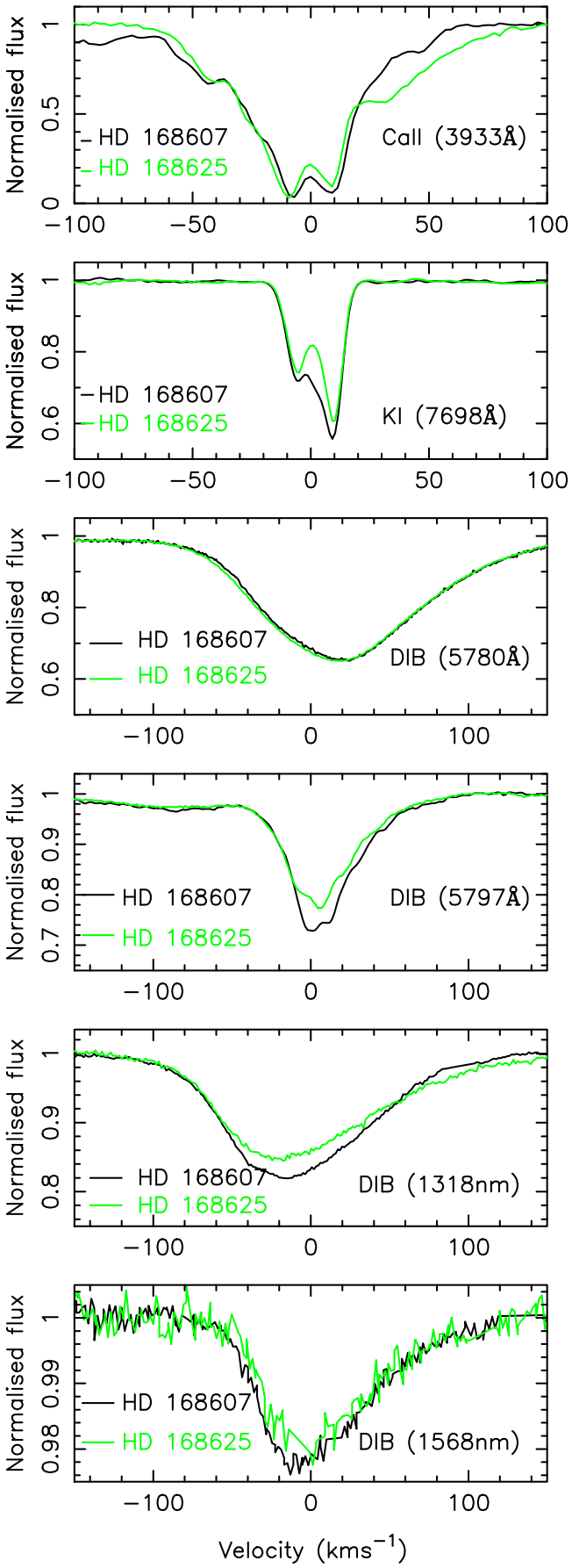

Fig. 24. Spectra of the HD 168607 and HD 168625 field in the Ca II, K I lines and 5780, 5797 Å and 1318 and 1568 nm DIBs.

B spectrum and are likely stellar. Finally, there are some indications that the DIB at 1527 nm is also stronger in HD 145501 A and B than HD 145502 A and B, although the data are rather noisy.

The two components of spectroscopic binary HD 145502 (nu Sco A and nu Sco B) are separated by 1.35 arcsec, and no obvious difference is visible in their 1318.1 nm DIB profiles, which have EWs of 220±10 mÅ. Their proper motions are −7.65±0.71 and −23.71±0.47 mas yr^{-1}, with parallax unknown for HD 145501 and 6.88±0.76 mas for HD 145502, both from Hipparcos data. The stars have no parallax or proper motion data in *Gaia* DR2. Figure 23 shows the available K I, 5780 Å, 5797 Å and 1318 nm data towards the field, and Table 6 shows the NIR DIB EW measurements.

Comparing with optical data, the variation occurring between the main components of HD 145501 and HD 145502 in the 1318 nm DIB is also reflected in the 5780 Å DIB but not in the K I line and only marginally in the 5797Å DIB. We note that in the data from Cordiner et al. (2013), the 5797 Å DIB showed more variation than the 5780 Å feature. The observed small-scale structure seen by comparing HD 145501 A and B profiles may just be caused by the objects being at different distances. A spectroscopic parallax for this object would be useful.

The second field where possible variation was seen in the 1318 nm line is the HD 160065 field. HD 160065 has $E(B-V)$ of 1.06 mag., and another star with separation of ∼18.6 arcsec was put on the slit. The 'companion' has no reference in SIMBAD. The spectrum of the second star is far noisier than that of HD 160065, but a clear difference in the DIB strength is seen. Follow-up work on this star would be needed to determine its distance.

The final field where there is some evidence for infrared DIB structure is in the region that contains the stars HD 168607 ($\pi = 0.6438 \pm 0.0603$ mas) and HD 168625 ($\pi = 0.6212 \pm 0.0640$ mas). These stars have similar reddenings ($E(B-V)$ = 1.54 and 1.47, respectively) and are separated in the sky by 67″, or around 0.52 pc. Possible variation in the 1318 nm line was seen. Clear variation was also seen in the K I line as well as possible variation in the 5797 Å DIB. Although the small scale variation of these three lines presented in Fig. 24 looks convincing, the baseline fitting is not straightforward. No clear variation was seen in the 5780 Å DIB.

Tables 6 and 7 show the EWs and percentage variations detected in the stars discussed above, and Fig. 25 shows spectra of binary and multiple systems observed around 1318 nm.

In conclusion, possible variation in the 1318 nm DIB is only seen around two double systems: HD 145501 and HD 145502, with separation of ∼7200 au, and HD 168607 and HD 168625, with separation of around 0.52 pc or 107 000 au.

4.5.2. Search for time variability

Seventeen of our sightlines were observed twice by CRIRES, with the epochs separated by six to 14 months, for the purpose of searching for time variable structure in NIR DIBs. Additionally, two of our X-shooter sightlines observed in conditions of low water vapour in August 2019 were previously observed in 2010 and published by Cox et al. (2014). These are also used to search for time variation in the 5780, 5797, C_{60}^+ 9577, and 9632 Å DIBs.

Table 8 lists the stars that were observed at more than one epoch in order to check for time variability in the ISM. The transverse distances derived from the Hipparcos proper motions range

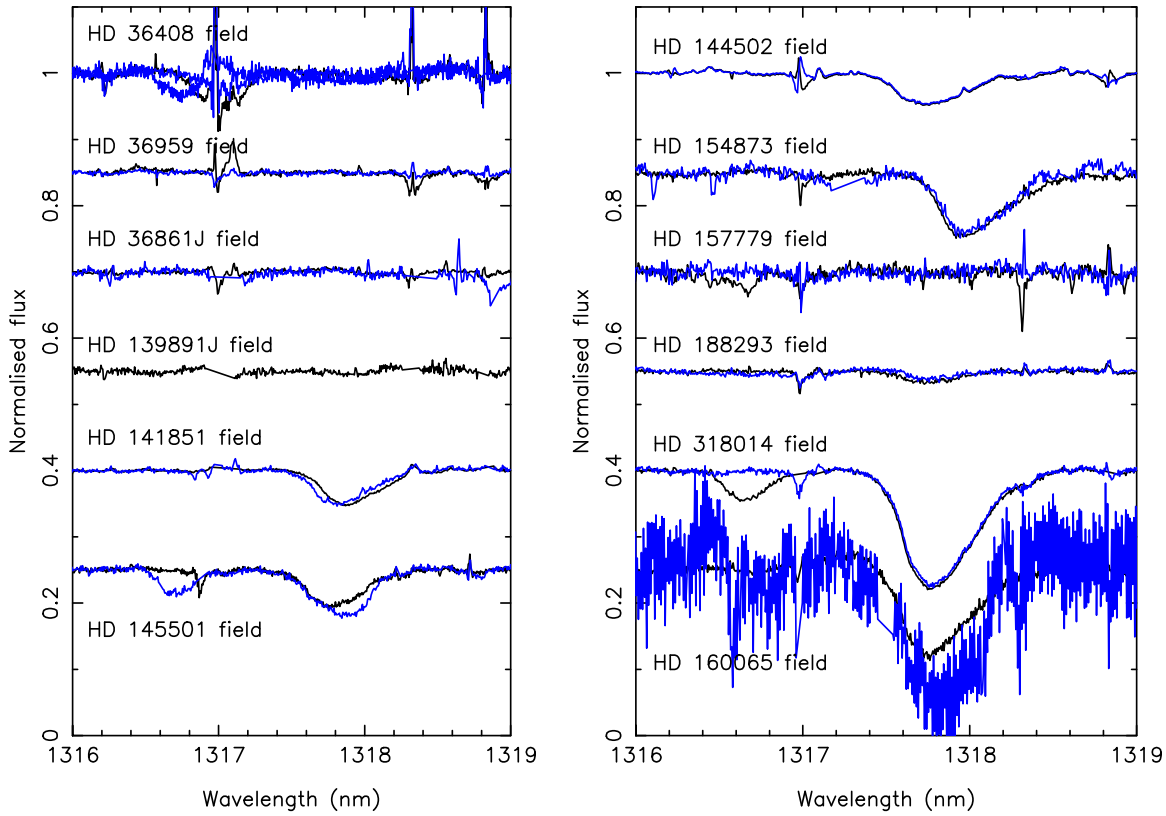

Fig. 25. Spectra of binary and multiple systems observed around 1318 nm.

Table 6. Equivalent widths of sightlines with companions within one arcminute that had a NIRDIB detection.

Star	EW Ca II (mÅ)	EW Na I (mÅ)	EW K I (mÅ)	EW DIB(5780 Å) (mÅ)	EW DIB(5797 Å) (mÅ)	EW DIB(1318 nm) (mÅ)	EW DIB(1527 nm) (mÅ)
HD 144217	40±1	148±1	–	157±1	16±1	220±10	83±4
HD 144218	38±2	152±2	–	148±2	16±1	240±10	99±4
HD 145501 A	58±2	–	35±1	175±3	31±1	250±10	–
HD 145501 B	–	–	–	–	–	310±10	–
HD 145502 A	62±1	–	37±1	172±2	33±1	220±10	–
HD 145502 B	–	–	–	–	–	220±10	–
							–
HD 160065	–	–	–	–	–	600±20	–
No name	–	–	–	–	–	1100±120	–
HD 168607	768±3	695±2	220±2	880±5	359±5	870±10	–
HD 168625	793±3	683±2	182±2	887±5	305±5	800±10	–
HD 188293	19±1	–	–	–	–	64±4	42±6
HD 188294	17±1	80±1	30±1	–	–	41±6	35±9
HD 318014	808±15	–	194±3	643±5	–	910±20	–
LS 4256	–	–	–	–	–	880±10	–

from 1.7±0.3 to 24±3 au. Time variability, although uncommon, has been found in over 20 cases in atomic lines such as Na I, as well as in singly ionised lines, such as Ca II (e.g. Hobbs et al. 1991; Crawford et al. 2000; Smoker et al. 2011; see Lauroesch 2007 and Stanimirović & Zweibel 2018 for reviews). Regarding the optical wavelength regime, a twin-epoch study of more than 100 early-type stars by McEvoy et al. (2015) found that in spectra with $R = 80\,000$ to 160 000 and S/Ns of several hundreds, typically a few percent of sightlines (corresponding to less than 1% of all components) in the diffuse interstellar medium show such time variation in optical lines on timescales from 6–20 yr. In their survey, time variable structure was only sightlines with upper limits of 50 au or more of transverse separation. Previous claims of time variability in DIBs have been made by

Table 7. Variation in EW in percent for sightlines where NIR DIBs were detected.

Main object	Companion star	Var. Ca II (%)	Var. Na I (%)	Var. K I (%)	Var. DIB (5880 Å) (%)	Var. DIB (5897 Å) (%)	Var. DIB (1318 nm) (%)	Var. DIB (1527 nm) (%)
HD 144217	HD 144218	5±7	–3±2	–	6±2	0±12	–9±9	–16±9
HD 145501 A	HD 145501 B	–	–	–	–	–	–20±7	–
HD 145501 A	HD 145502 A	–6±5	–	–6±5	2±3	–6±6	14±8	–
HD 145502 A	HD 145502 B	–	–	–	–	–	0±9	–
HD 160065	No name	–	–	–	–	–	–45±14	–
HD 168607	HD 168625	–3±1	2±1	20±2	–1±1	18±3	9±2	–
HD 188293	HD 188294	11±10	–	–	–	–	56±20	20±40
HD 318014	LS 4256	–	–	–	–	–	4±3	–

Notes. Where available, optical data are shown.

Table 8. Objects with repeat observations at 1318 nm (for CRIRES data C) and with X-shooter low water vapour data (XL) at 1318 nm and 1527 nm (for 4U 1907+09 and HD 183143 only) to search for time variability in the ISM.

HD number	Observation dates	Inst.	PM (mas yr^{-1}) RA Dec	π (mas)	Transverse. dist. (au)
4U 1907+09	2010-Jul-02 2019-Aug-10	XL	–	–	–
HD 106068	2013-May-27 2014-Mar-16	C	–5.18±0.06 –0.24±0.06	0.58±0.04	7.1±1.9
HD 112272	2013-May-28 2014-Mar-16	C	–8.49±0.05 –7.93±0.05	0.63±0.04	14.5±0.9
HD 115363	2013-Jun-22 2014-Mar-16	C	–8.81±0.05 –1.92±0.05	0.27±0.04	24.1±3.4
HD 116119	2013-Jun-22 2014-Mar-17	C	–5.71±0.04 –1.71±0.05	0.22±0.03	19.6±2.9
HD 125241	2013-May-16 2014-Mar-20	C	–6.92±0.04 –1.99±0.06	0.41±0.03	14.6±1.3
HD 142468	2013-May-16 2014-Mar-20	C	–2.52±0.07 –3.05±0.06	0.46±0.05	7.2±0.7
HD 144969	2013-May-16 2014-Mar-20	C	3.31±0.63 –1.85±0.32	0.50±0.21	6.3±3.1
HD 147932	2013-Jun-24 2014-Jun-17	C	–9.34±0.15 –21.94±0.09	7.46±0.07	3.1±0.1
HD 148379	2013-May-16 2014-Mar-22	C	–2.97±0.19 –4.04±0.11	0.33±0.13	12.7±5.2
HD 148937	2013-May-21 2014-Mar-23	C	0.88±0.08 –3.38±0.04	0.88±0.05	3.3±0.3
HD 154873	2013-Sep-04 2014-Mar-17	C	2.57±0.09 –3.17±0.07	0.97±0.06	2.2±0.2
″	2013-Sep-04 2014-Mar-30	C	″	″	2.4±0.2
HD 157038	2013-May-22 2014-May-15	C	–0.20±0.11 –0.60±0.08	0.36±0.05	1.7±1.0
HD 159455	2013-May-23 2013-Jun-25	C	0.06±0.11 –0.90±0.08	0.34±0.06	0.2±0.0
″	2013-May-23 2014-Apr-17	C	″		2.4±0.3
HD 160065	2013-May-22 2014-Mar-30	C	1.18±0.11 –1.46±0.08	0.47±0.06	3.4±0.6
HD 162168	2013-Jun-02 2014-Apr-27	C	–0.70±0.11 –1.13±0.09	0.70±0.06	1.7±0.3
HD 183143	2013-Apr-11 2014-Jun-23	C	–1.09±0.06 –5.57±0.08	0.41±0.05	16.6±2.1
″	2010-Jul-02 2019-Aug-09	XL	″	″	124±16
HD 318014	2013-May-13 2014-Apr-17	C	0.16±0.10 –1.40±0.08	0.43±0.05	3.0±2.0

Notes. Parallaxes and proper motions are from *Gaia*. The transverse distance travelled by the star between the first and last epoch is shown in the last column.

Law et al. (2017) and, more recently, by Farhang (in prep.) in the DIBs at 4735, 5547, 6196, and 6602 Å in high-resolution UVES, FEROS, and HARPS data towards early-type stars in the EDIBLES sample. The changes are typically very close to the noise level and will have to be followed-up with long-term monitoring. Non-detection of time variability in the 5780, 5797, and 6613 Å DIBs towards ζ Oph was recently reported by Cox et al. (2020).

Four examples of our CRIRES spectra and two observed with X-shooter at twin epochs are shown in Fig. 26. No time variability was detected in the 1318.1 nm DIB in the CRIRES data nor in the 5780.5, 5797.1 Å, 1318.1, and 1527.4 nm DIBs. Tentative time variation was observed in the C_{60}^+ DIBs at 9577 and 9632 Å in the spectrum of HD 183143, although very close to the noise level and with confirmation required at a higher spectral resolution, as continuum fitting and telluric line corrections are not straightforward. Although the transverse distance travelled in 9.9 yr of 124 au is the largest in our sample, variation is not seen in the 5780 or 5797Å DIBS.

5. Summary and future work

We have undertaken a mini-survey of several NIR DIBs using CRIRES with limited wavelength coverage. These data were supplemented by lower S/N and resolution X-shooter observations of ten highly reddened Cepheid variables, 19 archival

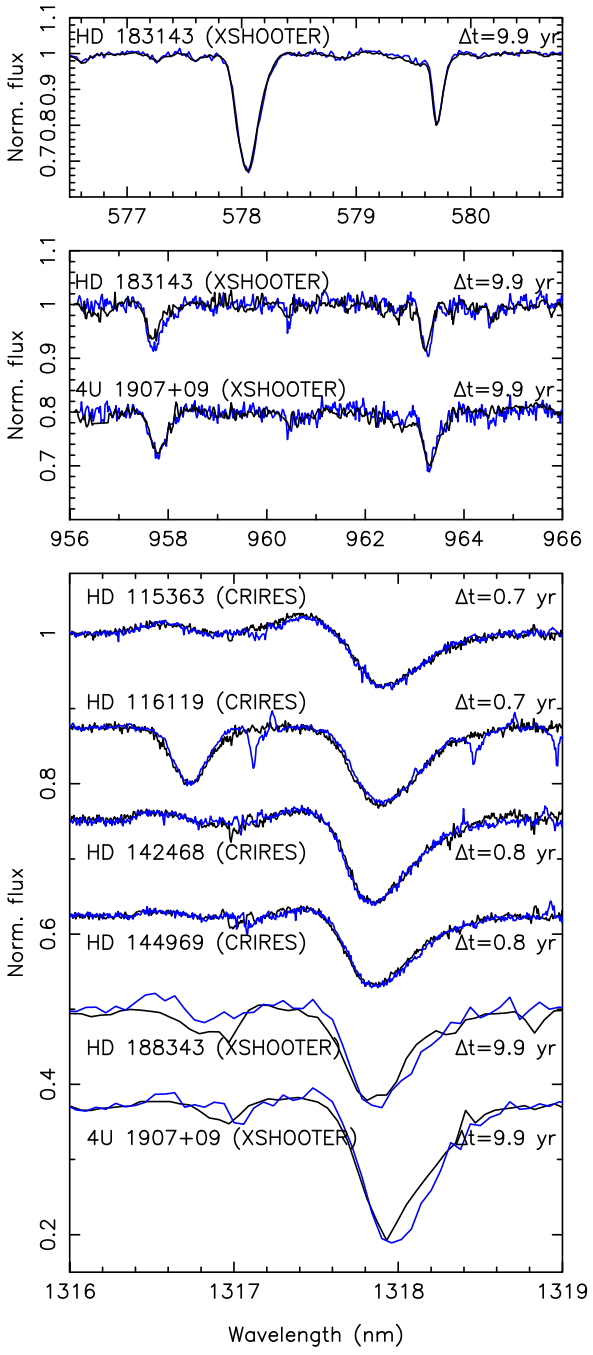

Fig. 26. Examples of normalised spectra for which twin epochs were taken separated by more than six months. *Top panel*: 5797 and 5780 Å DIBs observed with X-shooter at low PWV (4U 1907+09 not shown due to low S/N). *Middle panel*: The same C_{60}^+ DIBs observed with X-shooter. *Bottom panel*: 1318.1 nm NIR DIBs. The black line is the earlier epoch and the blue line the later epoch. For HD 115363, HD 116119, HD 142468, HD 144969, and HD 183143, the transverse distances moved by the star between the two epochs are 24.0±3.4, 19.5±2.9, 7.2±0.7, 6.4±3.1, and 138±20 au, respectively. The parallax and proper motions for 4U 1907+09 are not available in SIMBAD.

X-shooter targets, and towards four stars observed at very low values of water vapour in order to investigate time variability of the C_{60}^+-DIBs and correlations with the NIR DIBs. Our findings can be stated as follows:

(1) The NIR DIBs studied are reasonably well correlated with the strong optical bands, in particular those at 5705, 5780, 6203, 6283, and 6269 Å. The 5797 Å DIB is less well correlated with NIR DIB strengths. Using DIB ratios, and as found by previous authors, this implies that the NIR DIBs are σ type (unshielded) DIBs as opposed to the ζ DIB that are affected by UV radiation. The NIR DIBs are not well correlated with the C_{60}^+-DIB at 9632.1 Å nor the 5797 Å DIB, although the numbers are small.

(2) Correlations with reddening are fair to good with r values for the whole dataset of ~0.89 for the 1318 nm DIB.

(3) The 1318 nm DIB does not have a Gaussian profile shape but has a red wing that can be fitted adequately using two Gaussian functions. The integrated flux ratio of the two components is not correlated with reddening or the $\lambda\lambda$5780/5797 flux ratio.

(4) Regarding star types earlier than B2, the 1318 nm DIB often displays an emission feature to the blue. It is unclear if this is stellar, circumstellar, or interstellar in nature.

(5) In spectra with S/Ns of several hundreds and spectral resolving power of ~50 000, variation in the 1318 nm DIB was found towards two near equidistant stellar systems (HD 145501/HD 145502 and HD 168607/HD 168625). Variations of ~14 and ~9% in the 1318 nm line were observed with transverse separations of 7200 au and 0.52 pc. Two further sightlines (HD 145501 and line-of-sight companion separated by 2.5 arcsec, and HD 165501 with line-of-sight companion separated by 18.6 arcsec) also show small-scale variation in the 1318 nm line, but the distance to the companion object is uncertain in both cases. The remaining stellar pairs show no difference in their 1318 nm profiles.

(6) No time variation was detected regarding the 1318 nm DIB on timescales of 6–14 months of 17 sightlines nor for the two additional stars observed with X-shooter over epochs separated by 9.9 yr. One of the two stars (HD 183143) showed tentative time variation for the C_{60}^+-DIBs at 9577 and 9632 Å, although it was very close to the noise level.

Future work will use the upgraded CRIRES spectrometer (Dorn et al. 2014) and its expanded wavelength coverage to look for new DIBs in the infrared, check for emission in the 1318 nm DIBS towards the Red Rectangle, search for polarisation in the 1318 nm absorption and emission line DIBs, and observe more sightlines in the 1527 nm band at high spectral resolution.

Acknowledgements. We thank the referee Ed Jenkins for many useful corrections and suggestions that improved the paper. J.V.S. thanks the UK Astronomy Technology Centre for hospitality. A.M.I., K.T.S. and M.E. thank ESO for funding under the auspices of the Director General's Discretionary Fund. A.M.I. acknowledges support from the Spanish MINECO through project AYA2015-68217-P. F.N. acknowledges funding by grants PID2019-105552RB-C41 and MDM-2017-0737-19-3 Unidad de Excelencia "María de Maeztu". Observations were performed as ESO programmes 091.C-0655, 093.C-0480 and 0103.C-0766(A) and archival data taken from ESO programmes 072.D-0286, 081.C-0475, 266.D-5655, 194.C-0833, 082.C-0566, 083.C-0503, 194.C-0833, 074.D-0240, 194.C-0833, 081.D-2002, 194.C-0833, 284.D-5048, 60.A-9036, 079.C-0597 and 095.A-9029. This research has made use of the SIMBAD database operated by CDS in Strasbourg.

References

Alecian, E., Kochukhov, O., Petit, V., et al. 2014, A&A, 567, A28
Allamandola, L. J., Tielens, A. G. G. M., & Barker, J. R. 1989, ApJS, 71, 733
Bagnulo, S., Jehin, E., Ledoux, C., et al. 2003, The Messenger, 114, 10
Bailey, M., van Loon, J. T., Farhang, A., et al. 2016, A&A, 585, A12
Brown, A. G. A., & Verschueren, W. 1997, A&A, 319, 811
Cami, J., Sonnentrucker, P., Ehrenfreund, P., & Foing, B. H. 1997, A&A, 326, 822
Cami, J., Salama, F., Jiménez-Vicente, J., Galazutdinov, G. A., & Krełowski, J. 2004, ApJ, 611, L113

Cami, J., Cox, N. L., Farhang, A., et al. 2018, The Messenger, 171, 31
Campbell, E. K., Holz, M., Gerlich, D., & Maier, J. P. 2015, Nature, 523, 322
Campbell, E. K., Holz, M., Maier, J. P., et al. 2016, ApJ, 822, 17
Cardelli, J. A., Clayton, G. C., & Mathis, J. S. 1989, ApJ, 345, 245
Chen, Y.-P., Trager, S. C., Peletier, R. F., et al. 2014, A&A, 565, A117
Cordiner, M. A., Smith, K. T., Cox, N. L. J., et al. 2008, A&A, 492, L5
Cordiner, M. A., Cox, N. L. J., Evans, C. J., et al. 2011, ApJ, 726, 39
Cordiner, M. A., Fossey, S. J., Smith, A. M., & Sarre, P. J. 2013, ApJ, 764, L10
Cordiner, M. A., Cox, N. L. J., Lallement, R., et al. 2017, ApJ, 843, L2
Cordiner, M. A., Linnartz, H., Cox, N. L. J., et al. 2019, ApJ, 875, L28
Cox, N. L. J. 2011, in EAS Publications Series, 46, eds. C. Joblin, & A. G. G. M. Tielens, 349
Cox, N. L. J., Cordiner, M. A., Cami, J., et al. 2006, A&A, 447, 991
Cox, N. L. J., Ehrenfreund, P., Foing, B. H., et al. 2011, A&A, 531, A25
Cox, N. L. J., Cami, J., Kaper, L., et al. 2014, A&A, 569, A117
Cox, N. L. J., Cami, J., Farhang, A., et al. 2017, A&A, 606, A76
Cox, N. L. J., Smith, K. T., & Cordiner, M. A. 2020, RNAAS, 4, 28
Crawford, I. A. 2002, MNRAS, 334, L33
Crawford, I. A., Howarth, I. D., Ryder, S. D., & Stathakis, R. A. 2000, MNRAS, 319, L1
Crowther, P. A., Hadfield, L. J., Clark, J. S., Negueruela, I., & Vacca, W. D. 2006, MNRAS, 372, 1407
David, T. J., Hillenbrand, L. A., Gillen, E., et al. 2019, ApJ, 872, 161
Dekker, H., D'Odorico, S., Kaufer, A., Delabre, B., & Kotzlowski, H. 2000, SPIE Conf. Ser., 4008, 534
Dorn, R. J., Anglada-Escude, G., Baade, D., et al. 2014, The Messenger, 156, 7
Ebbets, D. 1995, in Calibrating Hubble Space Telescope. Post Servicing Mission, eds. A. P. Koratkar, & C. Leitherer, 207
Ebenbichler, A., Postel, A., Przybilla, N., et al. 2022, A&A, 662, A81
Elyajouri, M., & Lallement, R. 2019, A&A, 628, A67
Elyajouri, M., Lallement, R., Monreal-Ibero, A., Capitanio, L., & Cox, N. L. J. 2017, A&A, 600, A129
Fan, H., Welty, D. E., York, D. G., et al. 2017, ApJ, 850, 194
Fan, H., Schwartz, M., Farhang, A., et al. 2022, MNRAS, 510, 3546
Farhang, A., Khosroshahi, H. G., Javadi, A., & van Loon, J. T. 2015, ApJS, 216, 33
Fitzgerald, M. P. 1970, A&A, 4, 234
Fossey, S. J. 1991, Nature, 353, 393
Friedman, S. D., York, D. G., McCall, B. J., et al. 2011, ApJ, 727, 33
Gaia Collaboration (Vallenari, A., et al.) 2023, A&A, in press, https://doi.org/10.1051/0004-6361/202243940
Galazutdinov, G. A., Lee, J.-J., Han, I., et al. 2017a, MNRAS, 467, 3099
Galazutdinov, G. A., Shimansky, V. V., Bondar, A., Valyavin, G., & Krełowski, J. 2017b, MNRAS, 465, 3956
Geballe, T. R., Najarro, F., Figer, D. F., Schlegelmilch, B. W., & de La Fuente, D. 2011, Nature, 479, 200
Glinski, R. J., Michaels, P. D., Anderson, C. M., et al. 2009, Ap&SS, 323, 337
Gontcharov, G. A. 2006, Astron. Astrophys. Trans., 25, 145
Hamano, S., Kobayashi, N., Kondo, S., et al. 2015, ApJ, 800, 137
Hamano, S., Kobayashi, N., Kondo, S., et al. 2016, ApJ, 821, 42
Hamano, S., Kobayashi, N., Kawakita, H., et al. 2022, ApJS, 262, 2
Heger, M. L. 1922, Lick Observatory Bull., 10, 141
Herbig, G. H. 1993, ApJ, 407, 142
Hillier, D. J., & Lanz, T. 2001, in Astronomical Society of the Pacific Conference Series, 247, Spectroscopic Challenges of Photoionized Plasmas, eds. G. Ferland, & D. W. Savin, 343
Hobbs, L. M., Ferlet, R., Welty, D. E., & Wallerstein, G. 1991, ApJ, 378, 586
Hobbs, L. M., York, D. G., Snow, T. P., et al. 2008, ApJ, 680, 1256
Hobbs, L. M., York, D. G., Thorburn, J. A., et al. 2009, ApJ, 705, 32
Joblin, C., D'Hendecourt, L., Leger, A., & Maillard, J. P. 1990, Nature, 346, 729
Kaeufl, H.-U., Ballester, P., Biereichel, P., et al. 2004, SPIE Conf. Ser., 5492, 1218
Kaufer, A., Stahl, O., Tubbesing, S., et al. 1999, The Messenger, 95, 8
Kerber, F., Querel, R. R., Rondanelli, R., et al. 2014, MNRAS, 439, 247
Kerr, T. H., Hibbins, R. E., Miles, J. R., et al. 1996, MNRAS, 283, L105
Kervella, P., Arenou, F., Mignard, F., & Thévenin, F. 2019, A&A, 623, A72
Kharchenko, N. V., Scholz, R. D., Piskunov, A. E., Röser, S., & Schilbach, E. 2007, Astron. Nachr., 328, 889
Kochukhov, O., & Bagnulo, S. 2006, A&A, 450, 763
Koen, C., & Eyer, L. 2002, MNRAS, 331, 45
Kos, J., Zwitter, T., Grebel, E. K., et al. 2013, ApJ, 778, 86
Krelowski, J., & Walker, G. A. H. 1987, ApJ, 312, 860
Kuhn, M., Renzler, M., Postler, J., et al. 2016, Nat. Commun., 7, 13550
Lallement, R., Welsh, B. Y., Vergely, J. L., Crifo, F., & Sfeir, D. 2003, A&A, 411, 447
Lallement, R., Cox, N. L. J., Cami, J., et al. 2018, A&A, 614, A28
Lan, T.-W., Ménard, B., & Zhu, G. 2015, MNRAS, 452, 3629
Lauroesch, J. T. 2007, Astronomical Society of the Pacific Conference Series, 365, Optical Absorption Line Observations of Small Scale Interstellar Structure, eds. M. Haverkorn, & W. M. Goss, 40
Lauroesch, J. T., & Meyer, D. M. 1999, ApJ, 519, L181
Law, C. J., Milisavljevic, D., Crabtree, K. N., et al. 2017, MNRAS, 470, 2835
MacIsaac, H., Cami, J., Cox, N. L. J., et al. 2022, A&A, 662, A24
Maíz Apellániz, J., Barbá, R. H., Sota, A., & Simón-Díaz, S. 2015, A&A, 583, A132
Malkan, M. A., Hicks, E. K., Teplitz, H. I., et al. 2002, ApJS, 142, 79
Marshall, C. C. M., Krełowski, J., & Sarre, P. J. 2015, MNRAS, 453, 3912
Mattioda, A. L., Hudgins, D. M., & Allamandola, L. J. 2005, ApJ, 629, 1188
McCall, B. J., Drosback, M. M., Thorburn, J. A., et al. 2010, ApJ, 708, 1628
McEvoy, C. M., Smoker, J. V., Dufton, P. L., et al. 2015, MNRAS, 451, 1396
Meeus, G., Waters, L. B. F. M., Bouwman, J., et al. 2001, A&A, 365, 476
Merrill, P. W., & Wilson, O. C. 1938, ApJ, 87, 9
Meyer, D. M., & Lauroesch, J. T. 1999, ApJ, 520, L103
Minniti, J. H., Sbordone, L., Rojas-Arriagada, A., et al. 2020, A&A, 640, A92
Monreal-Ibero, A., Weilbacher, P. M., & Wendt, M. 2018, A&A, 615, A33
Moutou, C., Krełowski, J., D'Hendecourt, L., & Jamroszczak, J. 1999, A&A, 351, 680
Munari, U. 2000, in Molecules in Space and in the Laboratory, 67, eds. I. Porceddu, & S. Aiello, 179
Najarro, F., Geballe, T. R., Figer, D. F., & de la Fuente, D. 2017, ApJ, 845, 127
Pepe, F., Mayor, M., Delabre, B., et al. 2000, SPIE Conf. Ser., 4008, 582
Perruchot, S., Kohler, D., Bouchy, F., et al. 2008, SPIE Conf. Ser., 7014, 70140J
Raimond, S., Lallement, R., Vergely, J. L., Babusiaux, C., & Eyer, L. 2012, A&A, 544, A136
Rawlings, M., Adamson, A., McCall, B., & Kerr, T. 2011, in IAU Symposium, 280, The Molecular Universe, eds. J. Cernicharo, & R. Bachiller, 311
Routly, P. M., & Spitzer, Lyman, J. 1952, ApJ, 115, 227
Ruiterkamp, R., Cox, N. L. J., Spaans, M., et al. 2005, A&A, 432, 515
Russeil, D., Zavagno, A., Adami, C., et al. 2012, A&A, 538, A142
Salama, F., Bakes, E. L. O., Allamandola, L. J., & Tielens, A. G. G. M. 1996, ApJ, 458, 621
Sarre, P. J. 1991, Nature, 351, 356
Sarre, P. J. 2014, in IAU Symposium, 297, The Diffuse Interstellar Bands, eds. J. Cami, & N. L. J. Cox, 34
Sembach, K. R., Howk, J. C., Ryans, R. S. I., & Keenan, F. P. 2000, ApJ, 528, 310
Smette, A., Sana, H., Noll, S., et al. 2015, A&A, 576, A77
Smoker, J., Haddad, N., Iwert, O., et al. 2009, The Messenger, 138, 8
Smoker, J. V., Bagnulo, S., Cabanac, R., et al. 2011, MNRAS, 414, 59
Snow, T. P. J., & Cohen, J. G. 1974, ApJ, 194, 313
Sonnentrucker, P., York, B., Hobbs, L. M., et al. 2018, ApJS, 237, 40
Stanimirović, S., & Zweibel, E. G. 2018, ARA&A, 56, 489
Stütz, C., Bagnulo, S., Jehin, E., et al. 2006, A&A, 451, 285
Swihart, S. J., Garcia, E. V., Stassun, K. G., et al. 2017, AJ, 153, 16
Valdivia, V., Godard, B., Hennebelle, P., et al. 2017, A&A, 600, A114
Vallat, R. 2018, J. Open Source Softw., 3, 1026
Vallerga, J. V., Vedder, P. W., Craig, N., & Welsh, B. Y. 1993, ApJ, 411, 729
van de Hulst, H. C. 1946, Rech. Astron. Observ. Utrecht, 11, 2.i
van Loon, J. T., Bailey, M., Tatton, B. L., et al. 2013, A&A, 550, A108
Vernet, J., Dekker, H., & et al., D. 2011, A&A, 536, A105
Vink, J. S., & Sander, A. A. C. 2021, MNRAS, 504, 2051
Vio, R., Nagler, T. W., & Andreani, P. 2020, A&A, 642, A156
Vos, D. A. I., Cox, N. L. J., Kaper, L., Spaans, M., & Ehrenfreund, P. 2011, A&A, 533, A129
Walker, G. A. H., Campbell, E. K., Maier, J. P., & Bohlender, D. 2017, ApJ, 843, 56
Watson, J. K., & Meyer, D. M. 1996, ApJ, 473, L127
Wegner, W. 1994, MNRAS, 270, 229
Wegner, W. 2003, Astron. Nachr., 324, 219
Welty, D. E., Hobbs, L. M., & Morton, D. C. 2003, ApJS, 147, 61
Welty, D. E., Federman, S. R., Gredel, R., Thorburn, J. A., & Lambert, D. L. 2006, ApJS, 165, 138
Wendt, M., Husser, T.-O., Kamann, S., et al. 2017, A&A, 607, A133
Weselak, T., Galazutdinov, G. A., Sergeev, O., et al. 2014, Acta Astron., 64, 371
Wickramasinghe, N. C. 1968, Nature, 217, 412
Wraight, K. T., Fossati, L., Netopil, M., et al. 2012, MNRAS, 420, 757
Wu, C. C., York, D. G., & Snow, T. P. 1981, AJ, 86, 755
Xiang, F. Y., Li, A., & Zhong, J. X. 2017, ApJ, 835, 107
Zasowski, G., Chojnowski, S. D., Whelan, D. G., et al. 2015a, ApJ, 811, 119
Zasowski, G., Ménard, B., Bizyaev, D., et al. 2015b, ApJ, 798, 35
Zhekov, S. A., Tomov, T., Gawronski, M. P., et al. 2014, MNRAS, 445, 1663

Appendix A: The sample

Table A.1. Stellar sample sorted alphabetically and split into CRIRES and X-shooter subsections.

Target	Inst.	Spectral type	*l*,*b* (deg.)	m_B	m_V (mag.)	m_H	$(B-V)_0$ Fitz.	$(B-V)_0$ Weg.	E(B-V)	$N_{\rm Obs}$ a b c d e
HD 36408 A	C	B7-8IV-V	188.49 −08.89	6.10	6.09	6.02	−0.13	…	…	1 1 1 – –
HD 36408 B	C	B7II	188.49 −08.89	6.53	6.49	6.28	−0.13	…	0.17	1 1 1 – –
HD 36861	CAO	O8III	195.05 −12.00	3.48	3.66	3.77	−0.30	−0.30	0.12	1 1 – – –
HD 36862	CAO	B0.5V	195.05 −11.99	…	6.32	…	…	…	…	1 1 – – –
HD 36959	C	B1VvYSO	209.57 −19.72	5.44	5.67	6.24	−0.26	−0.23	0.01	1 1 1 – –
HD 36960	C	B1/2Ib/II	209.56 −19.71	4.50	4.72	5.38	−0.17	−0.16	0.03[1]	1 1 1 – –
HD 89587	C	B3III	279.84 +05.19	6.74	6.87	7.20	−0.20	…	0.07	1 – – 1 –
HD 88661	C	B5Vne	283.08 −01.48	5.66	5.75	5.57	−0.16	−0.15	0.06	1 – – 1 1
HD 90706	C	B2.5Ia	284.52 +00.00	7.56	7.10	5.84	−0.15	−0.14	0.61	1 – – 1 1
HD 92740	C	WN7h+	287.17 −00.85	6.50	6.42	5.58	…	…	0.36	1 – – 1 1
	C	O9III-V								
HD 93130	C	O6.5III	287.56 −00.86	8.31	8.04	7.26	…	…	0.56[2]	1 – – 1 –
HD 93632	C	O5I	288.03 −00.87	8.57	9.10	7.06	…	…	0.62[3]	1 – – 1 –
HD 94910	C	WN11h	289.18 −00.70	7.57	6.96	5.08	…	…	0.59	1 – – 1 1
HD 97707	C	B11b	291.26 −00.11	8.57	8.07	6.77	…	…	0.67	1 – – 1 1
HD 100841	C	B9III	294.47 −01.40	3.10	3.14	3.10	−0.08	…	0.04	1 – – 1 1
HD 105056	C	ON9.7Ia	298.96 −07.06	7.48	7.34	7.14	−0.27	−0.27	0.41	1 – – 1 –
HD 105071	C	B8Ia	298.24 −03.09	6.45	6.31	5.67	−0.01	−0.03	0.16	1 – – 1 1
HD 106068	C	B8Ia/Iab	298.51 −00.42	6.28	5.98	5.04	−0.01	−0.03	0.32	2 – – 1 1
HD 111774	C	B8V	303.04 +23.19	5.89	5.97	6.21	−0.11	−0.11	0.03	1 – – 1 1
HD 112272	C	B0.5Ia	303.49 −01.49	8.03	7.39	5.36	−0.22	−0.20	0.85	2 – – 1 1
HD 113904	C	WC5+B0III	304.67 −02.49	5.50	5.53	…	…	…	0.25[4]	1 – – 1 1
	C	O9IV								
HD 115088	C	B9.5/A0V	304.18 −17.17	6.31	6.33	6.47	−0.04	−0.06	0.03	2 – – 2 1
HD 115363	C	B1Ia	305.88 −00.96	8.32	7.82	6.13	−0.19	−0.19	0.69	2 – – 1 1
HD 115842	C	B0.5Ia	307.08 +06.83	6.39	6.09	5.30	−0.22	−0.20	0.51	1 – – 1 1
HD 116119	C	A0Ia	306.62 +00.63	8.58	7.87	5.88	0.00	0.00	0.71	2 – – 1 1
HD 125007	C	B9V	319.45 +17.49	7.00	7.03	7.03	−0.07	−0.07	0.04	1 – – 1 –
HD 125241	C	O8.5Ib	313.54 +00.14	9.08	8.60	6.99	−0.29	−0.30	0.77	2 – – 1 1
HD 137753	C	B7IV	325.93 +03.34	6.66	6.69	6.68	−0.13	…	0.10	1 – – 1 1
HD 139891	C	B9V	058.69 +53.41	5.82	5.93	…	−0.07	−0.07	0.07	1 1 – – –
HD 139892	C	B7V	058.69 +53.41	4.87	4.98	5.30	…	…	…	1 1 – – –
HD 142468	C	B1Ia/Iab	327.95 −00.76	8.48	7.90	6.41	−0.19	−0.19	0.77	2 – – 1 1
HD 144217	CAO	B1V	353.19 +23.60	2.55	2.62	2.80	…	…	0.20	1 1 1 – –
HD 144218	CAO	B2V	353.20 +23.60	4.87	4.89	4.47	…	…	…	1 1 1 – –
HD 144969	C	B1Ia	333.18 +02.01	9.32	8.39	5.68	−0.19	−0.19	1.12	2 – – 1 1
HD 145482	C	B2V	348.12 +16.84	4.42	4.57	5.01	−0.24	−0.21	0.07	2 – – 2 2
HD 145501A	CAO	B8V+	354.61 +22.71	6.43	6.30	5.69	−0.09	−0.09	0.22	1 1 1 – –
	CAO	B9VpSi								
HD 145501B	CAO	…	354.61 +22.71	7.54	7.23	…	…	…	…	1 1 1 – –
HD 145502A	C	B2V	354.61 +22.71	4.35	4.35	…	−0.24	−0.21	0.28	1 1 1 – –
HD 145502B	C	…	354.61 +22.70	6.72	6.60	…	…	…	…	1 1 1 – –
HD 146331	C	B9V	350.41 +17.53	8.69	8.30	7.19	−0.07	−0.07	0.46	1 – – 1 –
HD 147932	CAO	B5V	353.72 +17.71	7.59	7.27	5.92	−0.16	−0.15	0.48	1 – – 1 1
HD 148184	C	B2Vne	357.93 +20.67	4.71	4.43	3.26	−0.24	−0.21	0.51	1 – – 1 1
HD 148379	C	B2Iab	337.25 +01.57	5.95	5.37	3.83	−0.17	−0.16	0.74	2 – – 1 1
HD 148688	C	B1Ia	340.72 +04.34	5.78	5.39	4.24	−0.19	−0.19	0.58	1 – – 1 1
HD 148937	C	O6f?p	336.37 −00.22	7.12	6.71	5.74	…	…	0.66	
HD 151932	C	WN7h	343.22 +01.43	6.72	6.49	5.27	…	…	0.50[5]	1 – – 1 1
HD 152235	C	B0.5Ia	343.31 +01.10	6.92	6.38	4.94	−0.22	−0.20	0.75	1 – – 1 1

Table A.1. continued.

Target	Inst.	Spectral type	l,b (deg.)	m_B	m_V (mag.)	m_H	$(B-V)_0$ Fitz.	$(B-V)_0$ Weg.	E $(B-V)$	$N_{\rm Obs}$ a b c d e
HD 152386	C	O5/6I:fek	341.11 −00.94	8.64	8.13	6.62	−0.32	−0.31	0.83	1 – – 1 1
HD 154811	C	OC9.7Iab	341.06 −04.21	7.33	6.93	5.85	−0.27	−0.27	0.67	1 – – 1 1
HD 154873A	C	B1Ib	341.35 −04.10	6.98	6.70	…	−0.19	−0.19	0.47	3 1 2 2 1
HD 154873B	C	…	341.34 −04.11	8.49	8.23	…	…	…		3 1 2 2 1
HD 156134	C	B0Iab...	351.20 +01.36	8.70	8.05	6.41	−0.24	−0.22	0.88	1 – – 1 1
HD 156201	C	B0.5Ia	351.51 +01.48	8.70	8.01	6.10	−0.22	−0.20	0.90	1 – – 1 1
HD 156212	C	B0Iab	357.59 +05.82	8.34	7.95	6.57	−0.24	−0.22	0.62	1 – – 1 1
HD 156738	C	O6.5III	351.18 +00.48	10.27	9.35	6.92	−0.32	…	1.24	1 – – 1 –
HD 157038	C	B3Iap	349.95 −00.79	7.20	6.44	4.29	−0.13	−0.13	0.89	2 – – 1 1
HD 157778	C	A0Vn	061.22 +32.71	5.40	5.40	…	…	…	…	1 1 1 – –
HD 157779	C	B9.5III	061.44 +32.71	4.49	4.56	…	−0.05	…	0.00[5]	1 1 1 – –
HD 159455	C	B0.5Ia	355.23 −00.61	9.11	8.44	6.25	−0.22	−0.20	0.88	3 – – 2 2
HD 160065A	C	O9.5Iab	355.31 −01.35	9.41	8.60	6.17	−0.27	−0.24	1.06	2 – – 1 1
HD 160065B	C	…	…	…	…	…	…	…	…	1 – – – –
HD 161289	C	A0V	027.50 +16.03	6.60	6.54	6.38	0.00	0.00	0.07	1 – – – –
HD 161291	C	B0.5Iab	001.49 +00.85	9.61	8.88	7.04	−0.22	−0.20	0.94	1 – – 1 –
HD 162168	C	B0.5Iab	357.13 −03.08	9.04	8.42	6.84	−0.22	−0.20	0.83	2 – – 1 1
HD 164438	C	O9.2IV	010.35 +01.78	8.89	8.76	6.65	…	…	0.65	1 – – 1 1
HD 164865	C	B9Iab	006.21 −01.19	8.47	7.63	4.93	0.00	−0.01	0.85	1 – – 1 1
HD 165319	C	O9.7Ib	015.12 +03.33	8.63	8.04	6.36	−0.27	−0.24	0.85	1 – – 1 1
HD 166734	C	O7.5Iab	018.92 +03.62	9.49	8.42	5.53	−0.31	−0.30	1.37	1 – – 1 1
HD 167264	C	O9.7Iab	010.45 -01.74	5.42	5.37	5.21	−0.27	−0.27	0.32	1 – – 1 1
HD 167971	C	O8I+O5	018.25 +01.68	8.27	7.50	5.32	…	…	1.05[6]	1 – – 1 1
HD 168607	C	B9Iaep	014.97 −00.93	9.82	8.28	3.88	0.00	−0.01	1.54	1 – – 1 1
HD 168625	C	B6Iap	014.97 −00.95	9.78	8.37	4.54	−0.07	−0.06	1.47	1 – – 1 1
HD 168987	C	B1Ia/ab	014.99 −01.44	8.76	8.02	5.53	−0.19	−0.19	0.93	1 – – 1 1
HD 169034	C	B2Ia	017.66 −00.06	9.42	8.24	4.77	−0.17	−0.16	1.35	1 – – 1 1
HD 169454	C	B1Ia	017.53 −00.66	7.61	6.71	4.09	−0.19	−0.19	1.09	1 – – 1 1
HD 169754	C	B0.5Ia	020.02 +00.23	9.64	8.60	5.81	−0.22	−0.20	1.25	1 – – 1 1
HD 170938	C	B1Ia	016.84 −03.04	8.84	7.99	5.51	−0.19	−0.19	1.04	1 – – 1 1
HD 171722	C	B9V	324.68 −24.68	7.21	7.24	7.29	−0.07	−0.07	0.04	1 – – 2 –
HD 183143	C	B7Iae	053.24 +00.62	8.08	6.86	…	−0.04	−0.04	1.26	2 – – 2 2
HD 188293	C	B7Vn	032.66 −17.76	5.63	5.71	5.88	−0.13	−0.13	0.05	1 1 – – –
HD 188294	C	B8V	032.65 −17.76	6.42	6.44	6.51	−0.11	−0.11	0.09	1 1 – – –
HD 303188	C	B3	286.91 −00.30	9.90	9.19	6.64	…	…	0.75	1 – – 1 1
HD 312980	C	B0	010.70 −01.29	10.31	9.63	7.19	…	…	1.15[7]	1 – – 1 –
HD 318014	C	B8Iab:	355.07 −00.70	10.24	8.78	4.21	−0.02	−0.03	1.49	2 – – 1 1
HD 319699	C	O5V	351.32 +00.91	10.32	9.63	7.45	−0.32	−0.30	1.00	1 – – 1 –
HD 319702	C	O8III	351.34 +00.60	10.94	10.12	7.56	…	…	1.30[8]	2 – – 2 –
LS 4825	C	B1Ib	001.67 −06.62	12.04	11.99	…	−0.19	−0.19	0.24	1 – – 1 –

Table A.1. continued.

Target	Inst.	Spectral type	l,b (deg.)	m_B	m_V (mag.)	m_H	$(B-V)_0$ Fitz.	$(B-V)_0$ Weg.	E $(B-V)$	$N_{\rm Obs}$ a b c d e
4U 1907+09	XL	O8.5Iab	043.74 +00.48	19.41	16.35	...	...	...	3.48	– – – – –
ALS 18752	XL	O3.5III(f*)	353.17 +00.89	13.33	11.84	7.28	...	...	1.92[9]	– – – – –
ALS 19692	XL	O5.5IV(f)	353.11 +00.65	13.53	11.82	6.93	...	...	2.26[9]	– – – – –
B02	X	T2C	001.93 +01.44	...	...	14.00	...	...	3.35	– – – – –
B09	X	CC	355.22 −00.19	...	...	14.20	...	...	6.51	– – – – –
B19	X	CC	354.37 −00.44	...	...	13.76	...	...	3.27	– – – – –
B21	X	T2C	358.86 −00.85	...	...	13.45	...	...	4.10	– – – – –
B22	X	T2C	359.29 −00.71	...	...	12.75	...	...	4.27	– – – – –
B24	X	T2C	003.13 −00.97	...	...	13.42	...	...	3.66	– – – – –
D07	X	CC	339.26 −00.32	...	...	14.67	...	...	5.51	– – – – –
D20	X	CC	323.33 −00.13	...	...	13.07	...	...	3.57	– – – – –
D17	X	CC	346.13 +01.00	...	...	13.79	...	...	3.43	– – – – –
D18	X	T2C	346.16 +00.31	...	...	13.84	...	...	3.13	– – – – –
HD 35912	XA	B2/3V	201.88 −17.84	6.21	6.38	6.83	...	...	0.06[10]	– – – – –
HD 52266	XA	O9.5IIIn	219.13 −00.67	7.22	7.23	7.24	...	...	0.32[10]	– – – – –
HD 52973	XA	CC	195.75 +11.90	4.58	3.79	2.03	...	...	0.04[11]	– – – – –
HD 53367	XA	B0IV/Ve	223.70 −01.90	7.40	6.96	6.22	...	...	0.74[10]	– – – – –
HD 57060	XA	O7Iafpvar	237.82 −05.36	4.80	4.95	5.19	...	...	0.17[10]	– – – – –
HD 62542	XA	B3V	255.91 −09.23	8.21	8.03	7.58	...	...	0.35[10]	– – – – –
HD 108927	XA	B5V	301.91 −15.35	7.83	7.76	7.58	...	...	0.22[10]	– – – – –
HD 101602	XA	CC	294.95 −00.92	9.60	8.30	6.96	...	...	0.25[11]	– – – – –
HD 114213	XA	B1Ib	305.18 +01.31	9.88	8.96	6.46	...	...	1.12[10]	– – – – –
HD 139717	XA	CC	325.65 −00.16	10.68	9.22	5.18	...	...	0.89[11]	– – – – –
HD 147889	XA	B2III/IV	352.85 +17.04	8.73	7.90	4.94	...	...	1.07[10]	– – – – –
HD 152235	XA	B0.5Ia	343.31 +01.10	6.92	6.38	4.94	...	...	0.69[10]	– – – – –
HD 154368	XA	O9.5Iab	349.97 +03.21	6.63	6.13	4.85	...	...	0.78[10]	– – – – –
HD 168076	XA	O4III(f)	016.93 +00.83	8.72	8.25	6.66	...	...	0.74[10]	– – – – –
HD 170740	XA	B2/3II	021.05 −00.52	5.96	5.72	5.25	...	...	0.48[10]	– – – – –
HD 178287	XA	CC	028.20 −07.12	8.88	7.79	5.14	...	...	0.40[11]	– – – – –
HD 179315	XA	CC	039.15 −02.57	9.01	7.78	4.80	...	...	0.59[11]	– – – – –
HD 183143	XL	B6Ia	053.24 +00.63	8.08	6.86	...	...	...	1.26[10]	– – – – –
HD 214080	XA	B1/2Ib	044.80 −56.91	6.81	6.93	7.25	...	...	0.06[10]	– – – – –
HD 219188	XA	K0III	083.02 −50.17	6.90	7.06	7.43	...	...	0.13[10]	– – – – –

Notes: Targets are identified by HD number or alternative catalogue designations for those not in the HD catalogue. The instrument used is denoted by C for CRIRES (no adaptive optics), CAO for CRIRES using adaptive optics, X for data from Minniti et al. (2020), XA for archival X-shooter data, and XL for the X-shooter low water vapour sample. Spectral types, Galactic coordinates, and apparent magnitudes in the B, V, and H bands are taken from SIMBAD. CC indicates a classical Cepheid and T2C a type 2 Cepheid; the intrinsic colours of these stars vary over the pulsation period. Cepheid names are from Minniti et al. (2020), where B refers to a Bulge Cepheid and D to a Disc Cepheid. Intrinsic $(B-V)_0$ colours for the spectral type are taken from Fitzgerald (1970) and Wegner (1994); where the values differed, we took an average. Reddening E(B-V) was estimated by comparing the observed $(B-V)$ colours to the intrinsic colours, except for the entries taken from the literature shown in the footnote and towards the Cepheids, as explained in the text. $N_{\rm Obs}$ indicates the number of observations in each of the five wavelength regions observed using CRIRES, with central wavelengths (a) 1318.1 nm, (b) 1527.9 nm, (c) 1568.8 nm, (d) 1574.4 nm, and (e) 1624.2 nm. All wavelengths were observed in a single setting for X-shooter. There are no SIMBAD data for 145501 B nor 160065 B that were detected using CRIRES.

References. Published reddening values taken from: (1) Sonnentrucker et al. (2018); (2) Weselak et al. (2014); (3) Crowther et al. (2006); (4) Zhekov et al. (2014); (5) Swihart et al. (2017); (6) Xiang et al. (2017); (7) Wegner (2003); (8) Russeil et al. (2012); (9) Maíz Apellániz et al. (2015); (10) Fan et al. (2017); (11) Chen et al. (2014).

Appendix B: CRIRES spectra

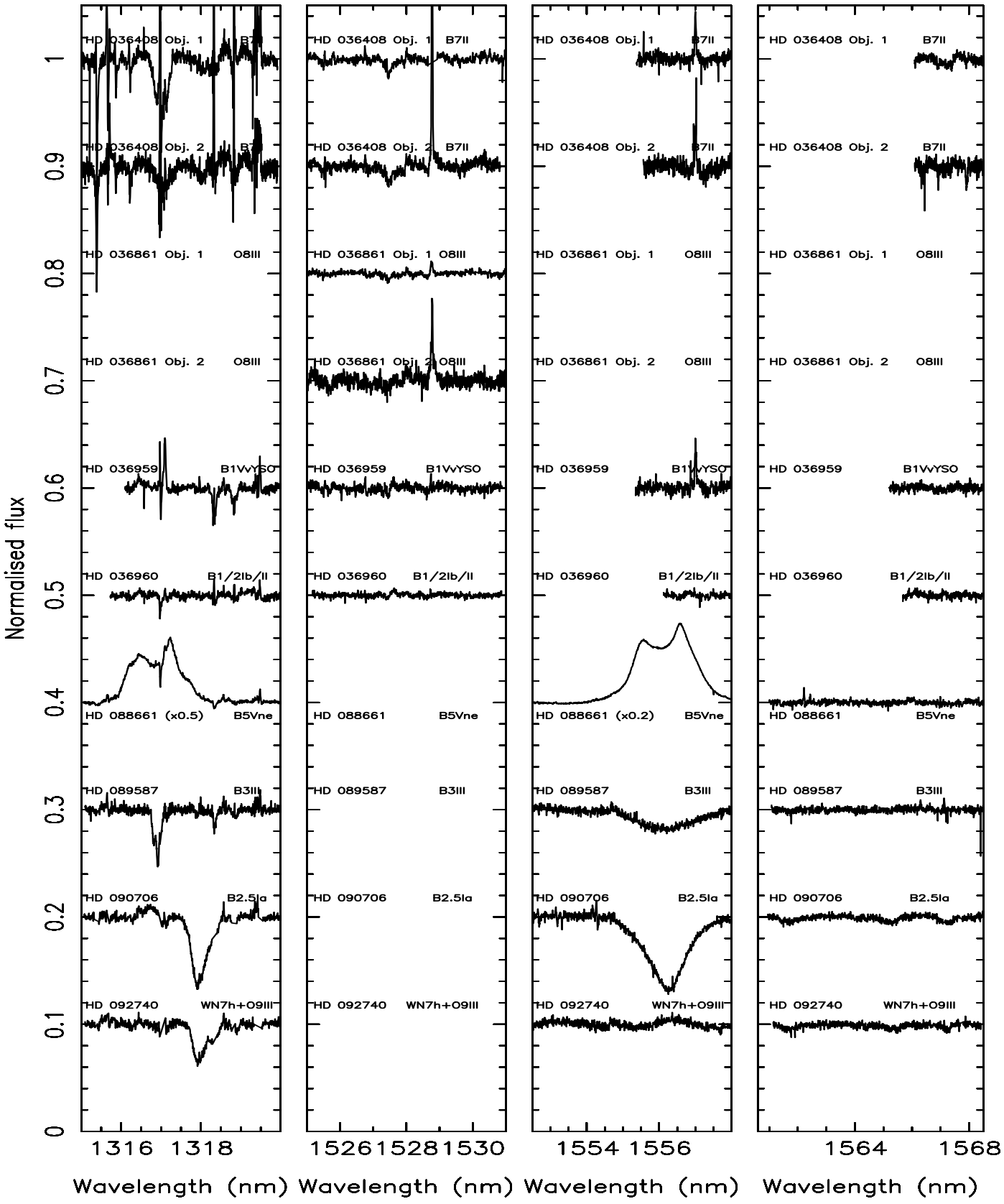

Fig. B1. Normalised CRIRES spectra around 1318, 1528, 1555, or 1565 nm offset in the ordinate for clarity.

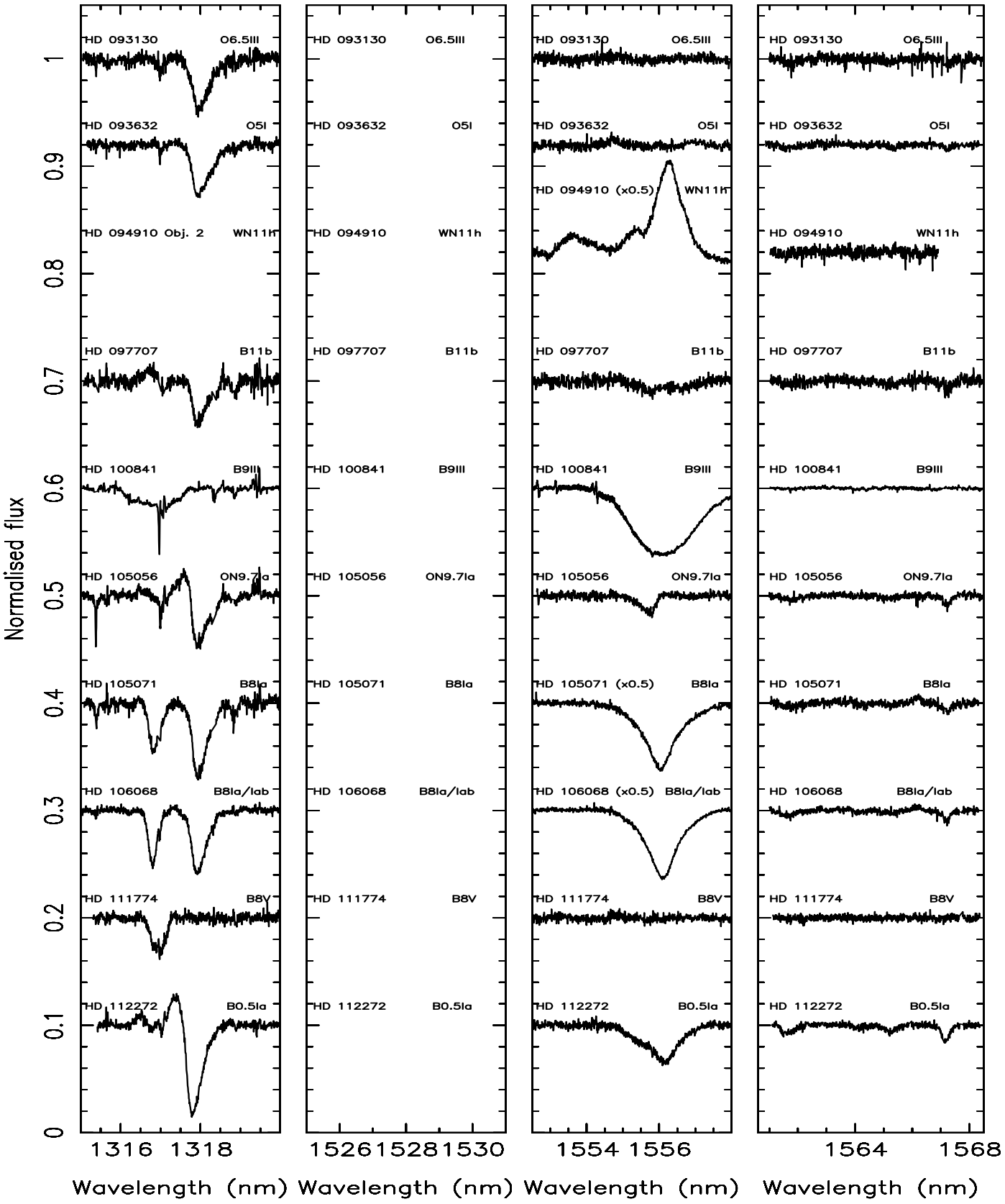

Fig. B1. continued.

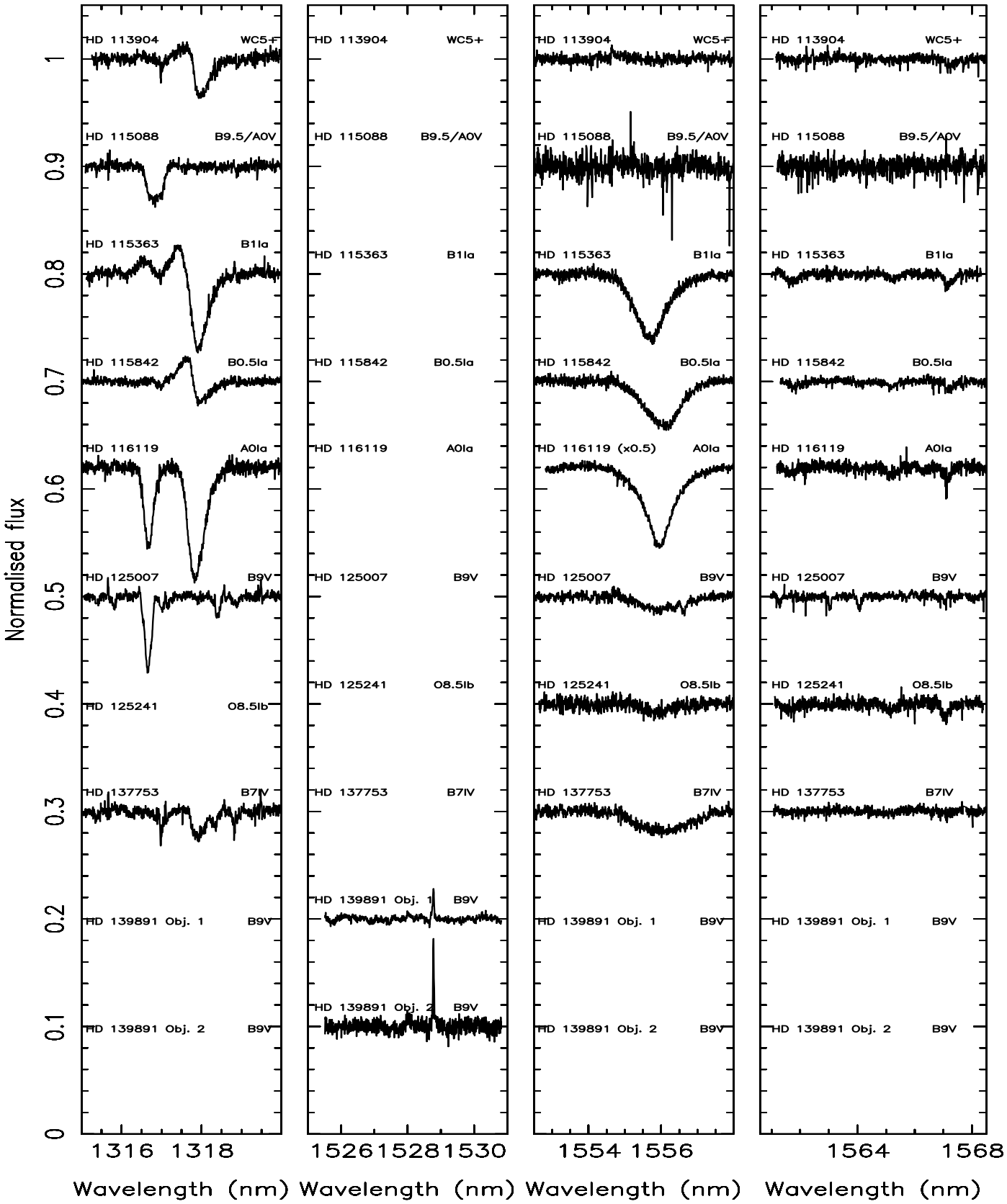

Fig. B1. continued.

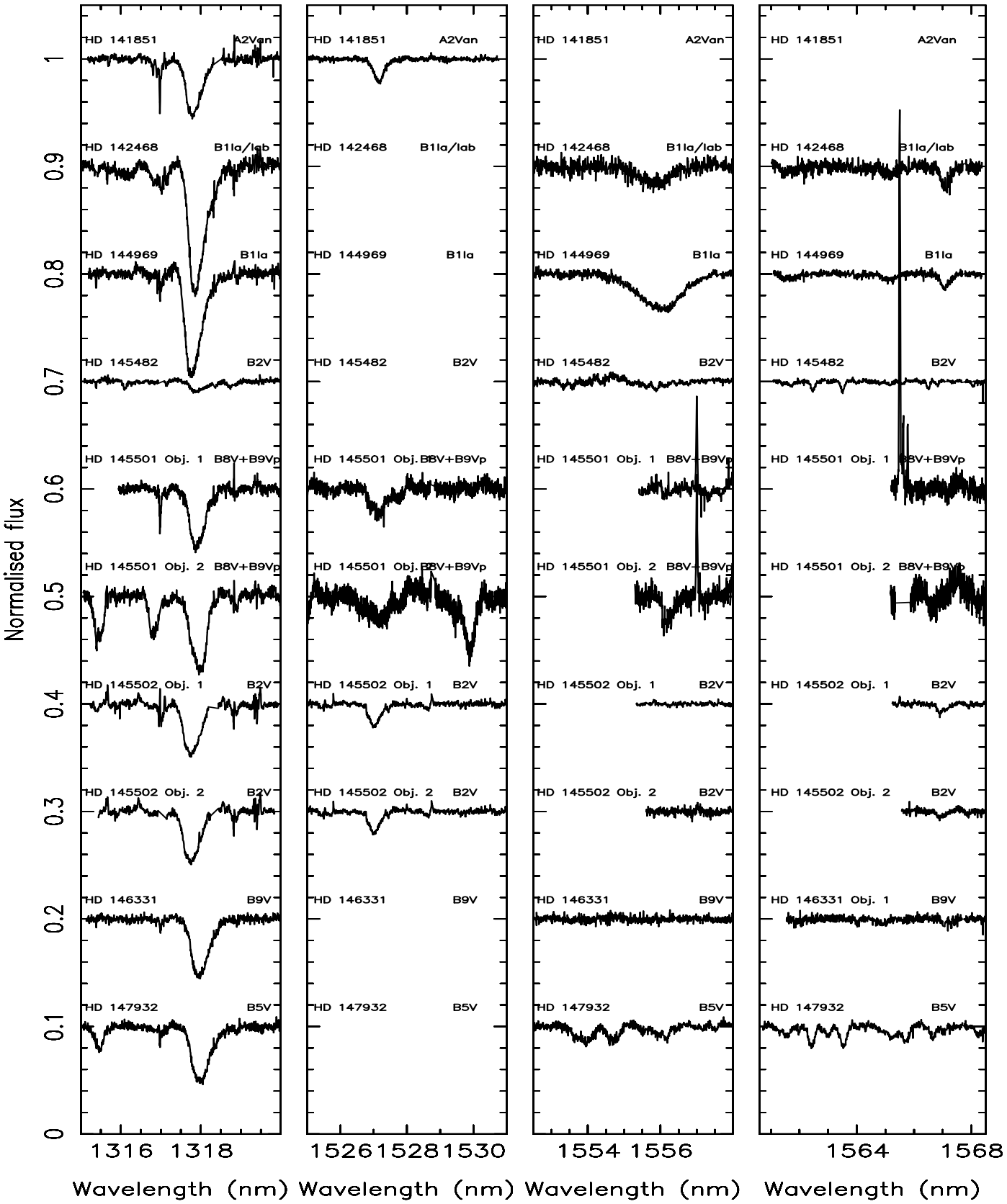

Fig. B1. continued.

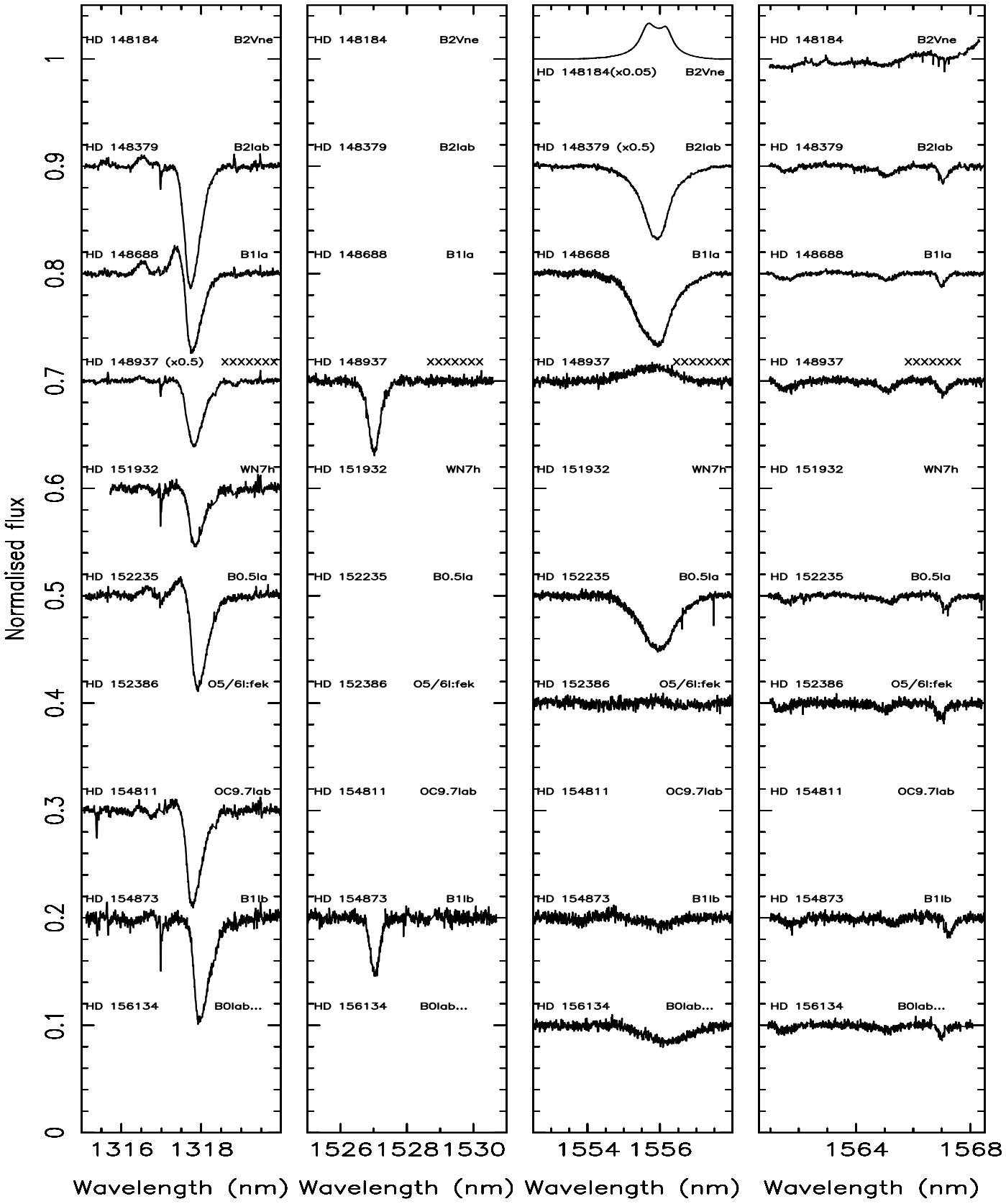

Fig. B1. continued.

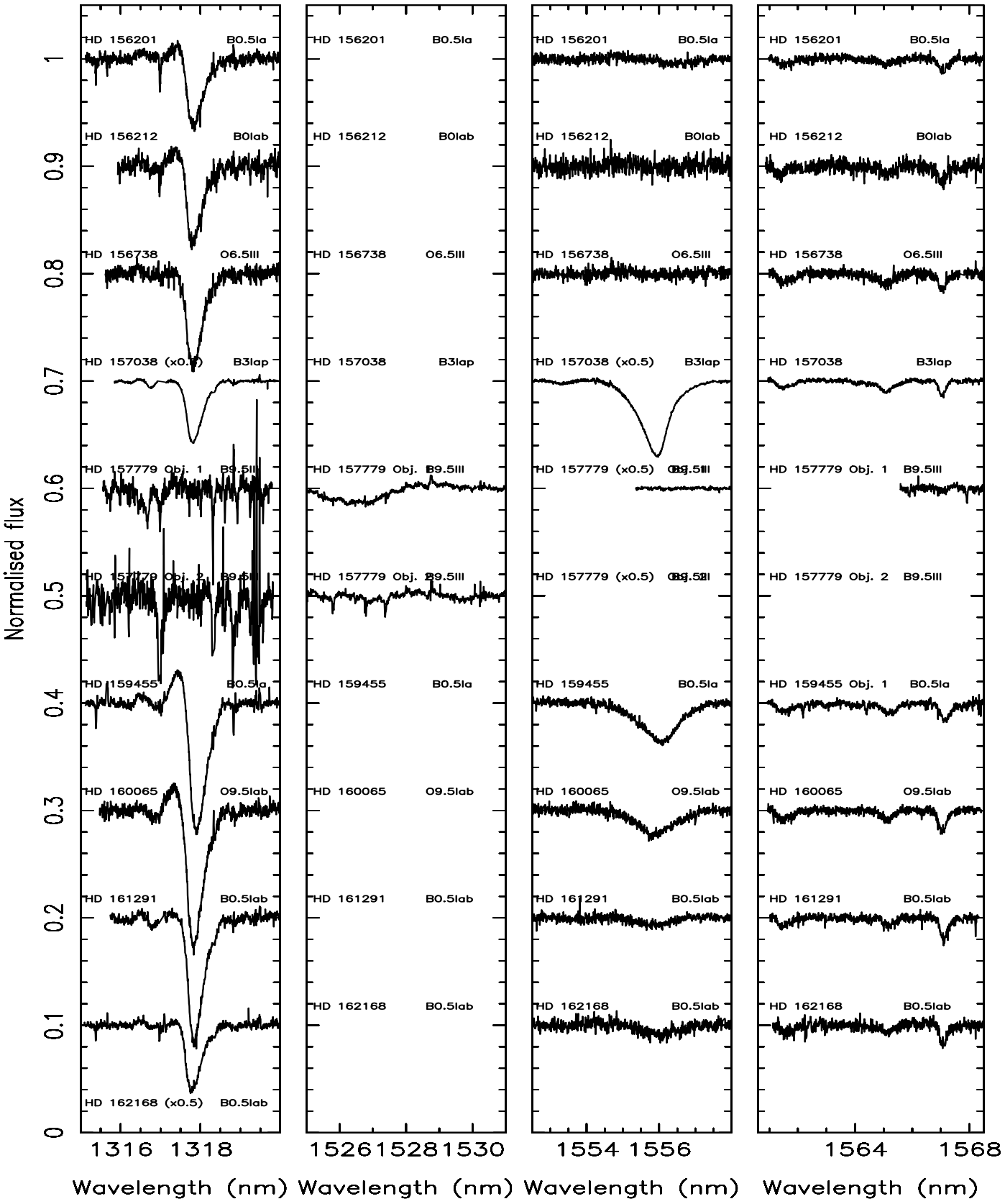

Fig. B1. continued.

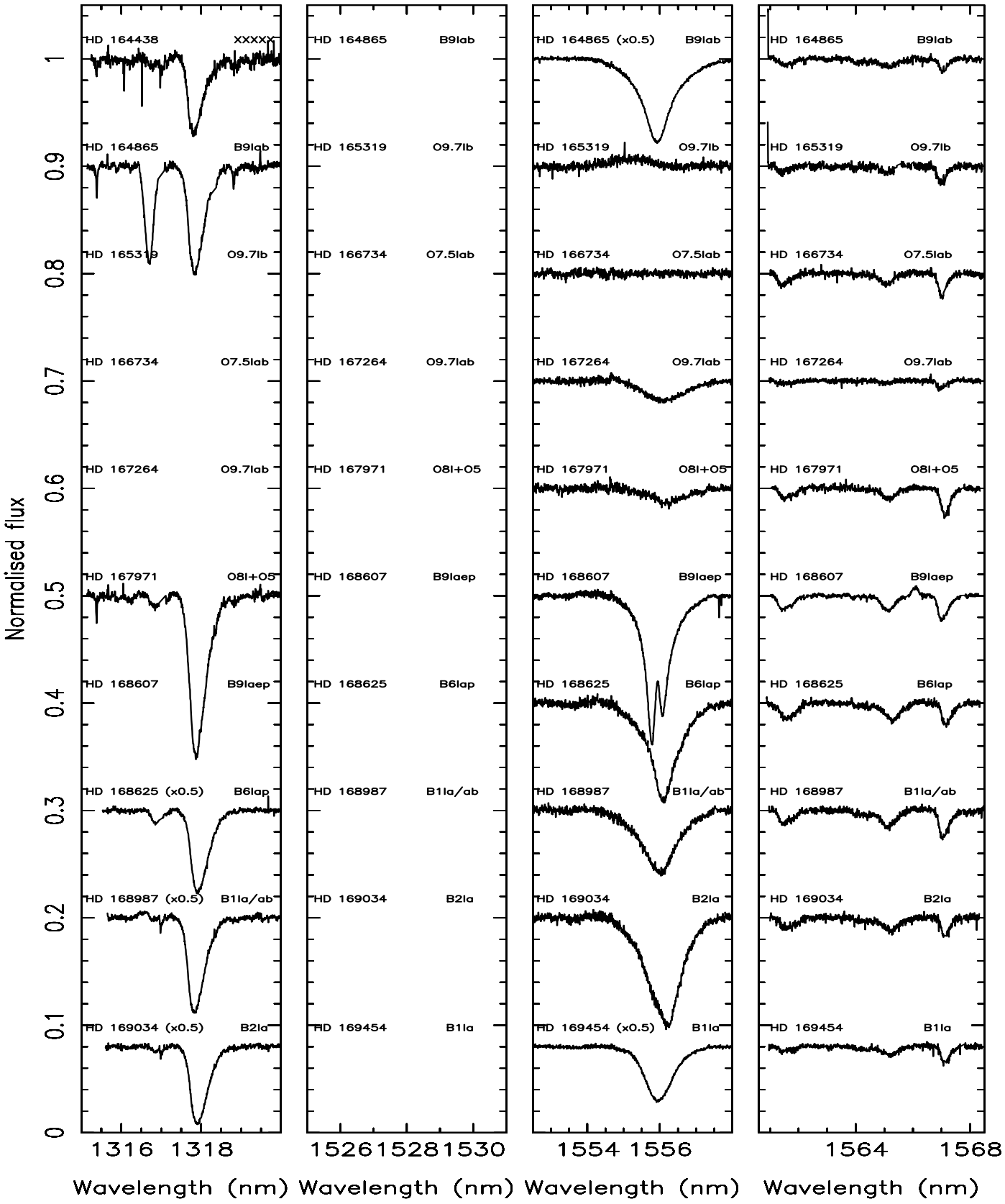

Fig. B1. continued.

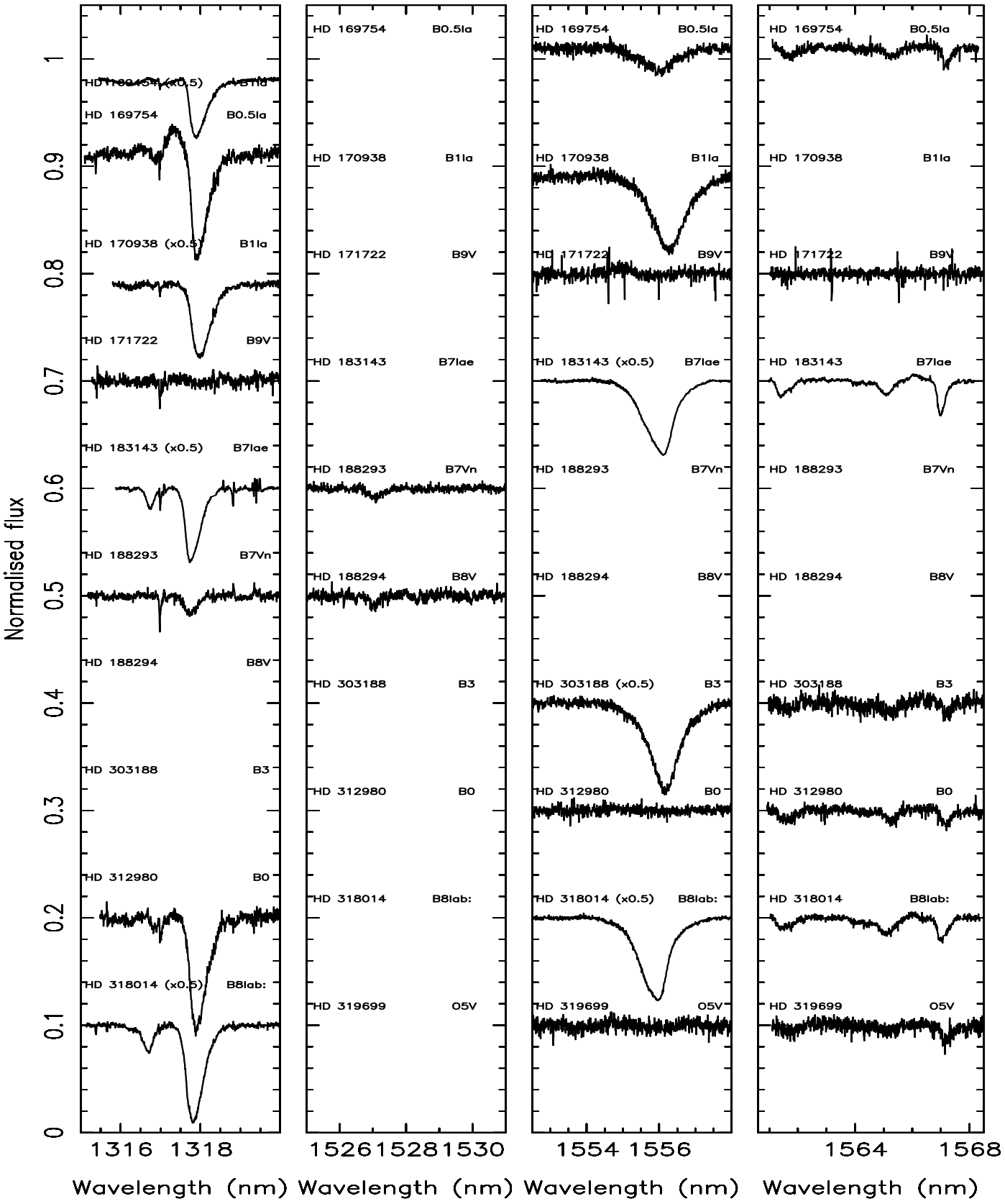

Fig. B1. continued.

Appendix C: Equivalent width measurements

Table C.1. Equivalent width values for the NIR DIBs studied in this paper as well as the optical DIBs at 5780 and 5797 Å. Columns with no entries either had no data taken or were affected by stellar lines or severe telluric absorption.

HD number	EW (1318 nm) (mÅ)	EW (1527 nm) (mÅ)	EW (1561 nm) (mÅ)	EW (1565 nm) (mÅ)	EW (1567 nm) (mÅ)	EW (578.0 nm) (mÅ)	EW (579.7 nm) (mÅ)
13989	<	<	...	...	...	...	...
35912	...	...	55	<	<	...	...
36408	170	55	<	<	<	...	...
36861	...	<	...	...	...	48	16
36862	...	...	...	...	...	34	17
36959	...	<	<	<	<	<	8.2
36960	<	<	<	<	<	15.0	5.6
52266	170	...	...	...	...	...	...
88661	...	<	<	<	<	13.2	8.2
89587	...	<	...	<	<	...	...
90706	308	...	33	34	36	...	...
90772	...	...	...	...	...	222	...
92740	156	...	...	...	...	...	...
93130	250	...	22	...	20	237	46
93576	...	...	...	...	...	199	78
93632	258	...	19	...	16	266	48
94910	448	...		...	...	430	92
97707	191	...	24	25	29	...	...
100841	<	...	<	<	<	...	...
101065		...		...	...	...	...
105056	202	...	23	15	28	...	...
105071	312	...	24	15	37	...	...
106068	265	...	32	17	35	235	47
111774	<	...	...	...	...	...	<
112272	363	...	38	...	...	441	143
113904	144	...	8	11	35	126	24
114213	370	...	...	...	...	...	...
115088	<	...	...	...	...	13.8	0.0
115363	331	...	34	20	38	...	...
115842	81	...	21	17	22	234	108
116119	471	...	...	...	...	449	125
125007	<	...	...	...	...	18	<<
125241	514	...	...	...	...	533	109
137753	78	...	...	...	...	...	...
138014	869	...	...	...	...	...	...
139892	<	...	...	...	...	...	...
141850	...	...	...	...	...	...	...
142468	590	...	32	38	72	461	118
144217	226	86	...	...	23	156	16
144218	245	100	...	...	...	157	20
144969	458	...	...	29	51	...	...
145482	39	...	...	...	...	...	...
145501	244	130	...	...	...	182	32

Table C.1. continued.

HD number	EW (1318 nm) (mÅ)	EW (1527 nm) (mÅ)	EW (1561 nm) (mÅ)	EW (1565 nm) (mÅ)	EW (1567 nm) (mÅ)	EW (578.0 nm) (mÅ)	EW (579.7 nm) (mÅ)
145501	244	130	...	...	...	182	32
145502	226	...	...	...	36	177	36
146331	281	...	...	...	...	...	...
147932	284	...	...	...	...	207	46
148184	126	...	...	...	...	100	53
148379	547	...	...	...	51	427	106
148688	318	...	38	...	36	...	...
148739	539	...	...	...	...	...	...
148937	602	310	50	...	52	356	71
151932	247	...	...	...	...	336	...
152235	406	...	30	...	48	418	101
152270	...	...	...	...	...	353	66
152386	378	...	31	...	55	352	70
154811	410	...	...	...	...	...	...
154873	385	160	...	...	...	...	...
156134	284	...	31	31	33	320	93
156201	306	...	29	31	47	318	119
156212	322	...	37	37	60	375	133
156738	413	...	48	65	57	494	136
157038	560	...	...	...	39	447	124
157778	...	...	...	...	...	34	<
157779	<	<	<	<	...	...	...
159455	570	...	56	58	78	...	...
160065	611	...	56	42	65	...	...
161289	...	...	...	...	...	...	...
161291	543	...	38	33	72	...	...
162168	575	...	37	45	68	...	...
164438	321	...	25	41	35	391	123
164865	485	...	32	47	37	383	67
165319	375	...	26	29	62	533	191
166734	566	...	...	...	...	720	276
167264	123	...	12	11	26	...	...
167971	745	...	51	57	100	563	158
168607	878	...	75	75	100	859	280
168625	809	...	100	120	90	842	239
168987	902	...	67	100	110	752	146
169034	760	...	55	78	60	689	216
169454	528	...	24	47	53	482	177
169754	451	...	...	40	58	...	...
170938	774	...	...	40	55	476	145
171722	<	...	...	...	...	20	<
183143	629	...	69	65	110	807	230
188293	64	48	...	...	...	...	...
188294	37	...	...	...	...	...	...
303188	690	...	<	<	<	...	...
305529	...	...	...	...	...	211	49
312980	521	...	58	53	61	...	...
318014	998	...	58	93	100	675	168
319699	534	...	35	33	69	363	87
319702	542	...	34	44	50	521	129

Appendix D: Optical spectra

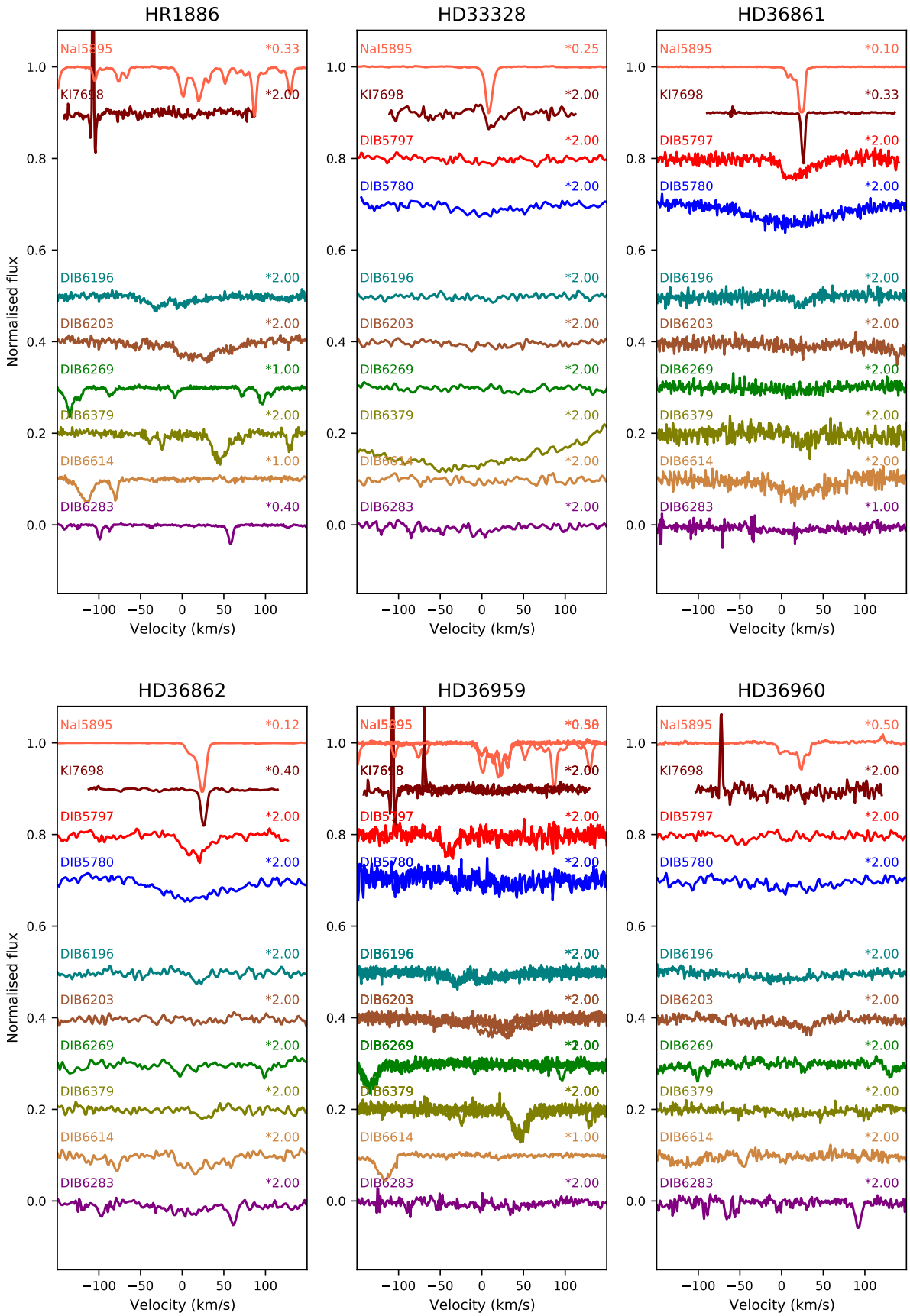

Fig. D.1. Normalised flux vs heliocentric velocity for Na I, K I, and a handful of DIBs. The flux is scaled by the factor shown and offset in the ordinate for clarity.

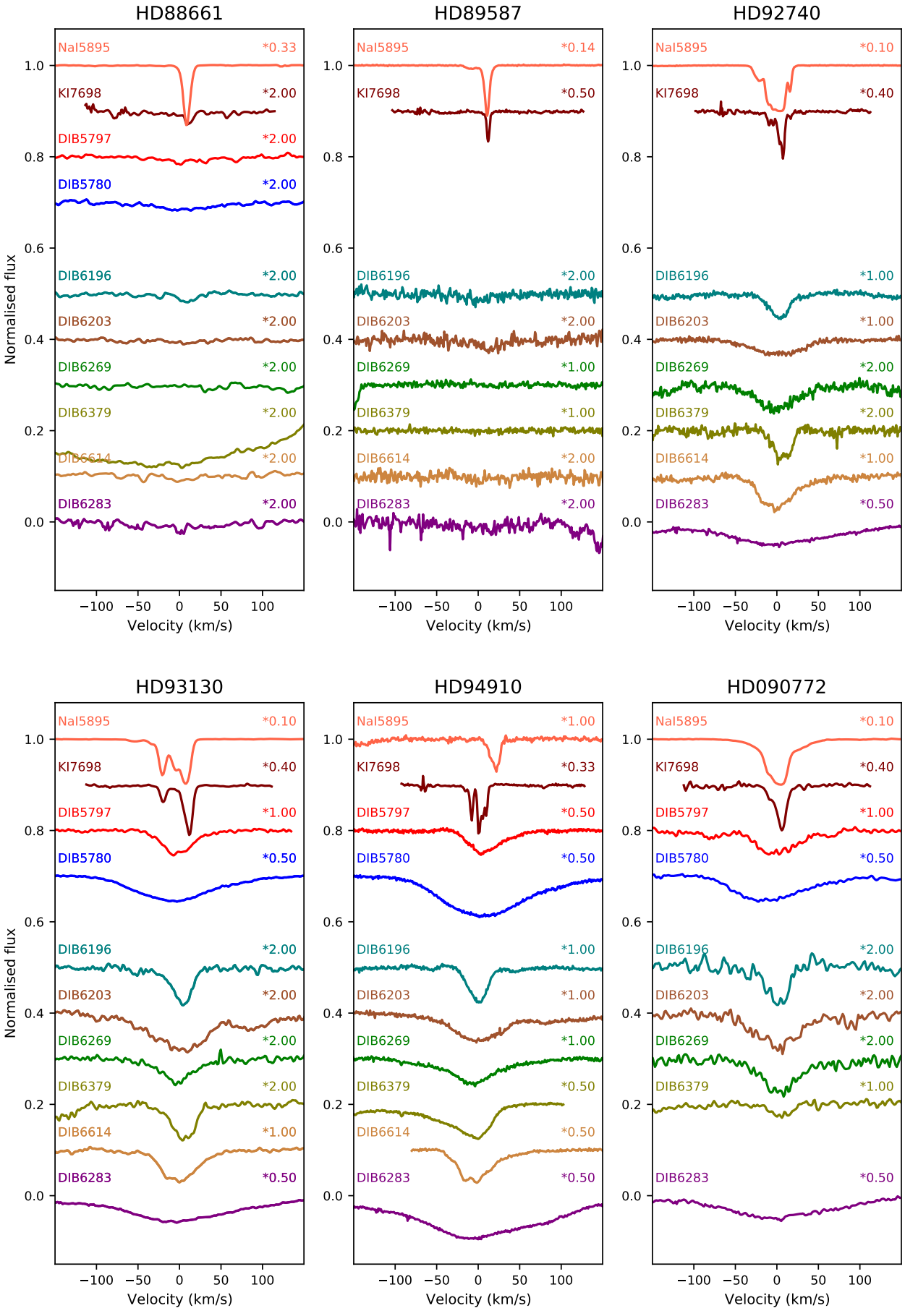

Fig. D.1. continued.

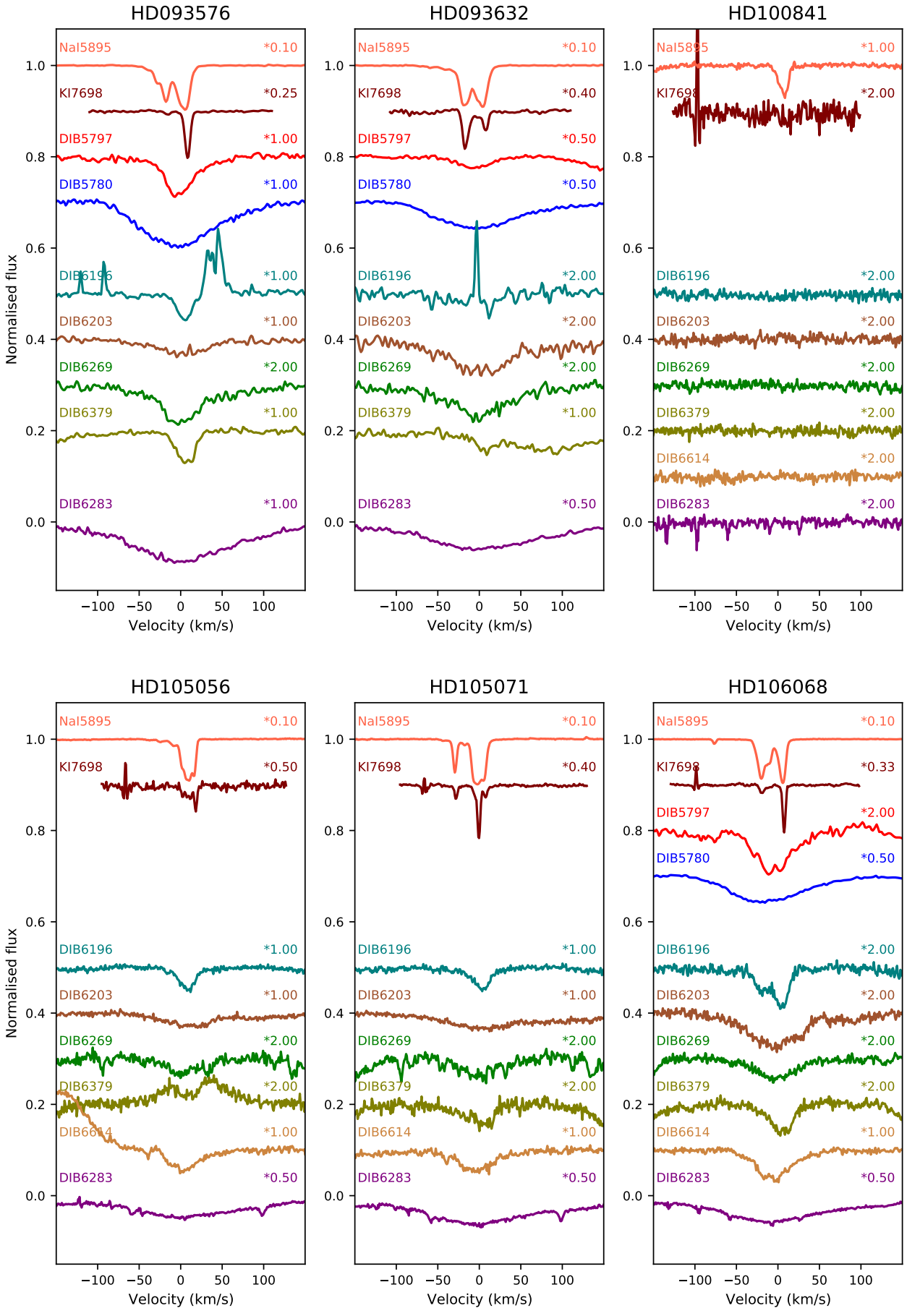

Fig. D.1. continued.

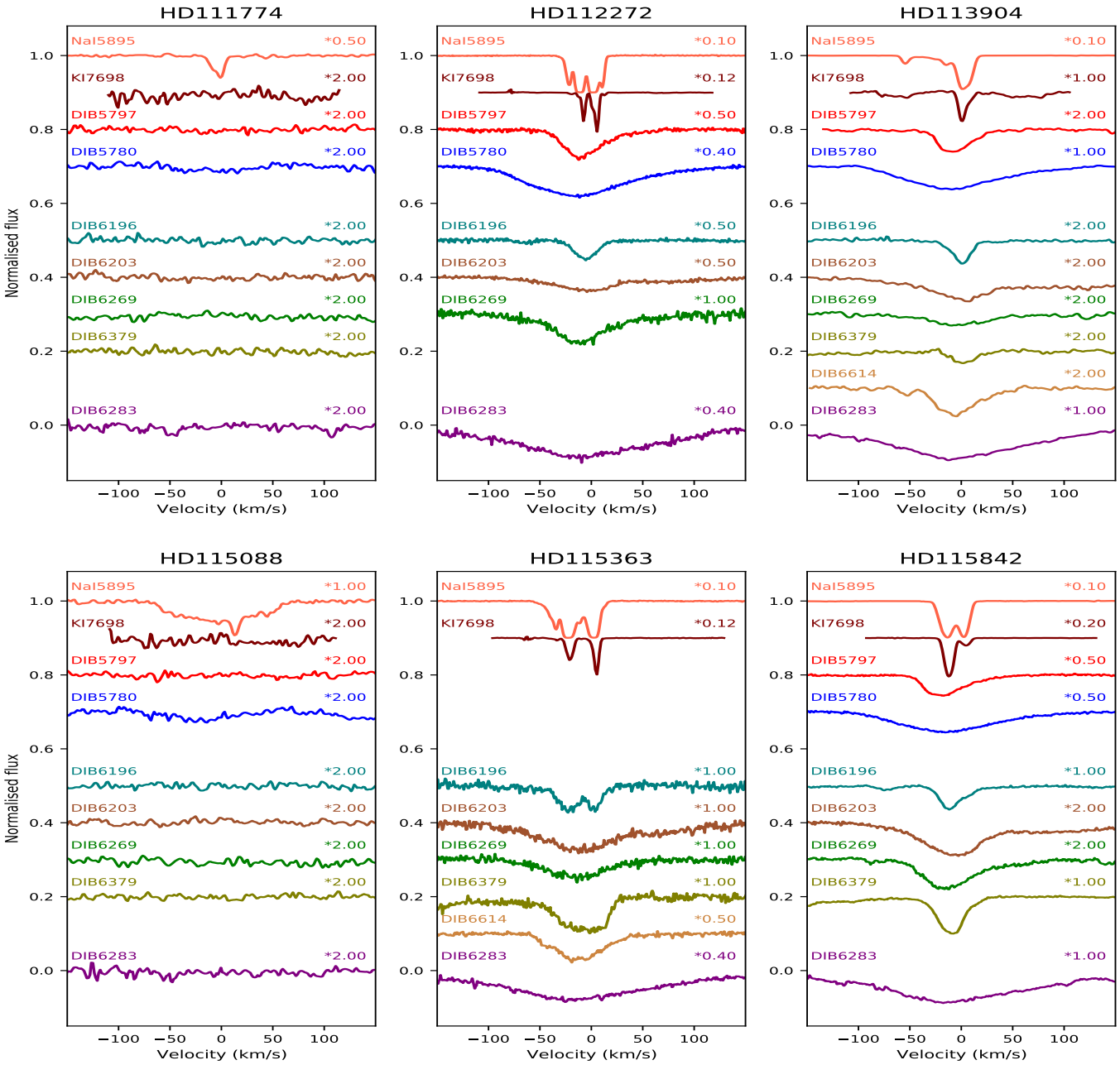

Fig. D.1. continued.

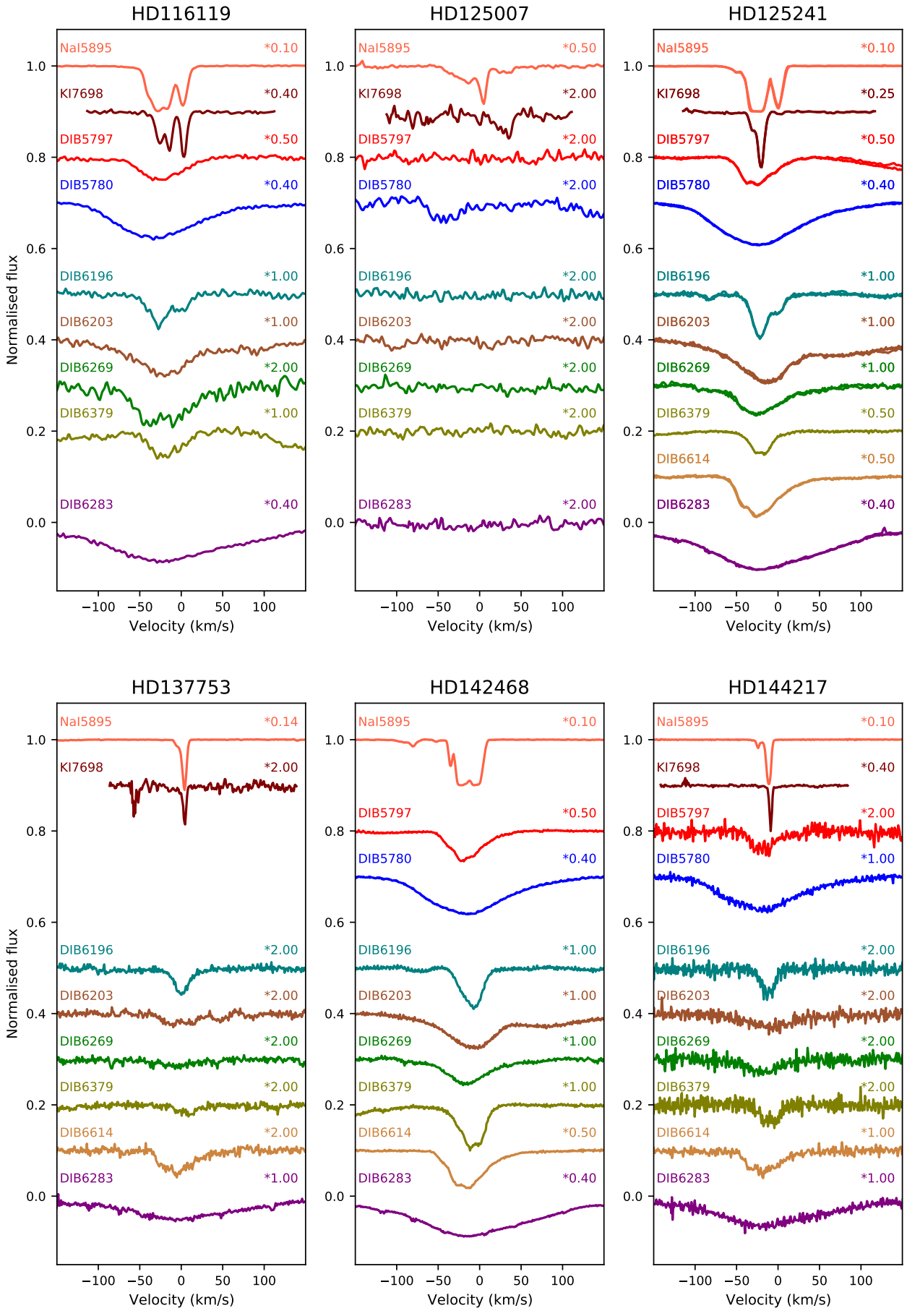

Fig. D.1. continued.

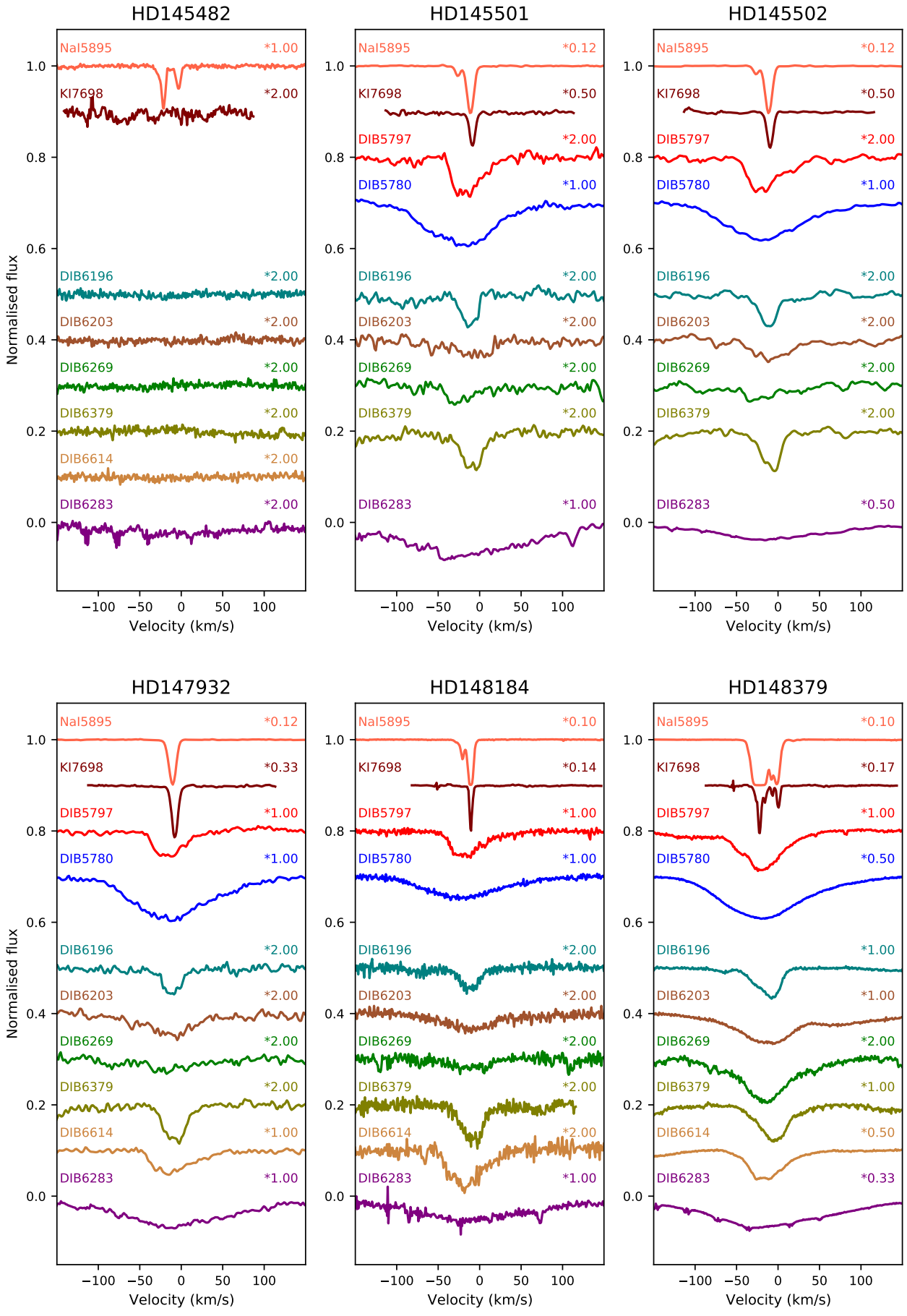

Fig. D.1. continued.

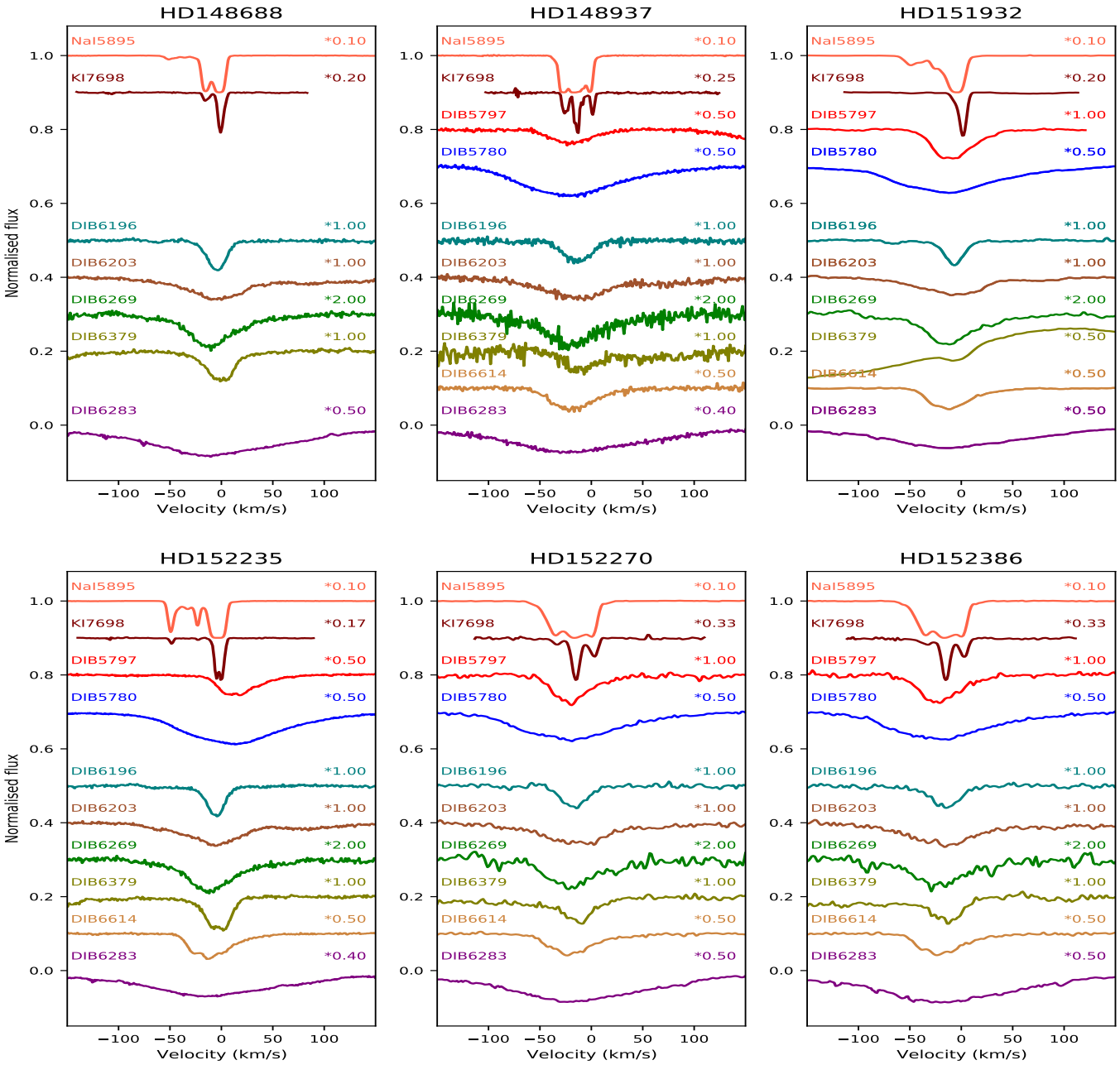

Fig. D.1. continued.

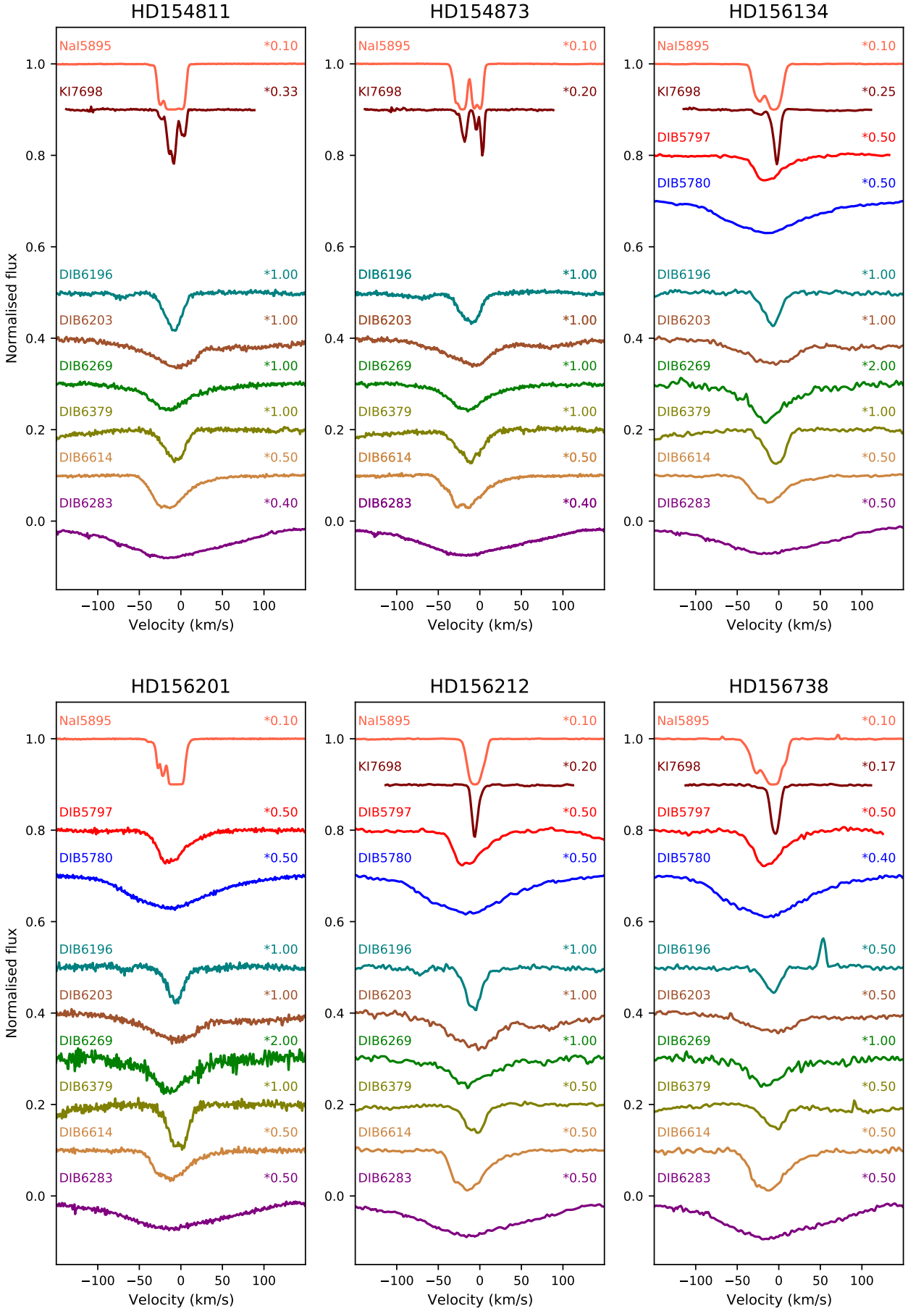

Fig. D.1. continued.

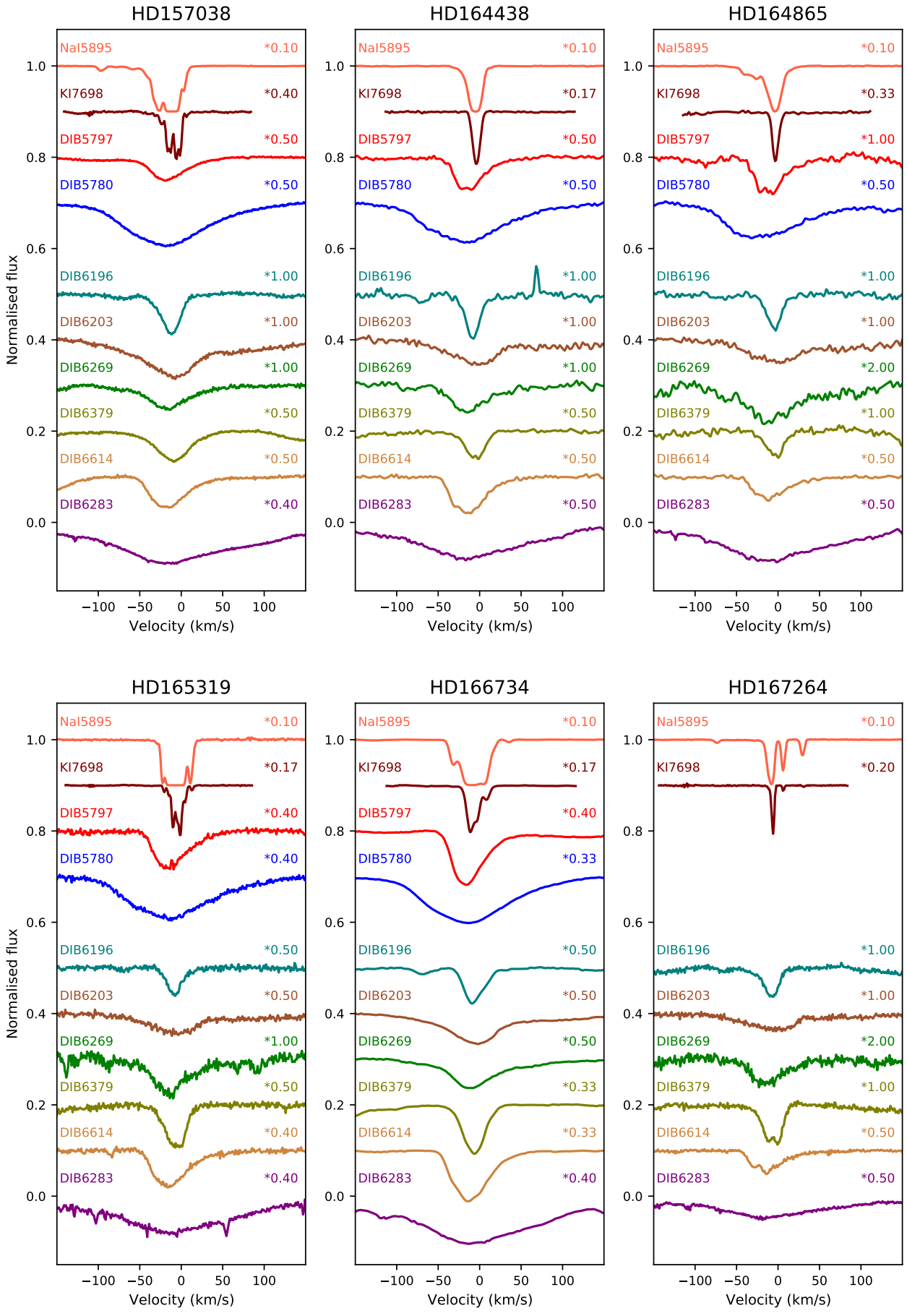

Fig. D.1. continued.

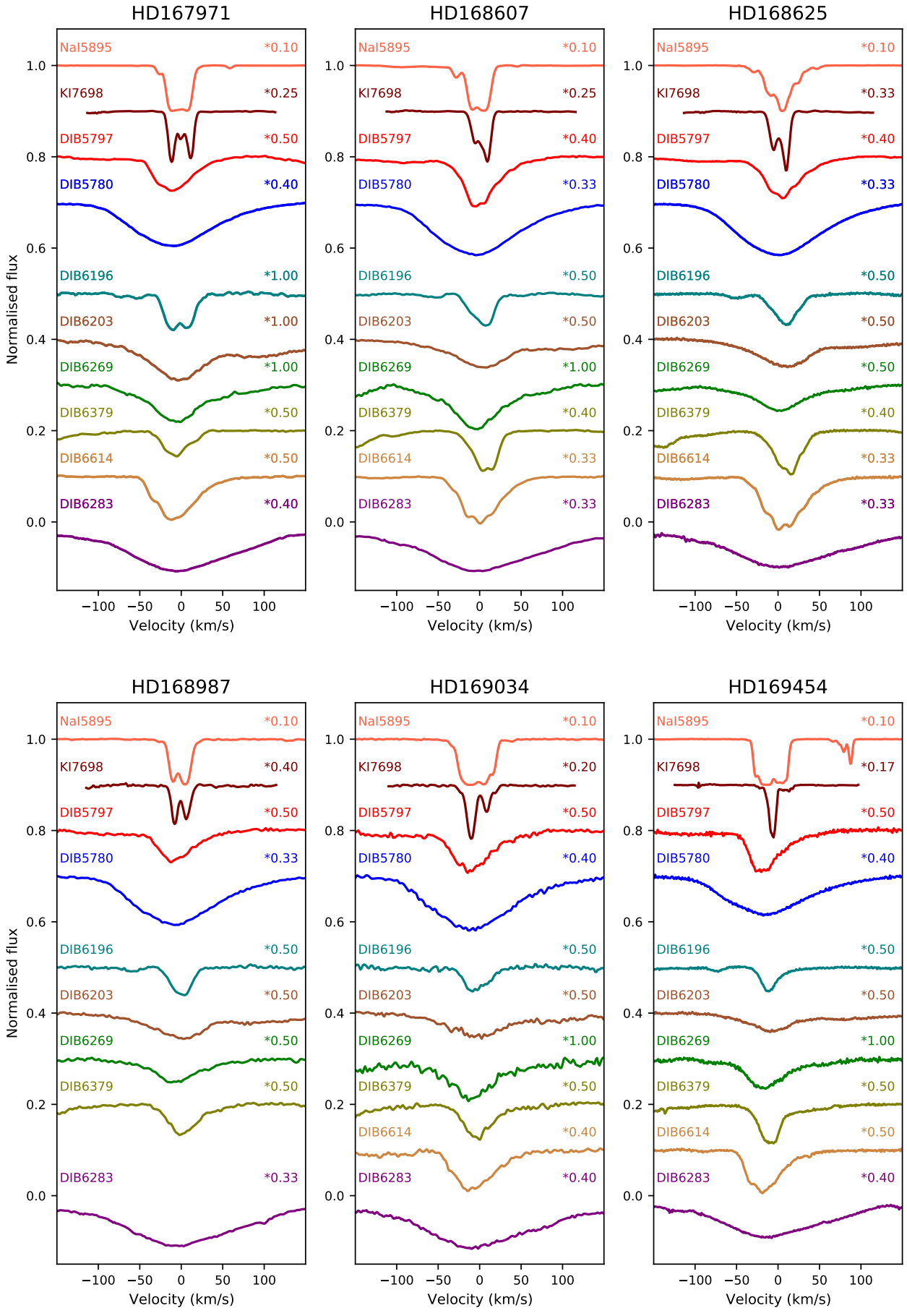

Fig. D.1. continued.

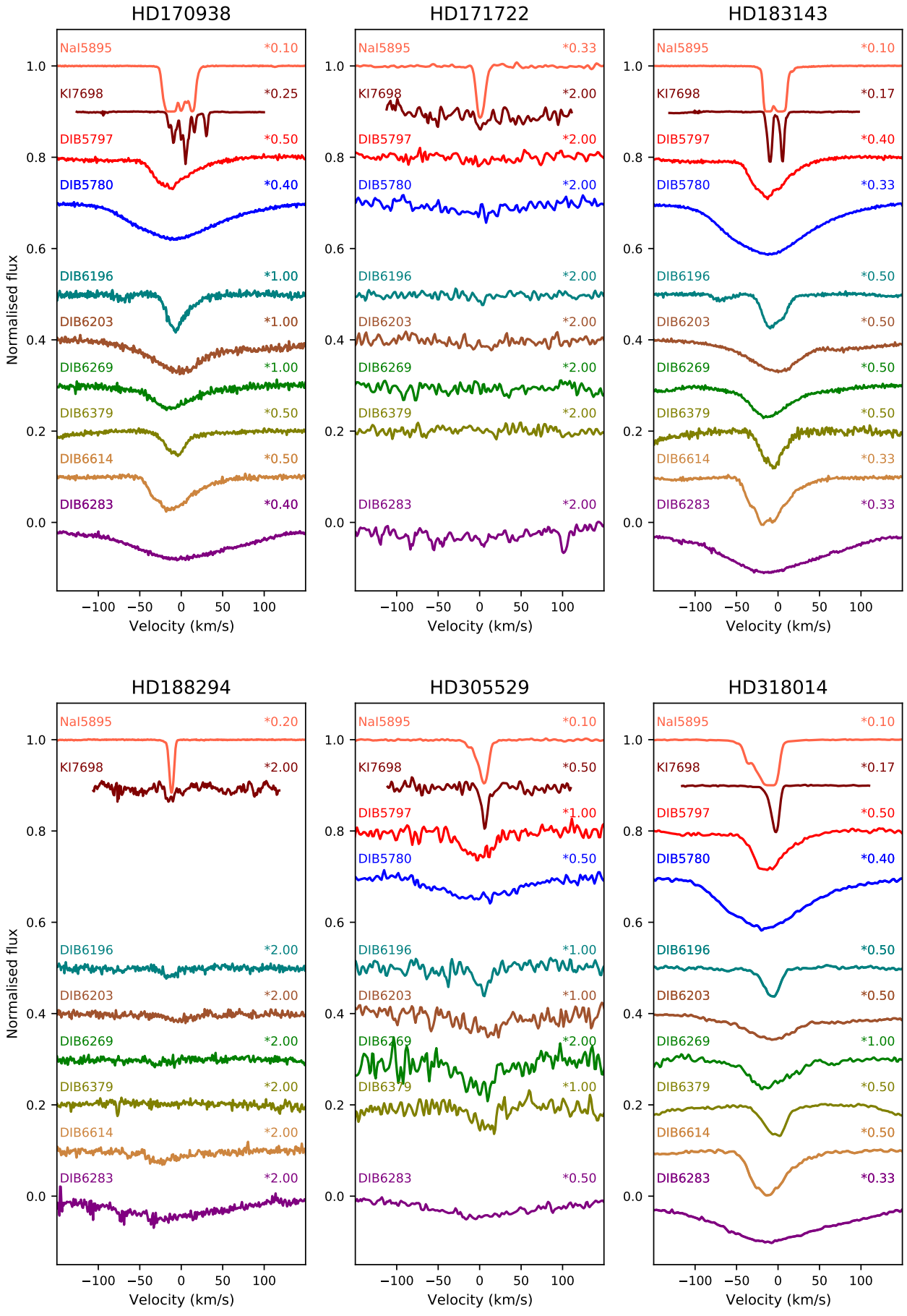

Fig. D.1. continued.

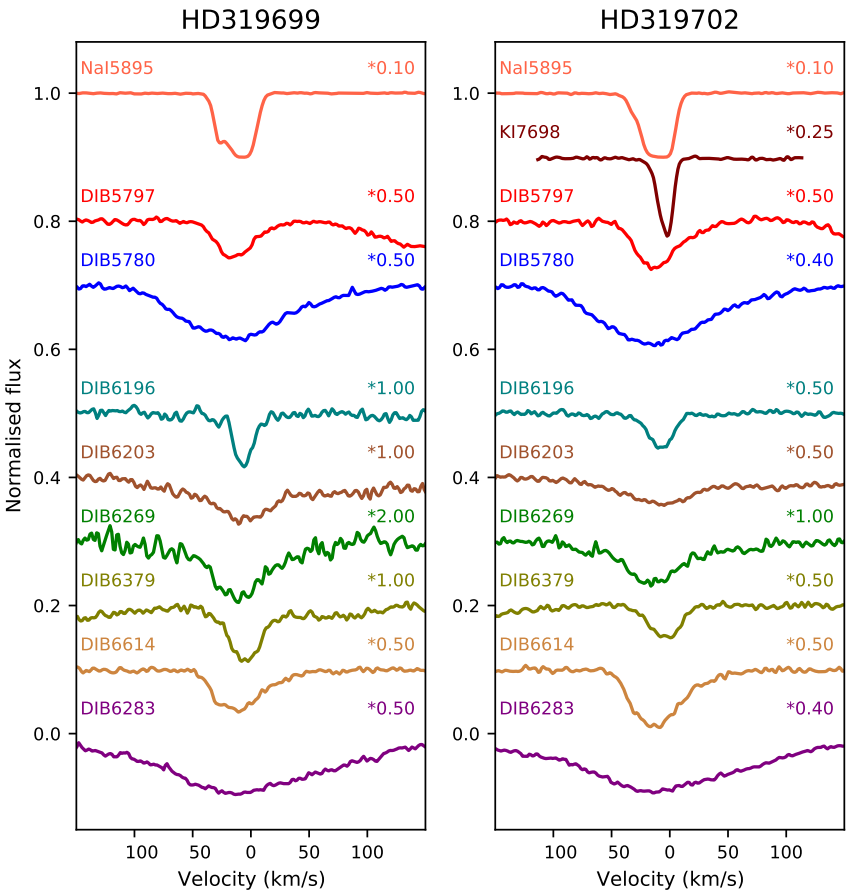

Fig. D.1. continued.

Appendix E: Equivalent width measurements

Table E.1. Equivalent width measurements for the optical and NIR features studied are only available in electronic form at the CDS via anonymous ftp to cdsarc.cds.unistra.fr (130.79.128.5) or via https://cdsarc.cds.unistra.fr/viz-bin/cat/J/A+A/672/A181

Appendix F: Correlations

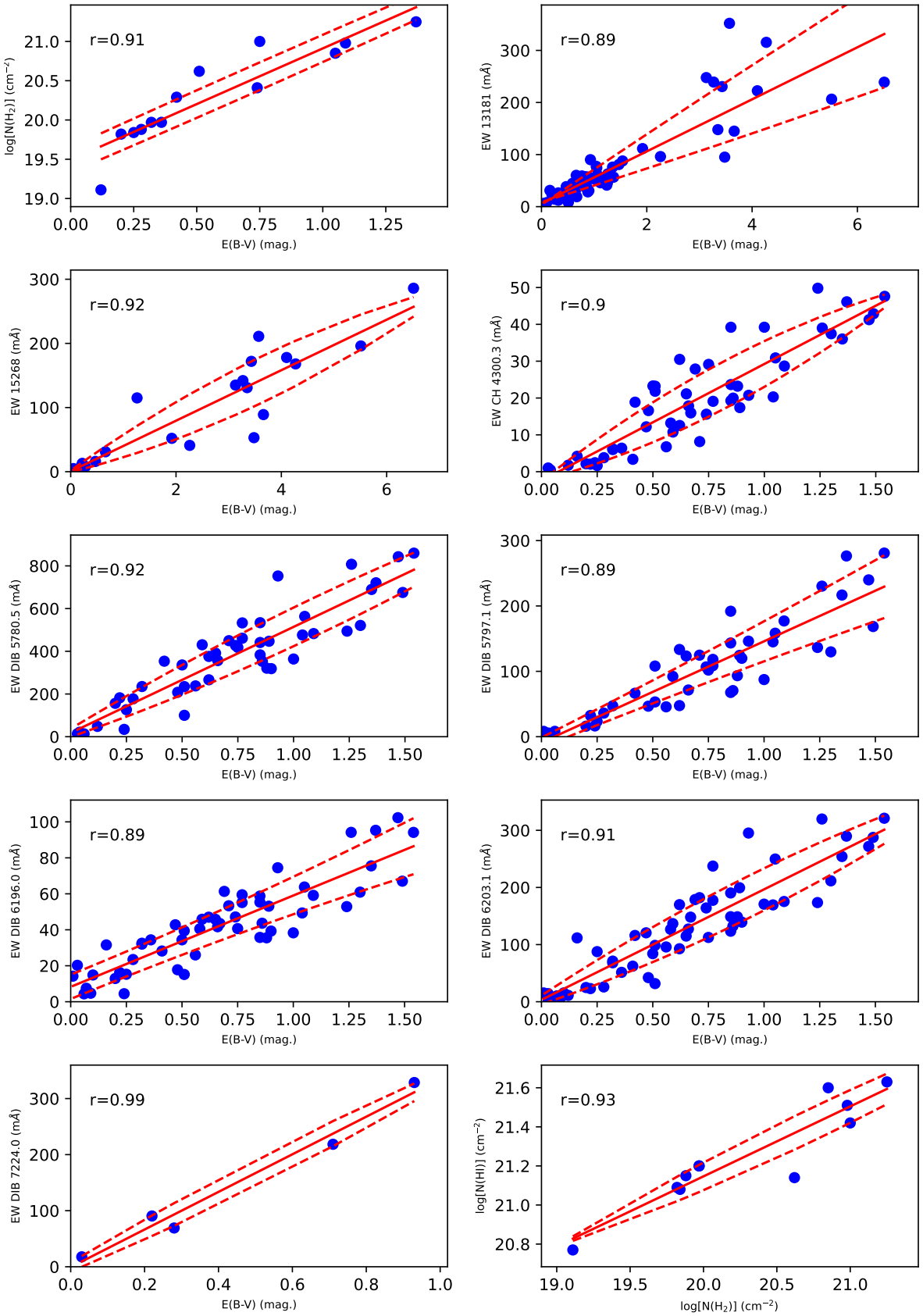

Fig. F.1. Correlations between EW of DIBs or reddening $E(B-V)$ for which the Pearson correlation coefficient exceeded 0.87, plus some optical lines. EW is measured in mÅ with reddening in magnitudes. The dashed lines show upper and lower error bounds obtained by fitting with a second order polynomial.

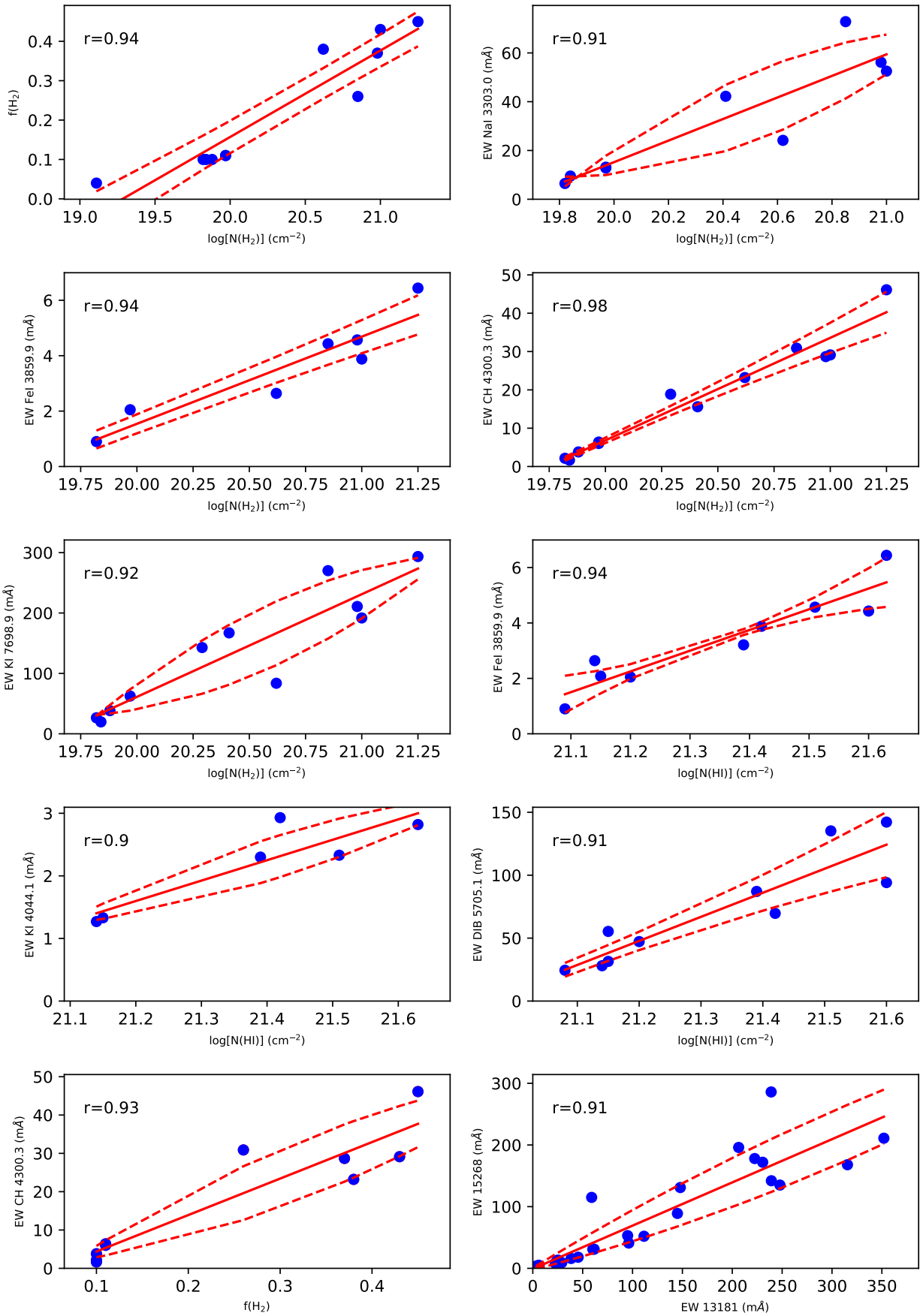

Fig. F.1. continued.

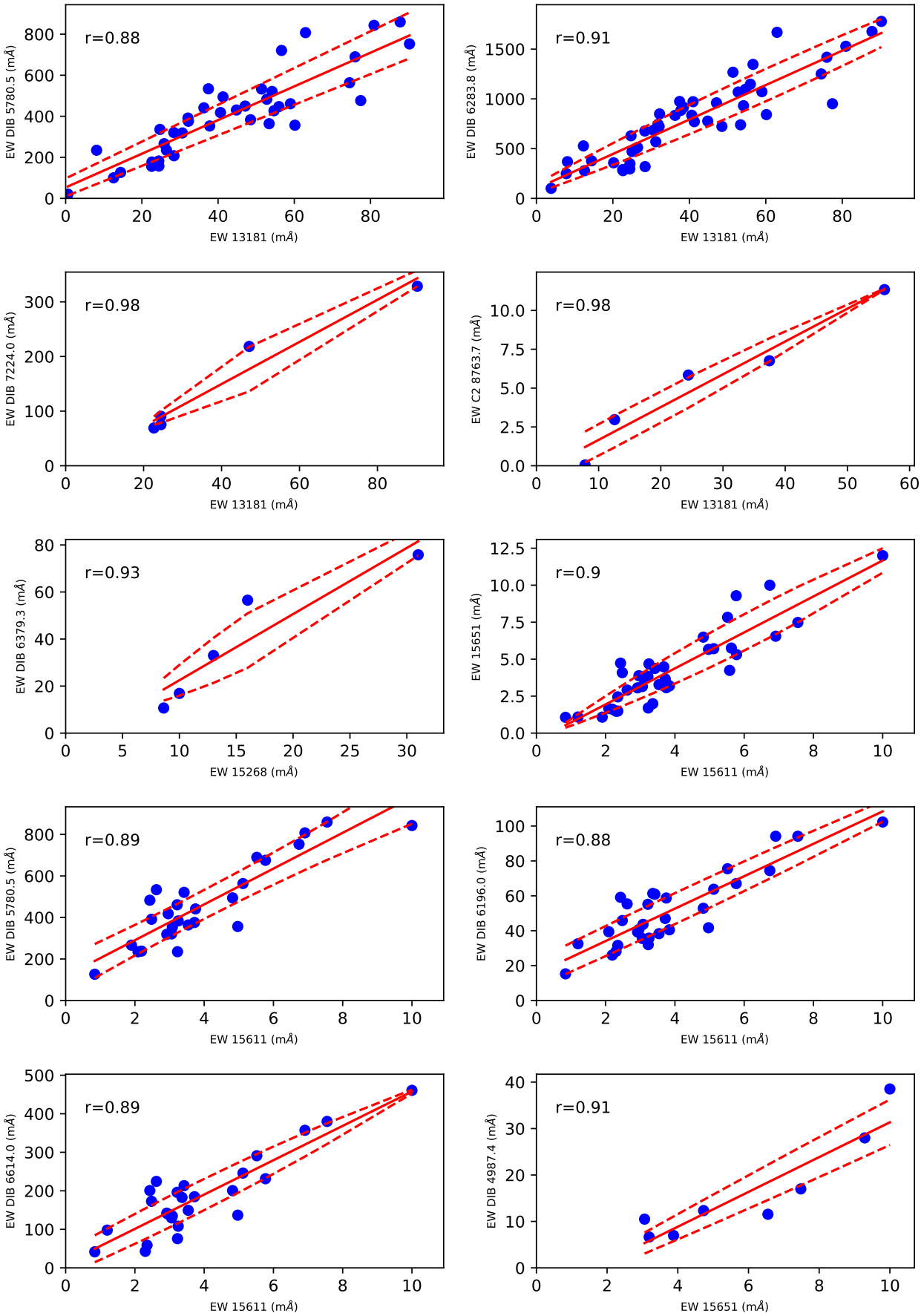

Fig. F.1. continued.

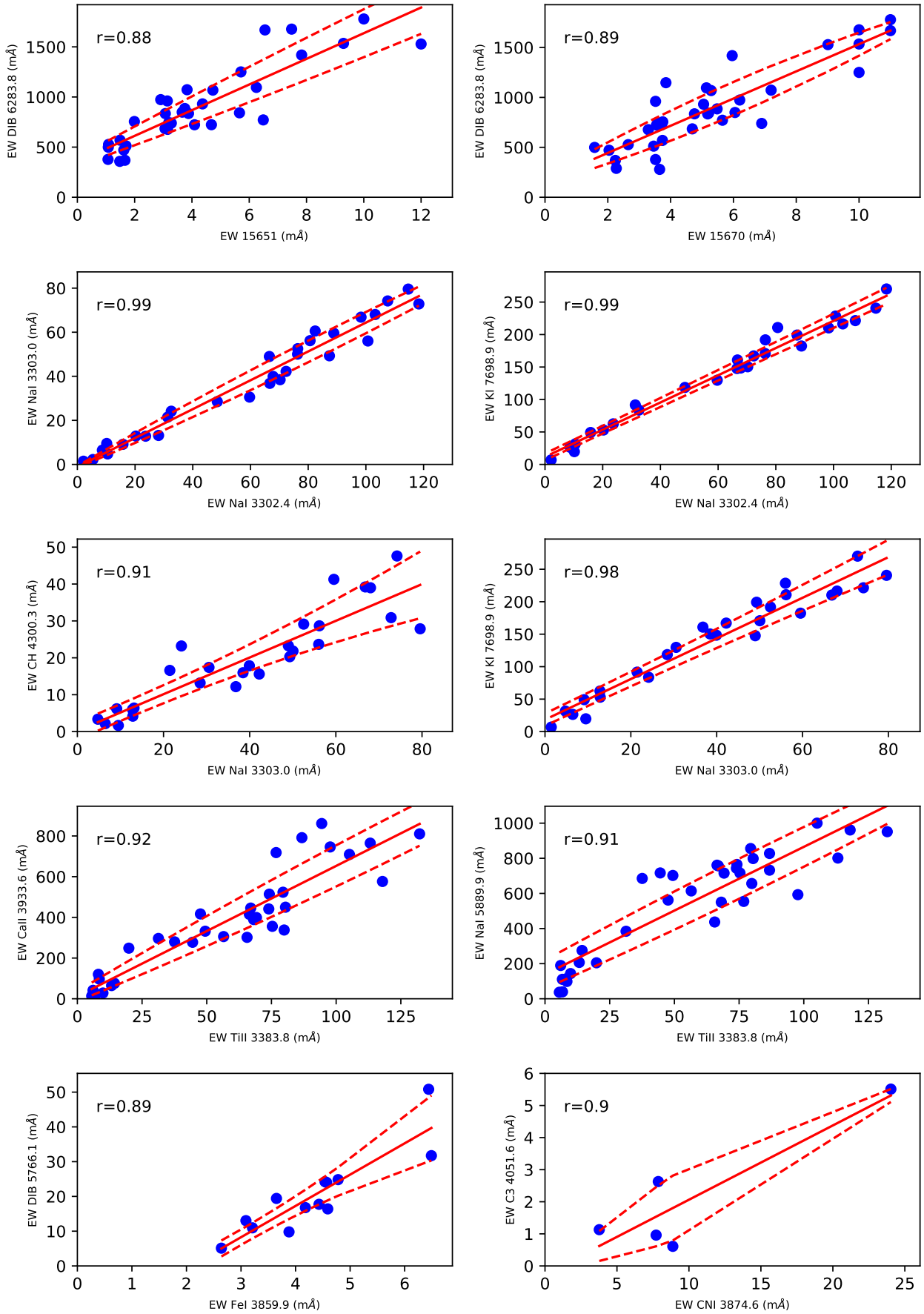

Fig. F.1. continued.

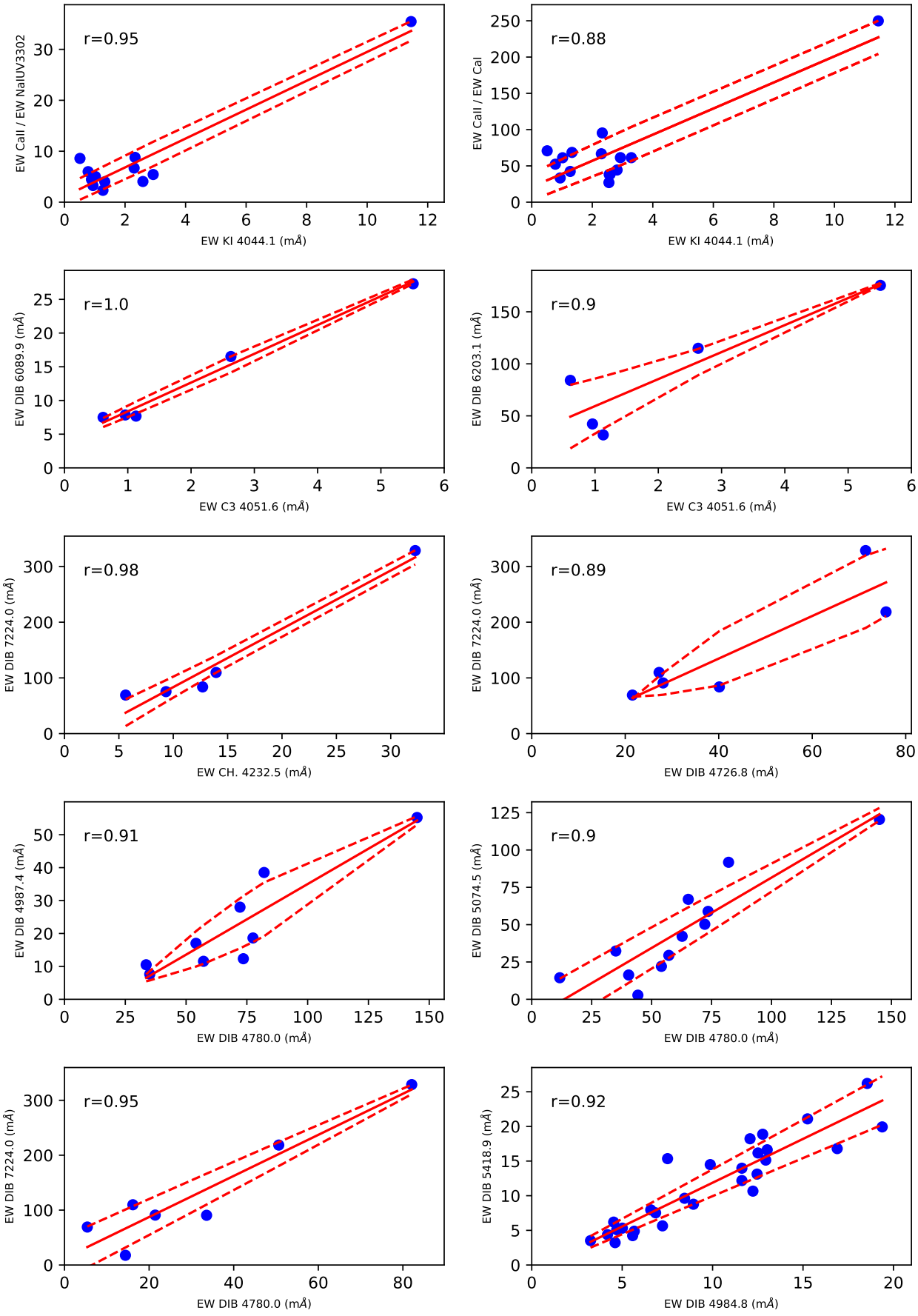

Fig. F.1. continued.

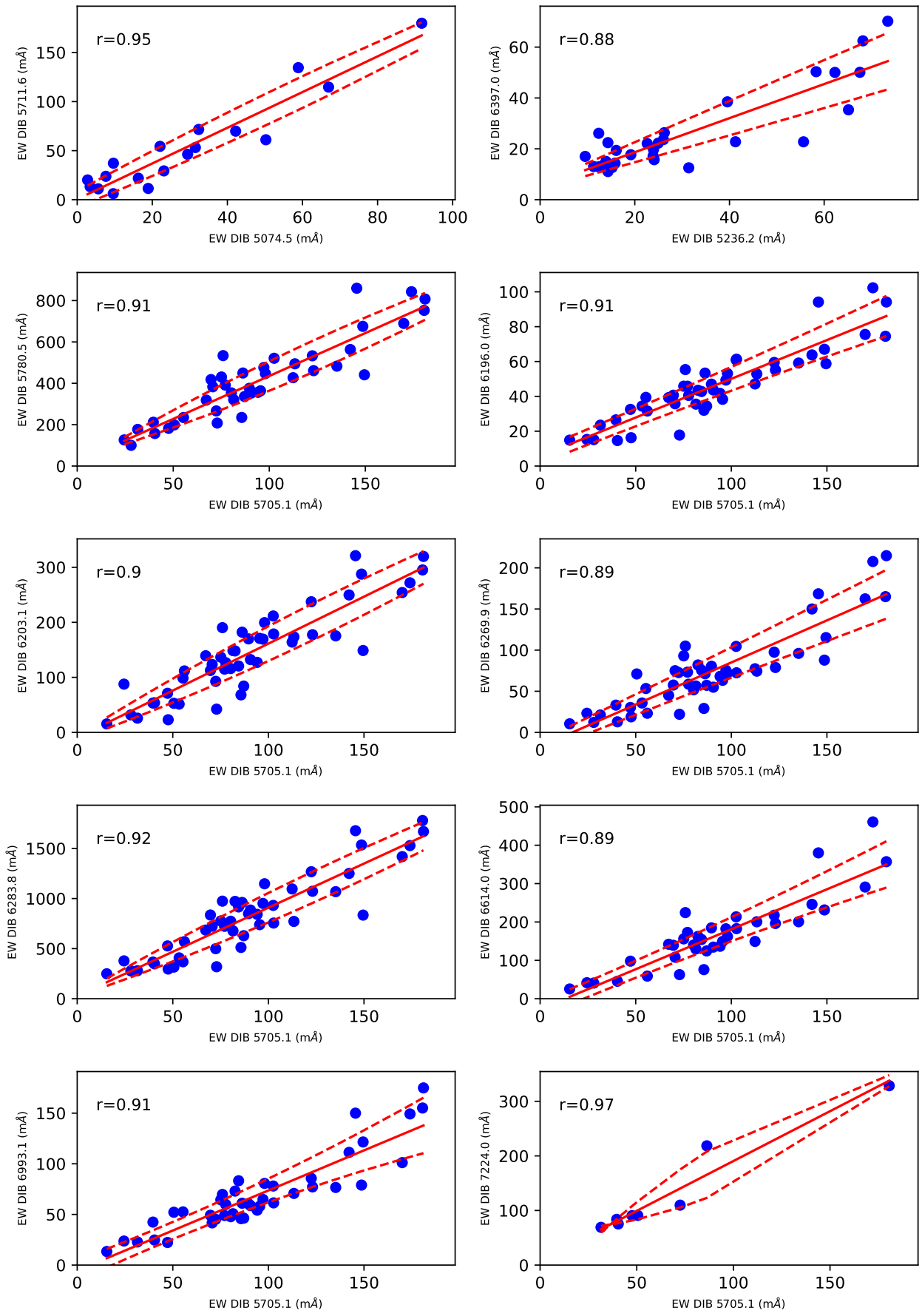

Fig. F.1. continued.

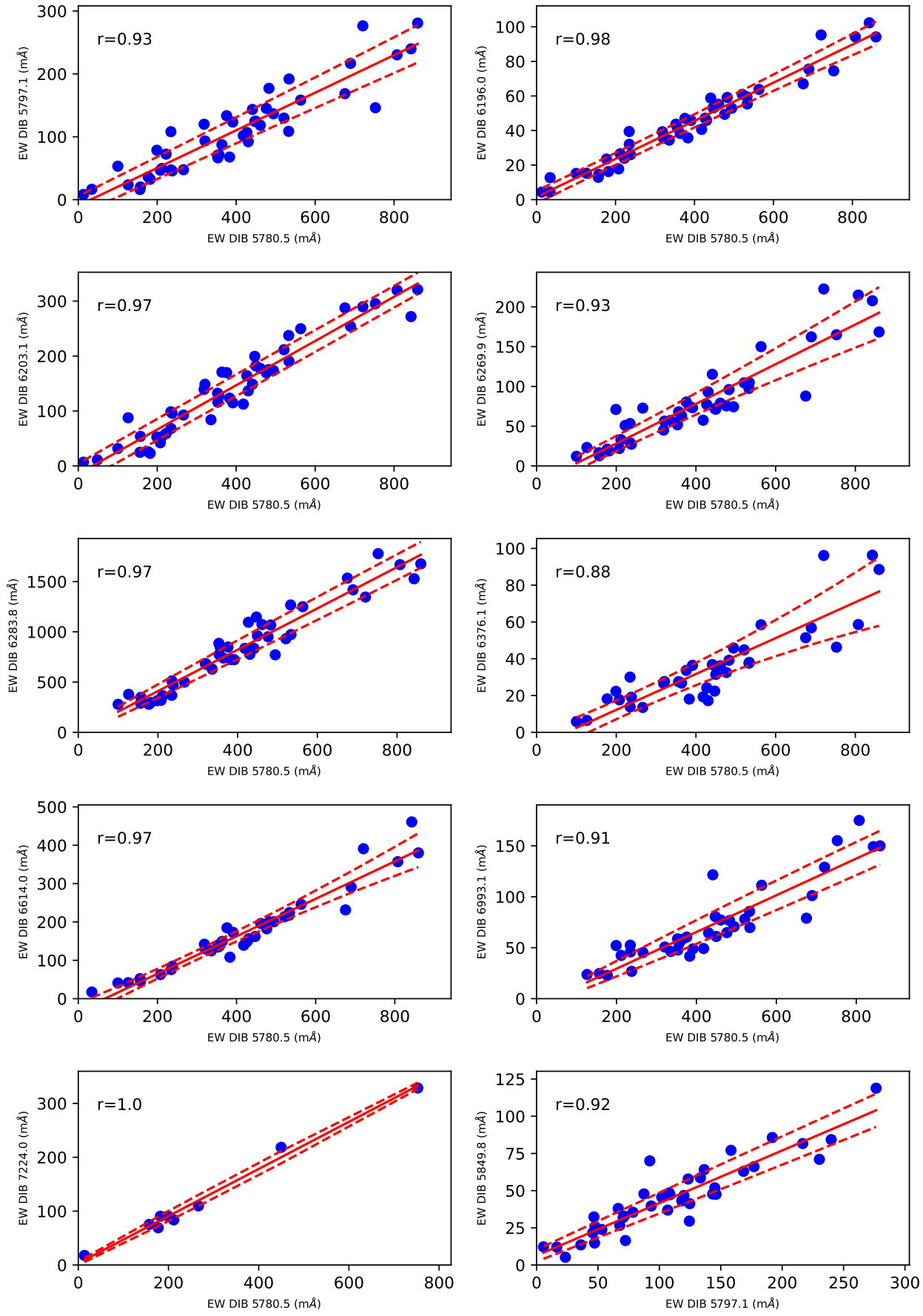

Fig. F.1. continued.

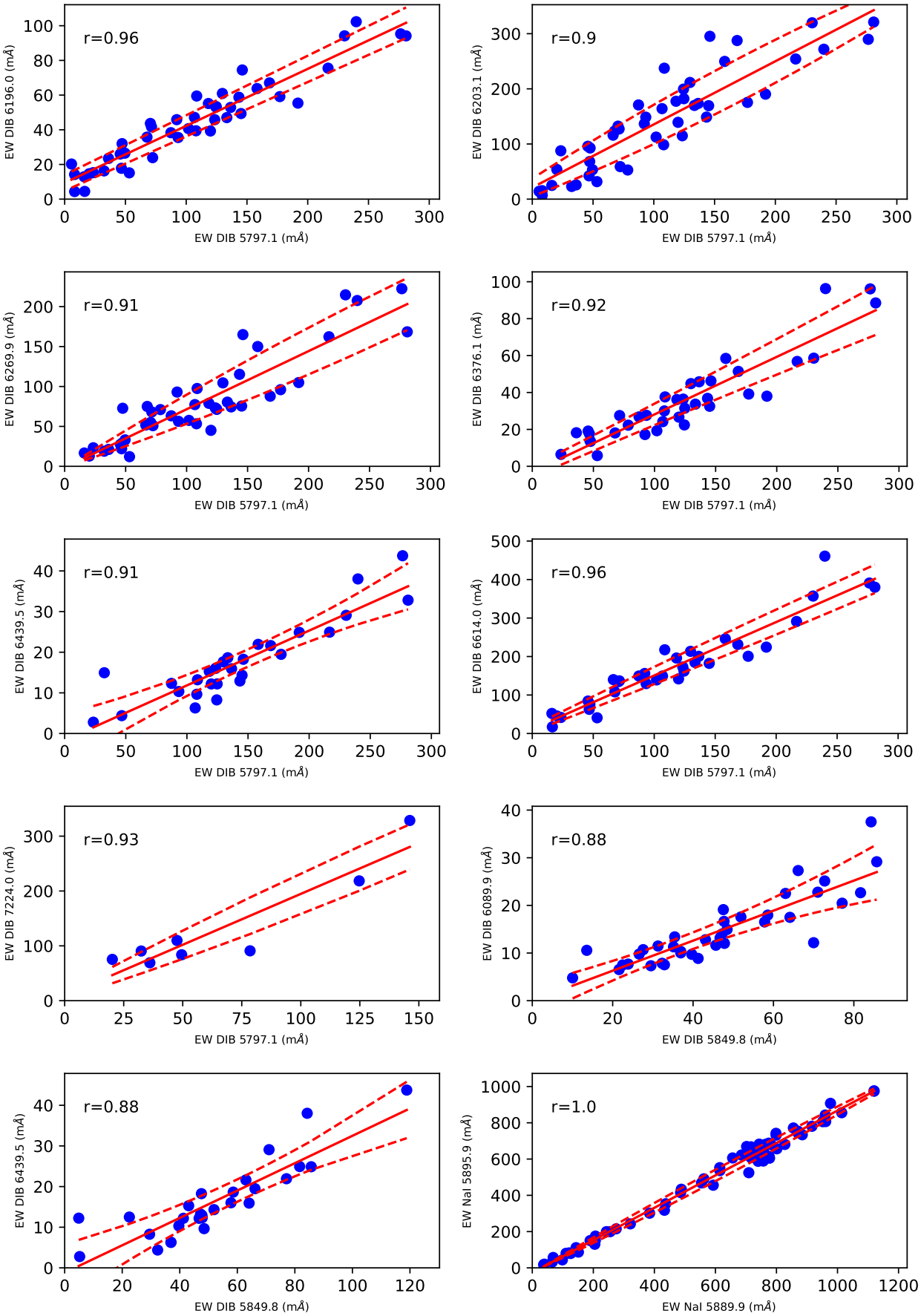

Fig. F.1. continued.

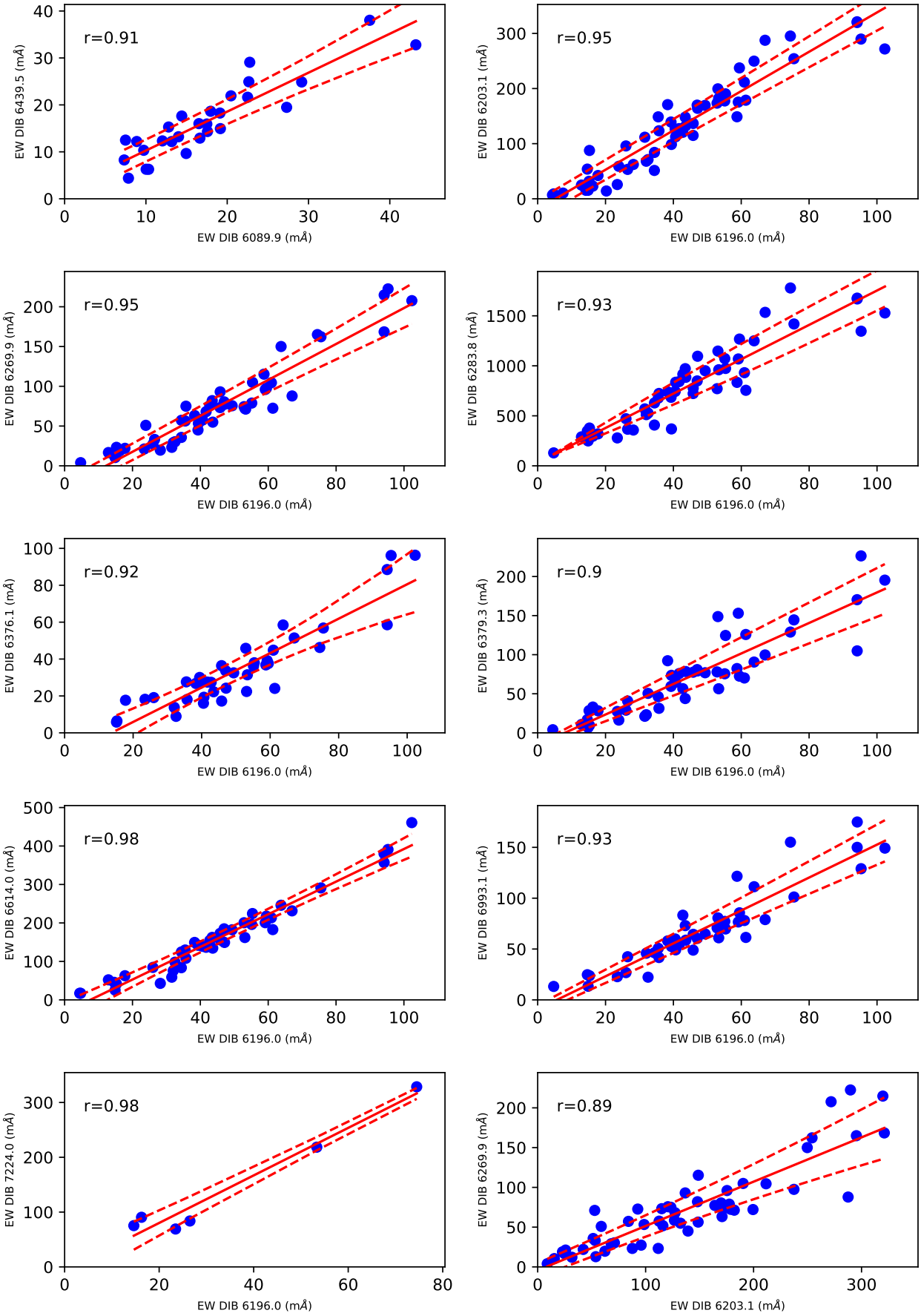

Fig. F.1. continued.

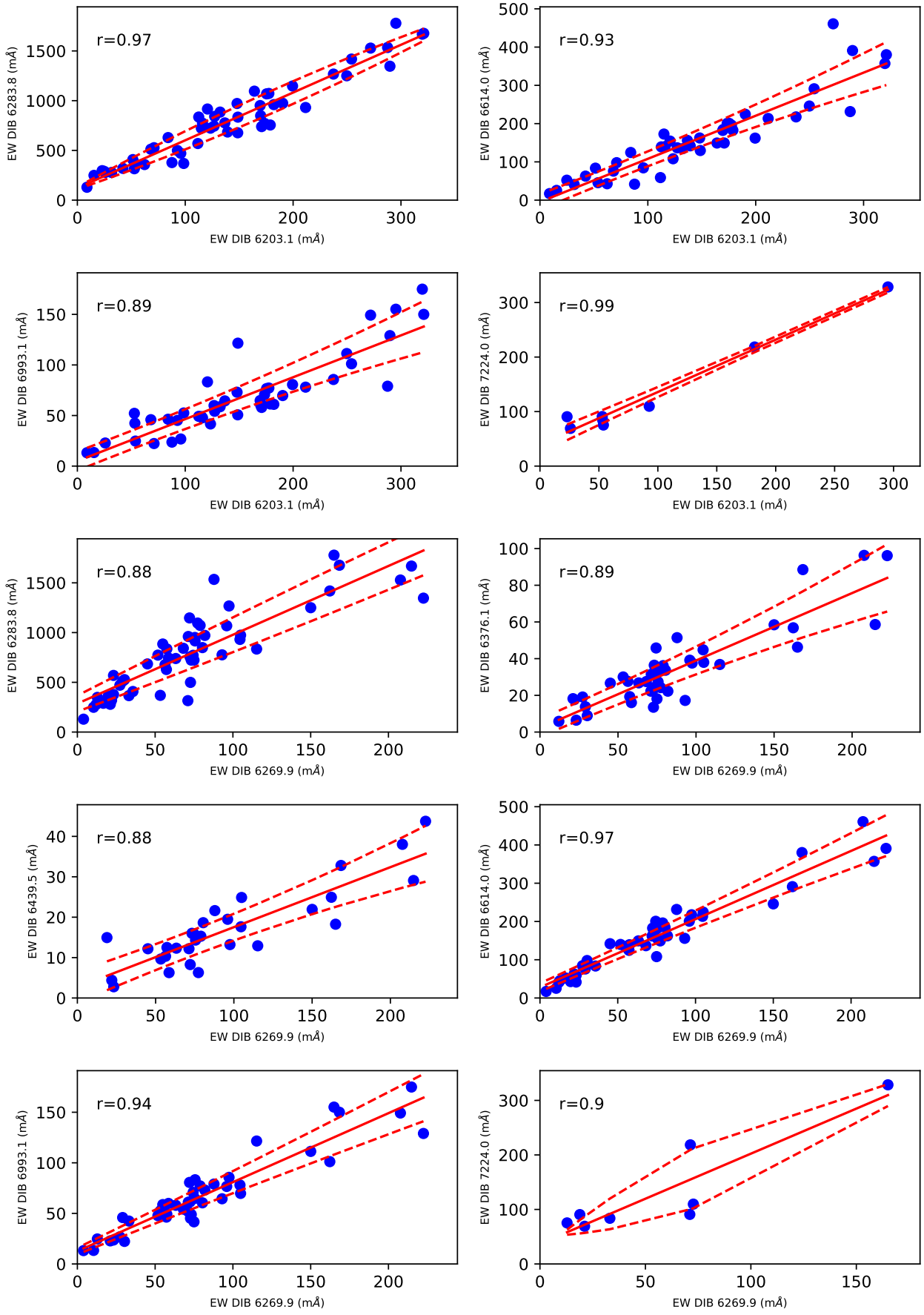

Fig. F.1. continued.

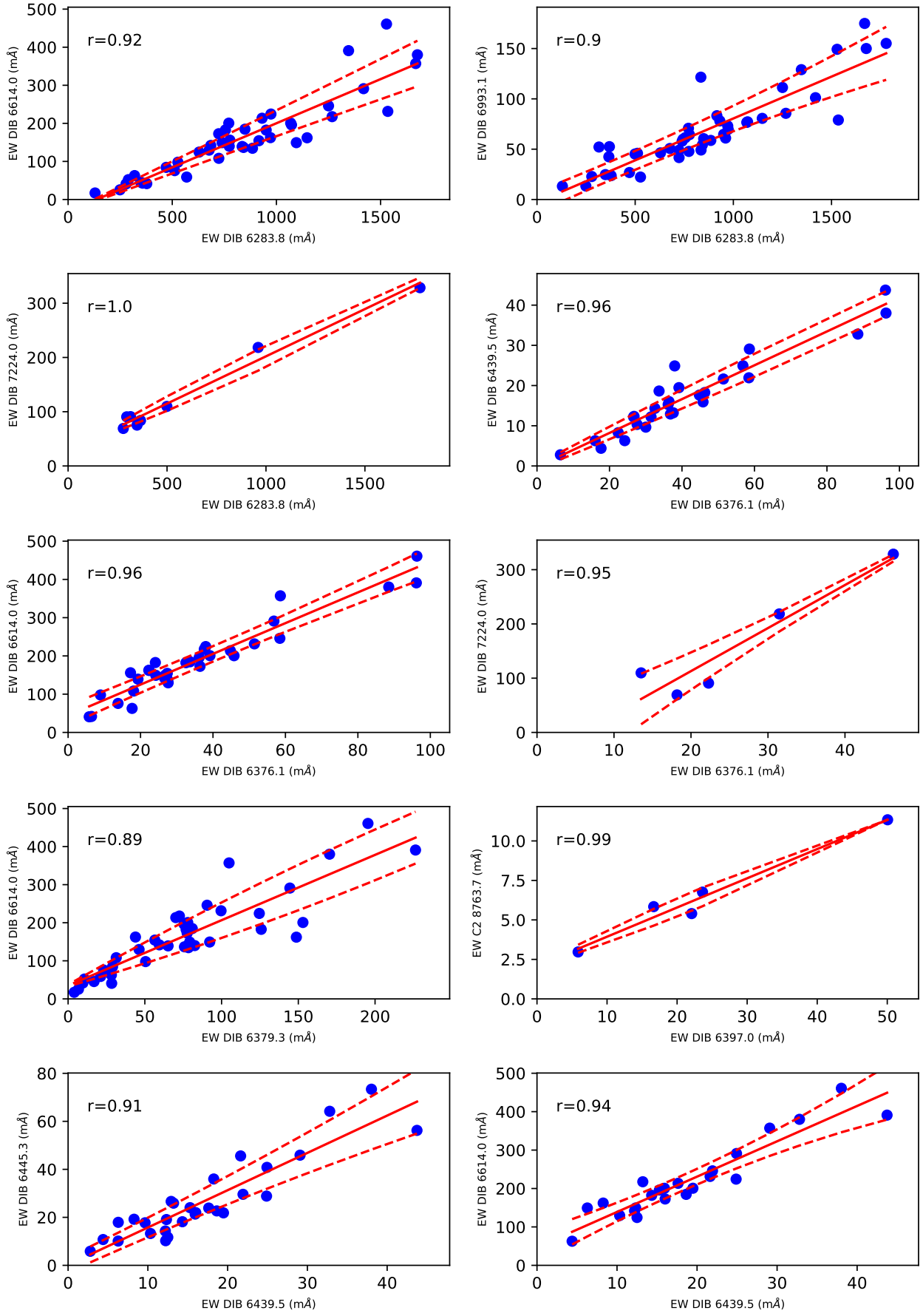

Fig. F.1. continued.

Appendix G: Correlation coefficients for the whole sample

Table G.1. Correlation coefficients. The number of sightlines used per correlation is shown in brackets. Both the standard Pearson correlation coefficient (top row per parameter) and 95 percent confidence range (second row) for the partial correlation coefficients are presented.

	E(B-V)	FeI (3859.9)	DIB (5074.5)	DIB (5418.9)	DIB (5705.1)	DIB (5711.6)	DIB) (5780.5)	DIB (5797.1)	DIB (5849.8)	DIB (6089.9)
E(B-V)		0.44 (17)	0.39 (20)	0.55 (32)	0.80 (45)	0.50 (27)	0.91 (47)	0.89 (44)	0.80 (48)	0.66 (40)
		0.06→0.83	-0.06→0.74	0.16→0.72	0.62→0.87	0.29→0.81	0.82→0.94	0.81→0.94	0.65→0.88	0.33→0.77
Na(3302.4)	0.84 (30)	-0.31 (23)	0.73 (13)	0.05 (26)	0.74 (26)	-0.01 (39)	0.79 (20)	-0.01 (37)	0.19 (24)	-0.01 (42)
	0.79→0.95	-0.64→0.16	-0.17→0.84	-0.33→0.48	-0.27→0.52	-0.38→0.28	-0.15→0.7	-0.31→0.37	-0.38→0.47	-0.27→0.36
FeI(3859.9)	0.44 (17)		0.73 (13)	0.05 (26)	0.30 (15)	-0.01 (39)	0.39 (16)	-0.01 (37)	0.19 (24)	-0.01 (42)
	0.06→0.83		-0.17→0.84	-0.33→0.48	-0.13→0.8	-0.38→0.28	-0.11→0.79	-0.31→0.37	-0.38→0.47	-0.27→0.36
CaII(3933.6)	0.66 (59)	0.23 (16)	0.73 (13)	0.05 (26)	0.45 (45)	-0.01 (39)	0.61 (47)	-0.01 (37)	0.19 (24)	-0.01 (42)
	0.55→0.82	-0.58→0.48	-0.17→0.84	-0.33→0.48	-0.24→0.38	-0.38→0.28	-0.04→0.53	-0.31→0.37	-0.38→0.47	-0.27→0.36
CaI(4226.7)	0.57 (44)	0.49 (15)	0.73 (13)	0.05 (26)	0.47 (39)	-0.01 (39)	0.55 (37)	-0.01 (37)	0.19 (24)	-0.01 (42)
	0.41→0.79	-0.42→0.66	-0.17→0.84	-0.33→0.48	-0.05→0.56	-0.38→0.28	-0.07→0.56	-0.31→0.37	-0.38→0.47	-0.27→0.36
CH+(4232.5)	0.84 (49)	-0.43 (45)	0.73 (13)	0.05 (26)	0.75 (43)	-0.01 (39)	0.81 (39)	-0.01 (37)	0.19 (24)	-0.01 (42)
	0.73→0.91	-0.72→-0.27	-0.17→0.84	-0.33→0.48	-0.11→0.5	-0.38→0.28	0.08→0.65	-0.31→0.37	-0.38→0.47	-0.27→0.36
CH(4300.3)	0.90 (51)	0.04 (41)	0.73 (13)	0.05 (26)	0.70 (44)	-0.01 (39)	0.78 (44)	-0.01 (37)	0.19 (24)	-0.01 (42)
	0.78→0.92	-0.23→0.4	-0.17→0.84	-0.33→0.48	-0.26→0.36	-0.38→0.28	-0.36→0.26	-0.31→0.37	-0.38→0.47	-0.27→0.36
DIB(4726.8)	0.81 (48)	0.01 (42)	0.73 (13)	0.05 (26)	0.62 (44)	-0.01 (39)	0.71 (43)	-0.01 (37)	0.19 (24)	-0.01 (42)
	0.67→0.89	-0.17→0.45	-0.17→0.84	-0.33→0.48	-0.21→0.41	-0.38→0.28	-0.28→0.35	-0.31→0.37	-0.38→0.47	-0.27→0.36
DIB(4984.8)	0.49 (36)	0.34 (29)	0.73 (13)	0.05 (26)	0.34 (33)	-0.01 (39)	0.25 (31)	-0.01 (37)	0.19 (24)	-0.01 (42)
	0.1→0.66	-0.26→0.48	-0.17→0.84	-0.33→0.48	-0.44→0.27	-0.38→0.28	-0.63→0.04	-0.31→0.37	-0.38→0.47	-0.27→0.36
DIB(5074.5)	0.39 (20)	0.73 (13)		0.05 (26)	0.53 (16)	-0.01 (39)	0.34 (17)	-0.01 (37)	0.19 (24)	-0.01 (42)
	-0.06→0.74	-0.17→0.84		-0.33→0.48	-0.13→0.83	-0.38→0.28	-0.22→0.77	-0.31→0.37	-0.38→0.47	-0.27→0.36
DIB(5418.9)	0.55 (32)	0.05 (26)	0.05 (26)		0.22 (30)	-0.01 (39)	0.31 (27)	-0.01 (37)	0.19 (24)	-0.01 (42)
	0.16→0.72	-0.33→0.48	-0.33→0.48		-0.59→0.11	-0.38→0.28	-0.62→0.11	-0.31→0.37	-0.38→0.47	-0.27→0.36
DIB(5705.1)	0.80 (45)	0.30 (15)	0.53 (16)	0.22 (30)		-0.01 (39)	0.91 (41)	-0.01 (37)	0.19 (24)	-0.01 (42)
	0.62→0.87	-0.13→0.8	-0.13→0.83	-0.59→0.11		-0.38→0.28	0.34→0.78	-0.31→0.37	-0.38→0.47	-0.27→0.36
DIB(5711.6)	0.50 (27)	-0.01 (39)	-0.01 (39)	-0.01 (39)	-0.01 (39)		0.50 (21)	-0.01 (37)	0.19 (24)	-0.01 (42)
	0.29→0.81	-0.38→0.28	-0.38→0.28	-0.38→0.28	-0.38→0.28		-0.21→0.68	-0.31→0.37	-0.38→0.47	-0.27→0.36
DIB(5780.5)	0.91 (47)	0.39 (16)	0.34 (17)	0.31 (27)	0.91 (41)	0.50 (21)		-0.01 (37)	0.19 (24)	-0.01 (42)
	0.82→0.94	-0.11→0.79	-0.22→0.77	-0.62→0.11	0.34→0.78	-0.21→0.68		-0.31→0.37	-0.38→0.47	-0.27→0.36
DIB(5797.1)	0.89 (44)	-0.01 (37)	-0.01 (37)	-0.01 (37)	-0.01 (37)	-0.01 (37)	-0.01 (37)		0.19 (24)	-0.01 (42)
	0.81→0.94	-0.31→0.37	-0.31→0.37	-0.31→0.37	-0.31→0.37	-0.31→0.37	-0.31→0.37		-0.38→0.47	-0.27→0.36
DIB(5849.8)	0.80 (48)	0.19 (24)	0.19 (24)	0.19 (24)	0.19 (24)	0.19 (24)	0.19 (24)	0.19 (24)		-0.01 (42)
	0.65→0.88	-0.38→0.47	-0.38→0.47	-0.38→0.47	-0.38→0.47	-0.38→0.47	-0.38→0.47	-0.38→0.47		-0.27→0.36
DIB(6089.9)	0.66 (40)	-0.01 (42)	-0.01 (42)	-0.01 (42)	-0.01 (42)	-0.01 (42)	-0.01 (42)	-0.01 (42)	-0.01 (42)	
	0.33→0.77	-0.27→0.36	-0.27→0.36	-0.27→0.36	-0.27→0.36	-0.27→0.36	-0.27→0.36	-0.27→0.36	-0.27→0.36	
DIB(6196.0)	0.88 (54)	0.39 (17)	0.37 (21)	0.35 (32)	0.91 (46)	0.53 (29)	0.98 (45)	0.95 (45)	0.83 (45)	0.75 (41)
	0.79→0.93	-0.25→0.71	-0.26→0.65	-0.46→0.25	0.49→0.82	0.02→0.7	0.81→0.94	0.61→0.87	0.36→0.76	0.22→0.71
DIB(6203.1)	0.91 (57)	-0.05 (44)	-0.05 (44)	-0.05 (44)	-0.05 (44)	-0.05 (44)	-0.05 (44)	-0.05 (44)	-0.05 (44)	-0.05 (44)
	0.87→0.95	-0.36→0.25	-0.36→0.25	-0.36→0.25	-0.36→0.25	-0.36→0.25	-0.36→0.25	-0.36→0.25	-0.36→0.25	-0.36→0.25
DIB(6269.9)	0.81 (51)	-0.15 (27)	-0.15 (27)	-0.15 (27)	-0.15 (27)	-0.15 (27)	-0.15 (27)	-0.15 (27)	-0.15 (27)	-0.15 (27)
	0.68→0.89	-0.56→0.2	-0.56→0.2	-0.56→0.2	-0.56→0.2	-0.56→0.2	-0.56→0.2	-0.56→0.2	-0.56→0.2	-0.56→0.2

Table G.1. continued.

	E(B-V)	FeI (3859.9)	DIB (5074.5)	DIB (5418.9)	DIB (5705.1)	DIB (5711.6)	DIB) (5780.5)	DIB (5797.1)	DIB (5849.8)	DIB (6089.9)
DIB(6283.8)	0.83 (51)	-0.10 (43)	-0.10 (43)	-0.10 (43)	-0.10 (43)	-0.10 (43)	-0.10 (43)	-0.10 (43)	-0.10 (43)	-0.10 (43)
	0.7→0.9	-0.38→0.24	-0.38→0.24	-0.38→0.24	-0.38→0.24	-0.38→0.24	-0.38→0.24	-0.38→0.24	-0.38→0.24	-0.38→0.24
DIB(6376.1)	0.84 (40)	-0.01 (42)	-0.01 (42)	-0.01 (42)	-0.01 (42)	-0.01 (42)	-0.01 (42)	-0.01 (42)	-0.01 (42)	-0.01 (42)
	0.66→0.9	-0.3→0.33	-0.3→0.33	-0.3→0.33	-0.3→0.33	-0.3→0.33	-0.3→0.33	-0.3→0.33	-0.3→0.33	-0.3→0.33
DIB(6439.5)	0.71 (30)	0.18 (37)	0.18 (37)	0.18 (37)	0.18 (37)	0.18 (37)	0.18 (37)	0.18 (37)	0.18 (37)	0.18 (37)
	0.46→0.86	-0.01→0.6	-0.01→0.6	-0.01→0.6	-0.01→0.6	-0.01→0.6	-0.01→0.6	-0.01→0.6	-0.01→0.6	-0.01→0.6
DIB(6614.0)	0.87 (44)	0.15 (27)	0.15 (27)	0.15 (27)	0.15 (27)	0.15 (27)	0.15 (27)	0.15 (27)	0.15 (27)	0.15 (27)
	0.74→0.92	-0.47→0.32	-0.47→0.32	-0.47→0.32	-0.47→0.32	-0.47→0.32	-0.47→0.32	-0.47→0.32	-0.47→0.32	-0.47→0.32
DIB(6993.1)	0.75 (41)	-0.22 (37)	-0.22 (37)	-0.22 (37)	-0.22 (37)	-0.22 (37)	-0.22 (37)	-0.22 (37)	-0.22 (37)	-0.22 (37)
	0.6→0.87	-0.53→0.1	-0.53→0.1	-0.53→0.1	-0.53→0.1	-0.53→0.1	-0.53→0.1	-0.53→0.1	-0.53→0.1	-0.53→0.1
KI(7698.9)	0.84 (51)	0.49 (16)	0.21 (18)	0.48 (29)	0.74 (47)	0.38 (24)	0.78 (43)	0.85 (41)	0.85 (44)	0.57 (39)
	0.72→0.9	-0.3→0.7	-0.53→0.53	-0.02→0.65	-0.07→0.51	-0.32→0.53	0.03→0.6	0.35→0.78	0.4→0.78	0.12→0.66
DIB(13180)	0.88 (82)	-0.31 (23)	0.73 (13)	0.05 (26)	0.84 (44)	-0.01 (39)	0.88 (40)	-0.01 (37)	0.19 (24)	-0.01 (42)
	0.85→0.94	-0.64→0.16	-0.17→0.84	-0.33→0.48	0.33→0.76	-0.38→0.28	0.38→0.79	-0.31→0.37	-0.38→0.47	-0.27→0.36
DIB(15650)	0.76 (43)	-0.31 (23)	0.73 (13)	0.05 (26)	0.82 (33)	-0.01 (39)	0.86 (29)	-0.01 (37)	0.19 (24)	-0.01 (42)
	0.59→0.87	-0.64→0.16	-0.17→0.84	-0.33→0.48	0.14→0.71	-0.38→0.28	0.22→0.78	-0.31→0.37	-0.38→0.47	-0.27→0.36
DIB(15670)	0.71 (46)	-0.31 (23)	0.73 (13)	0.05 (26)	0.80 (35)	-0.01 (39)	0.85 (32)	-0.01 (37)	0.19 (24)	-0.01 (42)
	0.59→0.86	-0.64→0.16	-0.17→0.84	-0.33→0.48	0.14→0.7	-0.38→0.28	0.19→0.75	-0.31→0.37	-0.38→0.47	-0.27→0.36

Table G.1. continued.

	DIB (6196.0)	DIB (6203.1)	DIB (6269.9)	DIB (6283.8)	DIB (6376.1)	DIB (6439.5)	DIB (6614.0)	DIB (6993.1)	DIB (13180)	DIB (15650)	DIB (1567)
E(B-V)	0.88 (54)	0.91 (57)	0.81 (51)	0.83 (51)	0.84 (40)	0.71 (30)	0.87 (44)	0.75 (41)	0.88 (82)	0.76 (43)	0.71 (46)
	0.79→0.93	0.87→0.95	0.68→0.89	0.7→0.9	0.66→0.9	0.46→0.86	0.74→0.92	0.6→0.87	0.85→0.94	0.59→0.87	0.59→0.86
Na(3302.4)	0.81 (30)	-0.05 (44)	-0.15 (27)	-0.10 (43)	-0.01 (42)	0.18 (37)	0.15 (27)	-0.22 (37)	-0.11 (31)	-0.11 (31)	-0.11 (31)
	0.21→0.76	-0.36→0.25	-0.56→0.2	-0.38→0.24	-0.3→0.33	-0.01→0.6	-0.47→0.32	-0.53→0.1	-0.49→0.24	-0.49→0.24	-0.49→0.24
FeI(3859.9)	0.39 (17)	-0.05 (44)	-0.15 (27)	-0.10 (43)	-0.01 (42)	0.18 (37)	0.15 (27)	-0.22 (37)	-0.31 (23)	-0.31 (23)	-0.31 (23)
	-0.25→0.71	-0.36→0.25	-0.56→0.2	-0.38→0.24	-0.3→0.33	-0.01→0.6	-0.47→0.32	-0.53→0.1	-0.64→0.16	-0.64→0.16	-0.64→0.16
CaII(3933.6)	0.67 (54)	-0.05 (44)	-0.15 (27)	-0.10 (43)	-0.01 (42)	0.18 (37)	0.15 (27)	-0.22 (37)	0.60 (48)	0.34 (32)	0.20 (34)
	-0.01→0.51	-0.36→0.25	-0.56→0.2	-0.38→0.24	-0.3→0.33	-0.01→0.6	-0.47→0.32	-0.53→0.1	-0.05→0.51	-0.39→0.35	-0.55→0.12
CaI(4226.7)	0.63 (44)	-0.05 (44)	-0.15 (27)	-0.10 (43)	-0.01 (42)	0.18 (37)	0.15 (27)	-0.22 (37)	0.42 (39)	0.27 (28)	0.42 (31)
	0.15→0.65	-0.36→0.25	-0.56→0.2	-0.38→0.24	-0.3→0.33	-0.01→0.6	-0.47→0.32	-0.53→0.1	-0.35→0.3	-0.52→0.26	-0.25→0.49
CH+(4232.5)	0.80 (47)	-0.05 (44)	-0.15 (27)	-0.10 (43)	-0.01 (42)	0.18 (37)	0.15 (27)	-0.22 (37)	-0.43 (45)	-0.43 (45)	-0.43 (45)
	0.04→0.58	-0.36→0.25	-0.56→0.2	-0.38→0.24	-0.3→0.33	-0.01→0.6	-0.47→0.32	-0.53→0.1	-0.72→-0.27	-0.72→-0.27	-0.72→-0.27
CH(4300.3)	0.76 (47)	-0.05 (44)	-0.15 (27)	-0.10 (43)	-0.01 (42)	0.18 (37)	0.15 (27)	-0.22 (37)	0.04 (41)	0.04 (41)	0.04 (41)
	-0.27→0.32	-0.36→0.25	-0.56→0.2	-0.38→0.24	-0.3→0.33	-0.01→0.6	-0.47→0.32	-0.53→0.1	-0.23→0.4	-0.23→0.4	-0.23→0.4
DIB(4726.8)	0.74 (46)	-0.05 (44)	-0.15 (27)	-0.10 (43)	-0.01 (42)	0.18 (37)	0.15 (27)	-0.22 (37)	0.01 (42)	0.01 (42)	0.01 (42)
	-0.11→0.48	-0.36→0.25	-0.56→0.2	-0.38→0.24	-0.3→0.33	-0.01→0.6	-0.47→0.32	-0.53→0.1	-0.17→0.45	-0.17→0.45	-0.17→0.45
DIB(4984.8)	0.34 (35)	-0.05 (44)	-0.15 (27)	-0.10 (43)	-0.01 (42)	0.18 (37)	0.15 (27)	-0.22 (37)	0.34 (29)	0.34 (29)	0.34 (29)
	-0.51→0.16	-0.36→0.25	-0.56→0.2	-0.38→0.24	-0.3→0.33	-0.01→0.6	-0.47→0.32	-0.53→0.1	-0.26→0.48	-0.26→0.48	-0.26→0.48
DIB(5074.5)	0.37 (21)	-0.05 (44)	-0.15 (27)	-0.10 (43)	-0.01 (42)	0.18 (37)	0.15 (27)	-0.22 (37)	0.73 (13)	0.73 (13)	0.73 (13)
	-0.26→0.65	-0.36→0.25	-0.56→0.2	-0.38→0.24	-0.3→0.33	-0.01→0.6	-0.47→0.32	-0.53→0.1	-0.17→0.84	-0.17→0.84	-0.17→0.84
DIB(5418.9)	0.35 (32)	-0.05 (44)	-0.15 (27)	-0.10 (43)	-0.01 (42)	0.18 (37)	0.15 (27)	-0.22 (37)	0.05 (26)	0.05 (26)	0.05 (26)
	-0.46→0.25	-0.36→0.25	-0.56→0.2	-0.38→0.24	-0.3→0.33	-0.01→0.6	-0.47→0.32	-0.53→0.1	-0.33→0.48	-0.33→0.48	-0.33→0.48
DIB(5705.1)	0.91 (46)	-0.05 (44)	-0.15 (27)	-0.10 (43)	-0.01 (42)	0.18 (37)	0.15 (27)	-0.22 (37)	0.84 (44)	0.82 (33)	0.80 (35)
	0.49→0.82	-0.36→0.25	-0.56→0.2	-0.38→0.24	-0.3→0.33	-0.01→0.6	-0.47→0.32	-0.53→0.1	0.33→0.76	0.14→0.71	0.14→0.7
DIB(5711.6)	0.53 (29)	-0.05 (44)	-0.15 (27)	-0.10 (43)	-0.01 (42)	0.18 (37)	0.15 (27)	-0.22 (37)	-0.01 (39)	-0.01 (39)	-0.01 (39)
	0.02→0.7	-0.36→0.25	-0.56→0.2	-0.38→0.24	-0.3→0.33	-0.01→0.6	-0.47→0.32	-0.53→0.1	-0.38→0.28	-0.38→0.28	-0.38→0.28
DIB(5780.5)	0.98 (45)	-0.05 (44)	-0.15 (27)	-0.10 (43)	-0.01 (42)	0.18 (37)	0.15 (27)	-0.22 (37)	0.88 (40)	0.86 (29)	0.85 (32)
	0.81→0.94	-0.36→0.25	-0.56→0.2	-0.38→0.24	-0.3→0.33	-0.01→0.6	-0.47→0.32	-0.53→0.1	0.38→0.79	0.22→0.78	0.19→0.75
DIB(5797.1)	0.95 (45)	-0.05 (44)	-0.15 (27)	-0.10 (43)	-0.01 (42)	0.18 (37)	0.15 (27)	-0.22 (37)	-0.01 (37)	-0.01 (37)	-0.01 (37)
	0.61→0.87	-0.36→0.25	-0.56→0.2	-0.38→0.24	-0.3→0.33	-0.01→0.6	-0.47→0.32	-0.53→0.1	-0.31→0.37	-0.31→0.37	-0.31→0.37
DIB(5849.8)	0.83 (45)	-0.05 (44)	-0.15 (27)	-0.10 (43)	-0.01 (42)	0.18 (37)	0.15 (27)	-0.22 (37)	0.19 (24)	0.19 (24)	0.19 (24)
	0.36→0.76	-0.36→0.25	-0.56→0.2	-0.38→0.24	-0.3→0.33	-0.01→0.6	-0.47→0.32	-0.53→0.1	-0.38→0.47	-0.38→0.47	-0.38→0.47
DIB(6089.9)	0.75 (41)	-0.05 (44)	-0.15 (27)	-0.10 (43)	-0.01 (42)	0.18 (37)	0.15 (27)	-0.22 (37)	-0.01 (42)	-0.01 (42)	-0.01 (42)
	0.22→0.71	-0.36→0.25	-0.56→0.2	-0.38→0.24	-0.3→0.33	-0.01→0.6	-0.47→0.32	-0.53→0.1	-0.27→0.36	-0.27→0.36	-0.27→0.36
DIB(6196.0)		-0.05 (44)	-0.15 (27)	-0.10 (43)	-0.01 (42)	0.18 (37)	0.15 (27)	-0.22 (37)	0.81 (47)	0.80 (34)	0.80 (36)
		-0.36→0.25	-0.56→0.2	-0.38→0.24	-0.3→0.33	-0.01→0.6	-0.47→0.32	-0.53→0.1	0.26→0.71	0.07→0.67	0.14→0.7
DIB(6203.1)	-0.05 (44)		-0.15 (27)	-0.10 (43)	-0.01 (42)	0.18 (37)	0.15 (27)	-0.22 (37)	-0.05 (44)	-0.05 (44)	-0.05 (44)
	-0.36→0.25		-0.56→0.2	-0.38→0.24	-0.3→0.33	-0.01→0.6	-0.47→0.32	-0.53→0.1	-0.36→0.25	-0.36→0.25	-0.36→0.25
DIB(6269.9)	-0.15 (27)	-0.15 (27)		-0.10 (43)	-0.01 (42)	0.18 (37)	0.15 (27)	-0.22 (37)	-0.15 (27)	-0.15 (27)	-0.15 (27)
	-0.56→0.2	-0.56→0.2		-0.38→0.24	-0.3→0.33	-0.01→0.6	-0.47→0.32	-0.53→0.1	-0.56→0.2	-0.56→0.2	-0.56→0.2

Table G.1. continued.

	DIB (6196.0)	DIB (6203.1)	DIB (6269.9)	DIB (6283.8)	DIB (6376.1)	DIB (6439.5)	DIB (6614.0)	DIB (6993.1)	DIB (13180)	DIB (15650)	DIB (1567)
DIB(6283.8)	-0.10 (43)	-0.10 (43)	-0.10 (43)		-0.01 (42)	0.18 (37)	0.15 (27)	-0.22 (37)	-0.10 (43)	-0.10 (43)	-0.10 (43)
	-0.38→0.24	-0.38→0.24	-0.38→0.24		-0.3→0.33	-0.01→0.6	-0.47→0.32	-0.53→0.1	-0.38→0.24	-0.38→0.24	-0.38→0.24
DIB(6376.1)	-0.01 (42)	-0.01 (42)	-0.01 (42)	-0.01 (42)		0.18 (37)	0.15 (27)	-0.22 (37)	-0.01 (42)	-0.01 (42)	-0.01 (42)
	-0.3→0.33	-0.3→0.33	-0.3→0.33	-0.3→0.33		-0.01→0.6	-0.47→0.32	-0.53→0.1	-0.3→0.33	-0.3→0.33	-0.3→0.33
DIB(6439.5)	0.18 (37)	0.18 (37)	0.18 (37)	0.18 (37)	0.18 (37)		0.15 (27)	-0.22 (37)	0.18 (37)	0.18 (37)	0.18 (37)
	-0.01→0.6	-0.01→0.6	-0.01→0.6	-0.01→0.6	-0.01→0.6		-0.47→0.32	-0.53→0.1	-0.01→0.6	-0.01→0.6	-0.01→0.6
DIB(6614.0)	0.15 (27)	0.15 (27)	0.15 (27)	0.15 (27)	0.15 (27)	0.15 (27)		-0.22 (37)	0.15 (27)	0.15 (27)	0.15 (27)
	-0.47→0.32	-0.47→0.32	-0.47→0.32	-0.47→0.32	-0.47→0.32	-0.47→0.32		-0.53→0.1	-0.47→0.32	-0.47→0.32	-0.47→0.32
DIB(6993.1)	-0.22 (37)	-0.22 (37)	-0.22 (37)	-0.22 (37)	-0.22 (37)	-0.22 (37)	-0.22 (37)		-0.22 (37)	-0.22 (37)	-0.22 (37)
	-0.53→0.1	-0.53→0.1	-0.53→0.1	-0.53→0.1	-0.53→0.1	-0.53→0.1	-0.53→0.1		-0.53→0.1	-0.53→0.1	-0.53→0.1
KI(7698.9)	0.81 (49)	0.78 (52)	0.75 (52)	0.75 (53)	0.71 (40)	0.64 (29)	0.81 (41)	0.65 (44)	0.67 (47)	0.50 (33)	0.52 (35)
	0.25→0.7	-0.06→0.49	0.05→0.57	-0.05→0.49	0.24→0.72	-0.→0.66	0.4→0.8	0.03→0.59	-0.32→0.28	-0.42→0.3	-0.26→0.44
DIB(13180)	0.81 (47)	-0.05 (44)	-0.15 (27)	-0.10 (43)	-0.01 (42)	0.18 (37)	0.15 (27)	-0.22 (37)		-0.08 (25)	-0.15 (28)
	0.26→0.71	-0.36→0.25	-0.56→0.2	-0.38→0.24	-0.3→0.33	-0.01→0.6	-0.47→0.32	-0.53→0.1		-0.39→0.44	-0.26→0.51
DIB(15650)	0.80 (34)	-0.05 (44)	-0.15 (27)	-0.10 (43)	-0.01 (42)	0.18 (37)	0.15 (27)	-0.22 (37)	-0.08 (25)		-0.15 (28)
	0.07→0.67	-0.36→0.25	-0.56→0.2	-0.38→0.24	-0.3→0.33	-0.01→0.6	-0.47→0.32	-0.53→0.1	-0.39→0.44		-0.26→0.51
DIB(15670)	0.80 (36)	-0.05 (44)	-0.15 (27)	-0.10 (43)	-0.01 (42)	0.18 (37)	0.15 (27)	-0.22 (37)	-0.15 (28)	-0.15 (28)	
	0.14→0.7	-0.36→0.25	-0.56→0.2	-0.38→0.24	-0.3→0.33	-0.01→0.6	-0.47→0.32	-0.53→0.1	-0.26→0.51	-0.26→0.51	

Appendix H: Correlation coefficients for the single component dominated sample

Table H.1. Correlation coefficients for single component dominated sightlines. The number of sightlines used per correlation is shown in brackets. Both the standard Pearson correlation coefficient (top row per parameter) and 95 percent confidence range (second row) for the partial correlation coefficients are presented.

	E(B-V)	FeI (3859.9)	DIB (5074.5)	DIB (5418.9)	DIB (5705.1)	DIB (5711.6)	DIB) (5780.5)	DIB (5797.1)	DIB (5849.8)	DIB (6089.9)
E(B-V)			0.84 (6)	0.78 (7)	0.92 (10)	0.59 (7)	0.95 (12)	0.92 (12)	0.84 (10)	0.75 (9)
			-0.8→0.99	0.36→1.	-0.01→0.94	0.02→0.99	0.44→0.96	0.89→0.99	0.22→0.96	-0.38→0.92
Na(3302.4)	0.99 (7)	-0.52 (5)				0.35 (9)		0.39 (11)	0.44 (5)	0.41 (12)
	0.36→1.	-1.→1.				-0.77→0.74		-0.78→0.51	-1.→1.	-0.08→0.89
FeI(3859.9)						0.35 (9)		0.39 (11)	0.44 (5)	0.41 (12)
						-0.77→0.74		-0.78→0.51	-1.→1.	-0.08→0.89
CaII(3933.6)	0.83 (16)		0.74 (6)	0.46 (7)	0.79 (11)	0.35 (9)	0.73 (13)	0.39 (11)	0.44 (5)	0.41 (12)
	0.18→0.88		-0.93→0.98	-0.9→0.87	-0.49→0.79	-0.77→0.74	-0.6→0.66	-0.78→0.51	-1.→1.	-0.08→0.89
CaI(4226.7)	0.80 (13)		0.75 (6)	0.34 (7)	0.82 (9)	0.35 (9)	0.90 (11)	0.39 (11)	0.44 (5)	0.41 (12)
	0.17→0.92		-0.95→0.97	-0.73→0.95	0.05→0.96	-0.77→0.74	0.09→0.93	-0.78→0.51	-1.→1.	-0.08→0.89
CH+(4232.5)	0.88 (12)	0.10 (13)	0.50 (5)	0.69 (7)	0.73 (10)	0.35 (9)	0.85 (10)	0.39 (11)	0.44 (5)	0.41 (12)
	0.85→0.99	-0.65→0.54	-1.→1.	-0.96→0.65	-0.88→0.36	-0.77→0.74	-0.86→0.59	-0.78→0.51	-1.→1.	-0.08→0.89
CH(4300.3)	0.94 (12)	0.63 (10)	0.77 (5)	0.80 (7)	0.79 (10)	0.35 (9)	0.83 (12)	0.39 (11)	0.44 (5)	0.41 (12)
	0.81→0.99	0.1→0.95	-1.→1.	-0.96→0.65	-0.84→0.48	-0.77→0.74	-0.86→0.3	-0.78→0.51	-1.→1.	-0.08→0.89
DIB(4726.8)	0.80 (12)	0.27 (11)	0.52 (6)	0.77 (7)	0.63 (10)	0.35 (9)	0.56 (10)	0.39 (11)	0.44 (5)	0.41 (12)
	0.46→0.96	-0.46→0.8	-0.99→0.87	-0.96→0.68	-0.81→0.55	-0.77→0.74	-0.88→0.51	-0.78→0.51	-1.→1.	-0.08→0.89
DIB(4984.8)	0.87 (7)	0.23 (8)		0.85 (7)	0.79 (6)	0.35 (9)	0.68 (6)	0.39 (11)	0.44 (5)	0.41 (12)
	-0.6→0.97	-0.88→0.7		-0.64→0.97	-0.99→0.9	-0.77→0.74	-0.87→0.99	-0.78→0.51	-1.→1.	-0.08→0.89
DIB(5074.5)	0.84 (6)					0.35 (9)		0.39 (11)	0.44 (5)	0.41 (12)
	-0.8→0.99					-0.77→0.74		-0.78→0.51	-1.→1.	-0.08→0.89
DIB(5418.9)	0.78 (7)				0.70 (6)	0.35 (9)	0.89 (6)	0.39 (11)	0.44 (5)	0.41 (12)
	0.36→1.				-0.7→1.	-0.77→0.74	-1.→-1.	-0.78→0.51	-1.→1.	-0.08→0.89
DIB(5705.1)	0.92 (10)			0.70 (6)		0.35 (9)	0.94 (9)	0.39 (11)	0.44 (5)	0.41 (12)
	-0.01→0.94			-0.7→1.		-0.77→0.74	0.5→0.99	-0.78→0.51	-1.→1.	-0.08→0.89
DIB(5711.6)	0.59 (7)	0.35 (9)	0.35 (9)	0.35 (9)	0.35 (9)		0.48 (5)	0.39 (11)	0.44 (5)	0.41 (12)
	0.02→0.99	-0.77→0.74	-0.77→0.74	-0.77→0.74	-0.77→0.74		-1.→1.	-0.78→0.51	-1.→1.	-0.08→0.89
DIB(5780.5)	0.95 (12)			0.89 (6)	0.94 (9)	0.48 (5)		0.39 (11)	0.44 (5)	0.41 (12)
	0.44→0.96			-1.→-1.	0.5→0.99	-1.→1.		-0.78→0.51	-1.→1.	-0.08→0.89
DIB(5797.1)	0.92 (12)	0.39 (11)	0.39 (11)	0.39 (11)	0.39 (11)	0.39 (11)	0.39 (11)		0.44 (5)	0.41 (12)
	0.89→0.99	-0.78→0.51	-0.78→0.51	-0.78→0.51	-0.78→0.51	-0.78→0.51	-0.78→0.51		-1.→1.	-0.08→0.89
DIB(5849.8)	0.84 (10)	0.44 (5)	0.44 (5)	0.44 (5)	0.44 (5)	0.44 (5)	0.44 (5)	0.44 (5)		0.41 (12)
	0.22→0.96	-1.→1.	-1.→1.	-1.→1.	-1.→1.	-1.→1.	-1.→1.	-1.→1.		-0.08→0.89
DIB(6089.9)	0.75 (9)	0.41 (12)	0.41 (12)	0.41 (12)	0.41 (12)	0.41 (12)	0.41 (12)	0.41 (12)	0.41 (12)	
	-0.38→0.92	-0.08→0.89	-0.08→0.89	-0.08→0.89	-0.08→0.89	-0.08→0.89	-0.08→0.89	-0.08→0.89	-0.08→0.89	
DIB(6196.0)	0.93 (16)		0.87 (6)	0.50 (7)	0.91 (10)	0.72 (7)	0.98 (12)	0.97 (12)	0.91 (10)	0.92 (9)
	0.66→0.96		-0.97→0.95	-0.73→0.95	-0.15→0.92	-1.→-1.	0.45→0.96	0.01→0.9	-0.23→0.91	0.66→0.99
DIB(6203.1)	0.96 (15)	0.28 (13)	0.28 (13)	0.28 (13)	0.28 (13)	0.28 (13)	0.28 (13)	0.28 (13)	0.28 (13)	0.28 (13)
	0.9→0.99	-0.61→0.58	-0.61→0.58	-0.61→0.58	-0.61→0.58	-0.61→0.58	-0.61→0.58	-0.61→0.58	-0.61→0.58	-0.61→0.58
DIB(6269.9)	0.90 (13)	0.30 (7)	0.30 (7)	0.30 (7)	0.30 (7)	0.30 (7)	0.30 (7)	0.30 (7)	0.30 (7)	0.30 (7)
	0.56→0.97	-0.83→0.92	-0.83→0.92	-0.83→0.92	-0.83→0.92	-0.83→0.92	-0.83→0.92	-0.83→0.92	-0.83→0.92	-0.83→0.92

Table H.1. continued.

	E(B-V)	FeI (3859.9)	DIB (5074.5)	DIB (5418.9)	DIB (5705.1)	DIB (5711.6)	DIB) (5780.5)	DIB (5797.1)	DIB (5849.8)	DIB (6089.9)
DIB(6283.8)	0.92 (12)	0.65 (11)	0.65 (11)	0.65 (11)	0.65 (11)	0.65 (11)	0.65 (11)	0.65 (11)	0.65 (11)	0.65 (11)
	0.39→0.96	-0.31→0.86	-0.31→0.86	-0.31→0.86	-0.31→0.86	-0.31→0.86	-0.31→0.86	-0.31→0.86	-0.31→0.86	-0.31→0.86
DIB(6376.1)	0.88 (8)	0.52 (10)	0.52 (10)	0.52 (10)	0.52 (10)	0.52 (10)	0.52 (10)	0.52 (10)	0.52 (10)	0.52 (10)
	0.15→0.98	-0.36→0.88	-0.36→0.88	-0.36→0.88	-0.36→0.88	-0.36→0.88	-0.36→0.88	-0.36→0.88	-0.36→0.88	-0.36→0.88
DIB(6439.5)	0.81 (5)	0.37 (10)	0.37 (10)	0.37 (10)	0.37 (10)	0.37 (10)	0.37 (10)	0.37 (10)	0.37 (10)	0.37 (10)
	-1.→1.	-0.56→0.81	-0.56→0.81	-0.56→0.81	-0.56→0.81	-0.56→0.81	-0.56→0.81	-0.56→0.81	-0.56→0.81	-0.56→0.81
DIB(6614.0)	0.92 (12)		0.92 (5)	0.55 (7)	0.90 (8)	0.66 (6)	0.97 (9)	0.96 (9)	0.96 (9)	0.88 (7)
	0.57→0.97		-1.→1.	-0.73→0.95	-0.12→0.97	-1.→-1.	0.54→0.99	-0.39→0.91	0.15→0.97	0.37→1.
DIB(6993.1)	0.96 (8)	0.21 (10)	0.21 (10)	0.21 (10)	0.21 (10)	0.21 (10)	0.21 (10)	0.21 (10)	0.21 (10)	0.21 (10)
	0.3→0.99	-0.65→0.75	-0.65→0.75	-0.65→0.75	-0.65→0.75	-0.65→0.75	-0.65→0.75	-0.65→0.75	-0.65→0.75	-0.65→0.75
KI(7698.9)	0.90 (12)			0.79 (6)	0.89 (11)	0.58 (5)	0.85 (10)	0.95 (10)	0.98 (9)	0.66 (10)
	0.75→0.99			-1.→-1.	-0.3→0.86	-1.→1.	-0.53→0.82	-0.29→0.9	-0.03→0.96	-0.66→0.74
DIB(13180)	0.80 (15)	-0.52 (5)		0.69 (5)	0.84 (9)	0.35 (9)	0.90 (8)	0.39 (11)	0.44 (5)	0.41 (12)
	-0.14→0.87	-1.→1.		-1.→1.	-0.21→0.94	-0.77→0.74	-0.08→0.97	-0.78→0.51	-1.→1.	-0.08→0.89
DIB(15650)	0.96 (5)	-0.52 (5)			0.84 (5)	0.35 (9)		0.39 (11)	0.44 (5)	0.41 (12)
	-1.→1.	-1.→1.			-1.→1.	-0.77→0.74		-0.78→0.51	-1.→1.	-0.08→0.89
DIB(15670)	0.88 (8)	-0.52 (5)			0.87 (6)	0.35 (9)	0.86 (6)	0.39 (11)	0.44 (5)	0.41 (12)
	0.11→0.98	-1.→1.			-0.7→1.	-0.77→0.74	-0.99→0.86	-0.78→0.51	-1.→1.	-0.08→0.89

Table H.1. continued.

	DIB (6196.0)	DIB (6203.1)	DIB (6269.9)	DIB (6283.8)	DIB (6376.1)	DIB (6439.5)	DIB (6614.0)	DIB (6993.1)	DIB (13180)	DIB (15650)	DIB (1567)
E(B-V)	0.93 (16)	0.96 (15)	0.90 (13)	0.92 (12)	0.88 (8)	0.81 (5)	0.92 (12)	0.96 (8)	0.80 (15)	0.96 (5)	0.88 (8)
	0.66→0.96	0.9→0.99	0.56→0.97	0.39→0.96	0.15→0.98	-1.→1.	0.57→0.97	0.3→0.99	-0.14→0.87	-1.→1.	0.11→0.98
Na(3302.4)	0.89 (7)	0.28 (13)	0.30 (7)	0.65 (11)	0.52 (10)	0.37 (10)	0.90 (6)	0.21 (10)	0.12 (7)	0.12 (7)	0.12 (7)
	-0.94→0.79	-0.61→0.58	-0.83→0.92	-0.31→0.86	-0.36→0.88	-0.56→0.81	-0.93→0.98	-0.65→0.75	-0.95→0.73	-0.95→0.73	-0.95→0.73
FeI(3859.9)		0.28 (13)	0.30 (7)	0.65 (11)	0.52 (10)	0.37 (10)		0.21 (10)	-0.52 (5)	-0.52 (5)	-0.52 (5)
		-0.61→0.58	-0.83→0.92	-0.31→0.86	-0.36→0.88	-0.56→0.81		-0.65→0.75	-1.→1.	-1.→1.	-1.→1.
CaII(3933.6)	0.83 (16)	0.28 (13)	0.30 (7)	0.65 (11)	0.52 (10)	0.37 (10)	0.81 (12)	0.21 (10)	0.83 (10)	0.74 (5)	0.55 (7)
	-0.41→0.63	-0.61→0.58	-0.83→0.92	-0.31→0.86	-0.36→0.88	-0.56→0.81	-0.5→0.73	-0.65→0.75	-0.58→0.8	-1.→1.	-0.9→0.86
CaI(4226.7)	0.91 (13)	0.28 (13)	0.30 (7)	0.65 (11)	0.52 (10)	0.37 (10)	0.92 (10)	0.21 (10)	0.52 (9)	0.59 (5)	0.69 (7)
	0.25→0.93	-0.61→0.58	-0.83→0.92	-0.31→0.86	-0.36→0.88	-0.56→0.81	-0.16→0.92	-0.65→0.75	-0.74→0.76	-1.→1.	-0.93→0.8
CH+(4232.5)	0.77 (12)	0.28 (13)	0.30 (7)	0.65 (11)	0.52 (10)	0.37 (10)	0.74 (11)	0.21 (10)	0.10 (13)	0.10 (13)	0.10 (13)
	-0.6→0.65	-0.61→0.58	-0.83→0.92	-0.31→0.86	-0.36→0.88	-0.56→0.81	-0.68→0.64	-0.65→0.75	-0.65→0.54	-0.65→0.54	-0.65→0.54
CH(4300.3)	0.80 (12)	0.28 (13)	0.30 (7)	0.65 (11)	0.52 (10)	0.37 (10)	0.81 (10)	0.21 (10)	0.63 (10)	0.63 (10)	0.63 (10)
	-0.83→0.28	-0.61→0.58	-0.83→0.92	-0.31→0.86	-0.36→0.88	-0.56→0.81	-0.86→0.44	-0.65→0.75	0.1→0.95	0.1→0.95	0.1→0.95
DIB(4726.8)	0.66 (12)	0.28 (13)	0.30 (7)	0.65 (11)	0.52 (10)	0.37 (10)	0.61 (10)	0.21 (10)	0.27 (11)	0.27 (11)	0.27 (11)
	-0.82→0.32	-0.61→0.58	-0.83→0.92	-0.31→0.86	-0.36→0.88	-0.56→0.81	-0.83→0.51	-0.65→0.75	-0.46→0.8	-0.46→0.8	-0.46→0.8
DIB(4984.8)	0.53 (7)	0.28 (13)	0.30 (7)	0.65 (11)	0.52 (10)	0.37 (10)	0.56 (7)	0.21 (10)	0.23 (8)	0.23 (8)	0.23 (8)
	-0.94→0.79	-0.61→0.58	-0.83→0.92	-0.31→0.86	-0.36→0.88	-0.56→0.81	-0.94→0.79	-0.65→0.75	-0.88→0.7	-0.88→0.7	-0.88→0.7
DIB(5074.5)	0.87 (6)	0.28 (13)	0.30 (7)	0.65 (11)	0.52 (10)	0.37 (10)	0.92 (5)	0.21 (10)			
	-0.97→0.95	-0.61→0.58	-0.83→0.92	-0.31→0.86	-0.36→0.88	-0.56→0.81	-1.→1.	-0.65→0.75			
DIB(5418.9)	0.50 (7)	0.28 (13)	0.30 (7)	0.65 (11)	0.52 (10)	0.37 (10)	0.55 (7)	0.21 (10)	0.69 (5)		
	-0.73→0.95	-0.61→0.58	-0.83→0.92	-0.31→0.86	-0.36→0.88	-0.56→0.81	-0.73→0.95	-0.65→0.75	-1.→1.		
DIB(5705.1)	0.91 (10)	0.28 (13)	0.30 (7)	0.65 (11)	0.52 (10)	0.37 (10)	0.90 (8)	0.21 (10)	0.84 (9)	0.84 (5)	0.87 (6)
	-0.15→0.92	-0.61→0.58	-0.83→0.92	-0.31→0.86	-0.36→0.88	-0.56→0.81	-0.12→0.97	-0.65→0.75	-0.21→0.94	-1.→1.	-0.7→1.
DIB(5711.6)	0.72 (7)	0.28 (13)	0.30 (7)	0.65 (11)	0.52 (10)	0.37 (10)	0.66 (6)	0.21 (10)	0.35 (9)	0.35 (9)	0.35 (9)
	-1.→-1.	-0.61→0.58	-0.83→0.92	-0.31→0.86	-0.36→0.88	-0.56→0.81	-1.→-1.	-0.65→0.75	-0.77→0.74	-0.77→0.74	-0.77→0.74
DIB(5780.5)	0.98 (12)	0.28 (13)	0.30 (7)	0.65 (11)	0.52 (10)	0.37 (10)	0.97 (9)	0.21 (10)	0.90 (8)		0.86 (6)
	0.45→0.96	-0.61→0.58	-0.83→0.92	-0.31→0.86	-0.36→0.88	-0.56→0.81	0.54→0.99	-0.65→0.75	-0.08→0.97		-0.99→0.86
DIB(5797.1)	0.97 (12)	0.28 (13)	0.30 (7)	0.65 (11)	0.52 (10)	0.37 (10)	0.96 (9)	0.21 (10)	0.39 (11)	0.39 (11)	0.39 (11)
	0.01→0.9	-0.61→0.58	-0.83→0.92	-0.31→0.86	-0.36→0.88	-0.56→0.81	-0.39→0.91	-0.65→0.75	-0.78→0.51	-0.78→0.51	-0.78→0.51
DIB(5849.8)	0.91 (10)	0.28 (13)	0.30 (7)	0.65 (11)	0.52 (10)	0.37 (10)	0.96 (9)	0.21 (10)	0.44 (5)	0.44 (5)	0.44 (5)
	-0.23→0.91	-0.61→0.58	-0.83→0.92	-0.31→0.86	-0.36→0.88	-0.56→0.81	0.15→0.97	-0.65→0.75	-1.→1.	-1.→1.	-1.→1.
DIB(6089.9)	0.92 (9)	0.28 (13)	0.30 (7)	0.65 (11)	0.52 (10)	0.37 (10)	0.88 (7)	0.21 (10)	0.41 (12)	0.41 (12)	0.41 (12)
	0.66→0.99	-0.61→0.58	-0.83→0.92	-0.31→0.86	-0.36→0.88	-0.56→0.81	0.37→1.	-0.65→0.75	-0.08→0.89	-0.08→0.89	-0.08→0.89
DIB(6196.0)		0.28 (13)	0.30 (7)	0.65 (11)	0.52 (10)	0.37 (10)	0.99 (12)	0.21 (10)	0.73 (10)	0.83 (5)	0.82 (7)
		-0.61→0.58	-0.83→0.92	-0.31→0.86	-0.36→0.88	-0.56→0.81	0.44→0.96	-0.65→0.75	-0.53→0.82	-1.→1.	-0.93→0.79
DIB(6203.1)	0.28 (13)		0.30 (7)	0.65 (11)	0.52 (10)	0.37 (10)	0.94 (11)	0.21 (10)	0.28 (13)	0.28 (13)	0.28 (13)
	-0.61→0.58		-0.83→0.92	-0.31→0.86	-0.36→0.88	-0.56→0.81	0.56→0.98	-0.65→0.75	-0.61→0.58	-0.61→0.58	-0.61→0.58
DIB(6269.9)	0.30 (7)	0.30 (7)		0.65 (11)	0.52 (10)	0.37 (10)	0.94 (11)	0.21 (10)	0.30 (7)	0.30 (7)	0.30 (7)
	-0.83→0.92	-0.83→0.92		-0.31→0.86	-0.36→0.88	-0.56→0.81	0.38→0.96	-0.65→0.75	-0.83→0.92	-0.83→0.92	-0.83→0.92

Table H.1. continued.

	DIB (6196.0)	DIB (6203.1)	DIB (6269.9)	DIB (6283.8)	DIB (6376.1)	DIB (6439.5)	DIB (6614.0)	DIB (6993.1)	DIB (13180)	DIB (15650)	DIB (1567)
DIB(6283.8)	0.65 (11)	0.65 (11)	0.65 (11)		0.52 (10)	0.37 (10)	0.92 (10)	0.21 (10)	0.65 (11)	0.65 (11)	0.65 (11)
	-0.31→0.86	-0.31→0.86	-0.31→0.86		-0.36→0.88	-0.56→0.81	0.69→0.99	-0.65→0.75	-0.31→0.86	-0.31→0.86	-0.31→0.86
DIB(6376.1)	0.52 (10)	0.52 (10)	0.52 (10)	0.52 (10)		0.37 (10)	0.98 (7)	0.21 (10)	0.52 (10)	0.52 (10)	0.52 (10)
	-0.36→0.88	-0.36→0.88	-0.36→0.88	-0.36→0.88		-0.56→0.81	-0.27→0.99	-0.65→0.75	-0.36→0.88	-0.36→0.88	-0.36→0.88
DIB(6439.5)	0.37 (10)	0.37 (10)	0.37 (10)	0.37 (10)	0.37 (10)			0.21 (10)	0.37 (10)	0.37 (10)	0.37 (10)
	-0.56→0.81	-0.56→0.81	-0.56→0.81	-0.56→0.81	-0.56→0.81			-0.65→0.75	-0.56→0.81	-0.56→0.81	-0.56→0.81
DIB(6614.0)	0.99 (12)	0.94 (11)	0.94 (11)	0.92 (10)	0.98 (7)			0.21 (10)	0.71 (8)	0.80 (5)	0.82 (6)
	0.44→0.96	0.56→0.98	0.38→0.96	0.69→0.99	-0.27→0.99			-0.65→0.75	-0.69→0.89	-1.→1.	-0.7→1.
DIB(6993.1)	0.21 (10)	0.21 (10)	0.21 (10)	0.21 (10)	0.21 (10)	0.21 (10)	0.21 (10)		0.21 (10)	0.21 (10)	0.21 (10)
	-0.65→0.75	-0.65→0.75	-0.65→0.75	-0.65→0.75	-0.65→0.75	-0.65→0.75	-0.65→0.75		-0.65→0.75	-0.65→0.75	-0.65→0.75
KI(7698.9)	0.91 (12)	0.87 (13)	0.88 (13)	0.83 (13)	0.91 (9)	0.58 (6)	0.94 (10)	0.96 (9)	0.65 (10)	0.66 (5)	0.61 (7)
	-0.6→0.66	-0.62→0.58	-0.7→0.48	-0.63→0.57	-0.62→0.85	-0.85→0.99	-0.59→0.79	-0.51→0.88	-0.78→0.61	-1.→1.	-0.94→0.77
DIB(13180)	0.73 (10)	0.28 (13)	0.30 (7)	0.65 (11)	0.52 (10)	0.37 (10)	0.71 (8)	0.21 (10)		0.29 (5)	0.26 (5)
	-0.53→0.82	-0.61→0.58	-0.83→0.92	-0.31→0.86	-0.36→0.88	-0.56→0.81	-0.69→0.89	-0.65→0.75		-1.→1.	-1.→1.
DIB(15650)	0.83 (5)	0.28 (13)	0.30 (7)	0.65 (11)	0.52 (10)	0.37 (10)	0.80 (5)	0.21 (10)	0.29 (5)		0.26 (5)
	-1.→1.	-0.61→0.58	-0.83→0.92	-0.31→0.86	-0.36→0.88	-0.56→0.81	-1.→1.	-0.65→0.75	-1.→1.		-1.→1.
DIB(15670)	0.82 (7)	0.28 (13)	0.30 (7)	0.65 (11)	0.52 (10)	0.37 (10)	0.82 (6)	0.21 (10)	0.26 (5)	0.26 (5)	
	-0.93→0.79	-0.61→0.58	-0.83→0.92	-0.31→0.86	-0.36→0.88	-0.56→0.81	-0.7→1.	-0.65→0.75	-1.→1.	-1.→1.	